Rol de la entropía en la enantioselectividad de la acilación del propranolol catalizada por lipasa B de *Candida antarctica*

Daniel Iván Barrera Valderrama

Tesis doctoral en Química

Asesores
Martha Cecilia Daza Espinosa
Doctora en Ciencias - Química

Markus Hans Oliver Doerr
Dr. rer. nat.
Grupo de Bioquímica Teórica

Universidad Industrial de Santander
Facultad de Ciencias
Escuela de Química
Bucaramanga
2020

Dedication

To my parents Jaime Arturo and Alicia Victoria and my brothers Fernando, Jaime, and Samuel one million of thanks for the truth in this long voyageur…

Acknowledgments

To my advisers Dr. Markus Doerr and Dra. Martha C. Daza for all scientific support.

To all mates at Grupo de Bioquímica Teórica at Universidad Industrial de Santander.

To my classmates, Ximena, Monica, Carolina, María, and Cirito for all great moments at seminars.

To Dr. Stefan Erhardt, Farah Al-Muzian, and Mr. and Mrs. Strachan for all kindly shared time in Edinburgh and Perth, Scotland.

To Dr. Guillermo Restrepo, Wilmer Leal, Ritoparnu, and Prof. Dr. Peter Stadler for all scientific meetings and funny time spent in Leipzig, Germany.

The financial support from COLCIENCIAS through the Fellowship of the Ph.D. Program 2015 is gratefully recognized. I also acknowledge the financial support from COLCIENCIAS (projects 8110256933409, 110271250586) and VIE-UIS (projects 5702 and 8855) given during my doctoral studies.

Finally, I thank the referees: Dra. Constanza Cárdenas Carvajal, Dr. Eduardo Chamorro Jiménez, Dr. Jhon Pérez Torres, Dr. Enrique Mejía Ospino and Dr. Herminsul Cano Calle for dedicating time on revising my dissertation and for their kind suggestions.

Table of Contents

Pag.

List of Tables

List of figures

List of appendixes

List of abbreviations

AceCalB	acetylated CalB
AM1	austin Method 1
CalB	*Candida antarctica* lipase B
DFT	density functional theory
E	enantiomeric ratio or enantioselectivity
ee	enantiomeric excess
EPC	enzyme-Product complex
k_{cat}	catalytic constant / turnover number
K_M	Michaelis-Menten constant
MCC	michaelis complex
MD	molecular dynamics
NAC	near attack conformer
O-AP	*O*-acetylpropranolol
OM2	orthogonalization method 2
OM3	orthogonalization method 3
PES	potential energy surface
PM3	parametrized Model number 3
QM/MM	Quantum Mechanics/Molecular Mechanics
SCC-DFTB	Self-consistent charge-density functional tight binding
SEA	acylated catalytic serine
TI	tetrahedral intermediate
TI-2	tetrahedral intermediate-2
TS	transition state
TZVP	triple-ζ basis set for valence electrons with (d,p) polarization functions
Δ_R or $\Delta_S G^{\ddagger}$	Gibbs free energy of activation for each enantiomer
$\Delta_{(R\text{-}S)}\Delta G^{\ddagger}$	difference in Gibbs free energy of activation for the enantiomers
$\Delta_{(R\text{-}S)}\Delta H^{\ddagger}$	difference in activation enthalpy for the enantiomers
$\Delta_{(R\text{-}S)}\Delta S^{\ddagger}$	difference in activation entropy for the enantiomers

Resumen

TÍTULO: Rol de la entropía en la enantioselectividad de la acilación de (*R*,*S*)-propranolol catalizada por lipasa B de *Candida antarctica*

AUTOR: DANIEL IVÁN BARRERA VALDERRAMA

PALABRAS CLAVE: Entropía, Efectos de la temperatura finita, enantioselectividad, *Umbrella sampling*

DESCRIPCIÓN: La lipasa B de *Candida antarctica* cataliza la *O*-acilación del (*R,S*) -propranolol usando tolueno como solvente. Esta lipasa muestra enantioselectividad moderada (*E* = 61-63) y quimioselectividad exclusiva que favorece la formación más rápida de *R*-*O*-acetil-propranolol. La reacción implica dos pasos. El primer paso conduce a la formación de una acil-enzima reactiva (acilación). El segundo paso (desacilación) conduce a la formación de (*R*,*S*) -acil-propranolol. La quimio y enantioselectividad se origina en el paso de desacilación. La comprensión de la enantioselectividad experimental se ha centrado en el paso de desacilación mediante protocolos combinados de acoplamiento y dinámica molecular. Los resultados mostraron que se favorece la transformación de (*R*)-propranolol.
En esta tesis se estudió el papel de la entropía en la enantioselectividad de la acilación del propranolol catalizada por la lipasa B de *Candida antarctica* mediante un enfoque computacional. El espacio de configuración se analizó a lo largo de la reacción de desacilación (MCC → TI → EPC) utilizando métodos QM / MM y QM / MM-MD, incluyendo el enfoque de Conformación de Ataque Cercano (NAC). Los NAC es un subgrupo de los MCC que se asemejan al estado de transición. Los resultados muestran que el enfoque de NAC es una herramienta para comprender el espacio de configuración durante la conversión de MCC a TI; sin embargo, no permiten concluir sobre la enantioselectividad de la reacción en este caso.
Los valores de la barrera de energía libre oscilan entre 9,7 y 13,4 kcal / mol para el (*R*) -propranolol y entre 9,3 y 14,9 kcal / mol para (*S*) -propranolol y confirma que el intermediario tetraédrico no es una buena representación de los estados de transición. La superposición del potencial de fuerza media (PMF) y la superficie de energía potencial (PES) dio información sobre el efecto de temperatura finita (f.t.e = PMF - PES). El papel de la entropía en la *O*-acilación del propranolol catalizado por CalB es aumentar la energía de la TI-2. Finalmente, los resultados computacionales obtenidos aquí contribuyen a una mejor comprensión del papel de la entropía en la enantioselectividad de la acilación de propranolol catalizada por la lipasa B de *Candida antarctica*.

---

* Tesis Doctoral

**Facultad de Ciencias. Escuela de Química. Doctorado en Química.

Directora Dra. Martha Cecilia Daza Espinosa, Director Dr. Markus Hans Olivier Doerr

Abstract

TITLE: Role of entropy in the enantioselectivity of acylation of propranolol catalyzed by lipase B of *Candida antarctica*

AUTHOR: DANIEL IVÁN BARRERA VALDERRAMA

KEYWORDS: Entropy, Finite-temperature effects, Enantioselectivity, Umbrella sampling

DESCRIPTION: *Candida antarctica* Lipase B catalyzes the O-acylation of the (*R*,*S*)-propranolol using toluene as solvent. This lipase displays moderate enantioselectivity (*E* = 61-63) and exclusive chemoselectivity favoring the faster formation of *R*-*O*-acetyl-propranolol. The reaction involves two steps. The first step leads to the formation of a reactive acyl-enzyme (acylation). The second step (deacylation) leads to the formation of (*R,S*)-acyl-propranolol. The chemo- and enantioselectivity originates from the deacylation step. The rationalization of the experimental enantioselectivity has been focused on the deacylation step by combined docking and molecular dynamics protocols. Additionally, the energetic barriers for the *O*-acetylation of (*R*)- and (*S*)- propranolol were calculated using the Quantum Mechanics/Molecular Mechanics (QM/MM) approach. The results showed that the transformation of R-propranolol is favored.

In this dissertation, the role of the entropy in the enantioselectivity of the acylation of propranolol catalyzed by lipase B of *Candida antarctica* was studied through a computational approach. The configurational space was analyzed throughout all deacylation step of the reaction (MCC→TI→EPC) using several QM/MM and QM/MM-MD methods, including the Near Attack Conformation (NAC) approach. NACs are a subgroup of the Michaelis complexes MCCs which closely resembles the transition state. Besides, the effect of the modification of the initial velocities of QM / MM-MD in enantioselective reactions is reported. The results show that the NAC approach is a tool for understanding the configurational space during the conversion from MCC to TI; nevertheless, no conclusion respect to the enantioselectivity can be drawn here.

Free energy calculations show that the values of the free energy barrier ranged from 9,7 to 13,4 kcal/mol for (*R*)-propranolol and between 9,3 to 14,9 kcal/mol for (*S*)-propranolol. The free energy barriers confirm that the TI is not a good representation of the transition states, in contrast to what is commonly suggested for lipase-catalyzed reactions. The entropy was calculated as the difference between free energy profile (PMF) and minimal energy pathway calculated by QM/MM relaxed scans (PES). The superposition of PMF and PES gave us information about the finite-temperature effect (f.t.e =PMF – PES). The role of the entropy in the *O*-acylation of the propranolol catalyzed by CalB is to increase the energy of the TI-2. In general, the effect of the entropy can reach values of ~8kcal/mol. Finally, the computational results obtained here contribute to a better understanding of the role of entropy in the enantioselectivity of acylation of propranolol catalyzed by lipase B from *Candida antarctica*.

---

* Doctoral Dissertation

**Facultad de Ciencias. Escuela de Química. Doctorado en Química

Advisor: Dra. Martha Cecilia Daza Espinosa. Advisor Dr. Markus Hans Oliver Doerr

Introduction

Propranolol (1-iso-propylamino-3-(1-naphthoxy)-2-propanol) is a non-cardioselective β-blocker (Figure 1). It is reported to have membrane-stabilizing properties, but it does not possess intrinsic sympathomimetic activity. Clinically propranolol is used as the hydrochloride salt in the management of hypertension, cardiac arrhythmias (Barrett, 1985), angina pectoris (Rabkin et al., 1966). It is also used to control anxiety disorders (Steenen et al., 2016), post-traumatic stress disorder (Giustino et al., 2016). Besides, propranolol is used for the treatment of infantile hemangioma, the most common childhood vascular tumor (Leaute-Labreze et al., 2016).

Figure 1

(R,S)-propranolol

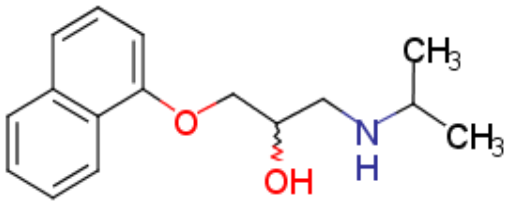

The desired therapeutic effect is associated with the (*S*)-enantiomer (Jia et al., 2015). (*S*)-propranolol is 100 times stronger β-adrenergic receptor antagonist than the (*R*)-enantiomer (Neri, 2015). The administration of the racemic propranolol mixture causes side effects such as bronchoconstriction (Bangalore, Messerli, et al., 2007; Bangalore, Parkar, et al., 2007) and, insulin resistance (Khan et al., 2007). Hence, the design of strategies for obtaining (*S*)- and (*R*)-propranolol in enantiomerically pure forms continues to be a critical area of research including enantioselective synthesis (Sasai et al., 1993; Veloo & Koomen, 1993) and chemoenzymatic synthesis (Kamal et al., 2004; Zelaszczyk & Kiec, 2007). Several approaches have also reported the enzymatic

resolution of (*R*,*S*)-propranolol through lipase-catalyzed transesterification and hydrolysis reactions (Barbosa et al., 2010; Chiou et al., 1997; Escorcia et al., 2013).

The lipases, triacylglycerol hydrolases, E.C.3.1.1.3, under natural conditions catalyze the hydrolysis of carboxylic ester bonds in hydrophobic compounds such as triglycerides. Additionally, lipases under non-aqueous conditions (Salihu & Alam, 2015), their function can be redirected towards alcoholysis, esterification, interesterification and acyl-transfer reactions (Ansorge-Schumacher & Thum, 2013; Naik et al., 2010; Turki, 2013); therefore, lipases are currently considered one of the most important enzymes for biotechnological applications(Ansorge-Schumacher & Thum, 2013; Ghanem, 2007; Ghanem & Aboul-Enein, 2004; Gotor-Fernández et al., 2006). *Candida antarctica* lipase B (CalB) has been used for kinetic resolution of several substrates, e.g., profen esters (Qin et al., 2013), secondary alcohols (Ursoiu et al., 2012), amines (Busto et al., 2011), amino acids (Ferrari et al., 2014), and amino alcohols (Joubioux et al., 2013).

The (*R*)- enantioselective *O*-acylation of (*R*,*S*)-propranolol by CalB with vinyl acetate in toluene as solvent (Escorcia et al., 2013) gave (*S*)-propranolol with an enantiomeric purity of 96% and relative low conversion rate (Figure 2). The Enantiomeric ratio (*E*) of reaction was 63. These results are comparable to other reactions catalyzed by other lipases from *Pseudomonas cepacia, Pseudomonas fluorescens,* and *Rhizopus niveus* (Barbosa et al., 2010).

The (*R*)- enantioselective *O*-acylation of (*R,S*)-propranolol catalyzed by CalB has been studied by our group using different computational approaches: Molecular Docking (Escorcia et al., 2013) and Quantum Mechanics /Molecular mechanics (QM/MM) hybrid calculations in combination with Molecular Dynamics (MD) (Escorcia et al., 2014) and the reaction barriers for conversion of (*R*)- and (*S*)-propranolol were calculated.

Figure 2

General visualization of the CalB catalyzed acetylation of (R,S)-propranolol. Adapted from Escorcia et al., 2013.

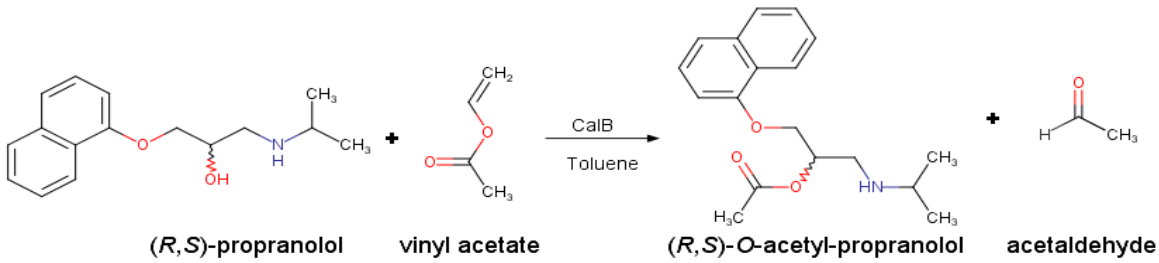

The energy barrier for the transformation of (*R*)-propranolol to *O*-acetylpropranolol was 4,5 kcal/mol lower than that of the reaction of (*S*)-propranolol. This difference in activation energy barriers gave insights into the enantioselectivity of the reaction (Escorcia et al., 2017). Nevertheless, to characterize systems and chemical processes, the calculation of free energy gives better results than energetic barriers. Specifically, in enzymatic kinetic resolution, the enantioselectivity is the result of a difference in activation free energy between enantiomers, $\Delta_{(R\text{-}S)}\Delta G^{\ddagger}$, which is related to the enantiomeric ratio *E* as -RTln*E*. Furthermore, $\Delta_{(R\text{-}S)}\Delta G^{\ddagger}$ is related to the difference in activation enthalpy and entropy as $\Delta_{(R\text{-}S)}\Delta G^{\ddagger} = \Delta_{(R\text{-}S)}\Delta H^{\ddagger} - T\Delta_{(R\text{-}S)}\Delta S^{\ddagger}$ (Ottosson et al., 2001). There are three probable scenarios to rationalize the experimental enantioselectivity found in terms of free energy. In all cases, free enzyme and (*R*)- or (*S*)- propranolol initially separated lead to the Michaelis complexes (*R*)-, (*S)*- MCCs (Figure 3). In the first one scenery, we can assume that MCCs formation proceeds with similarly rate and is essentially barrierless for both enantiomers. MCCs formed are degenerated, and there is only different free energy activation for (*R*,*S*)-propranolol acylation. In the other scenarios, the enantioselectivity assumes that there are differences in binding free energy for MCC formation and different free energy activation for (*R*,*S*)-propranolol acylation. In all scenarios, the enantioselectivity is a consequence of the

difference in free energy of activation for the enantiomers $\Delta_{(R\text{-}S)}\Delta G$ at the enantioselective step of the reaction.

Figure 3

*Activation free energy scenarios in the enantioselective acylation of (*R,S*)-propranolol. Left: MCCs formed are degenerate, and there is only different free energy activation for (R,S)-propranolol acylation. Center: the MCC formed, and the tetrahedral intermediate have different free energy . Right: the MCC has different free energy, and the tetrahedral intermediates are degenerate.*

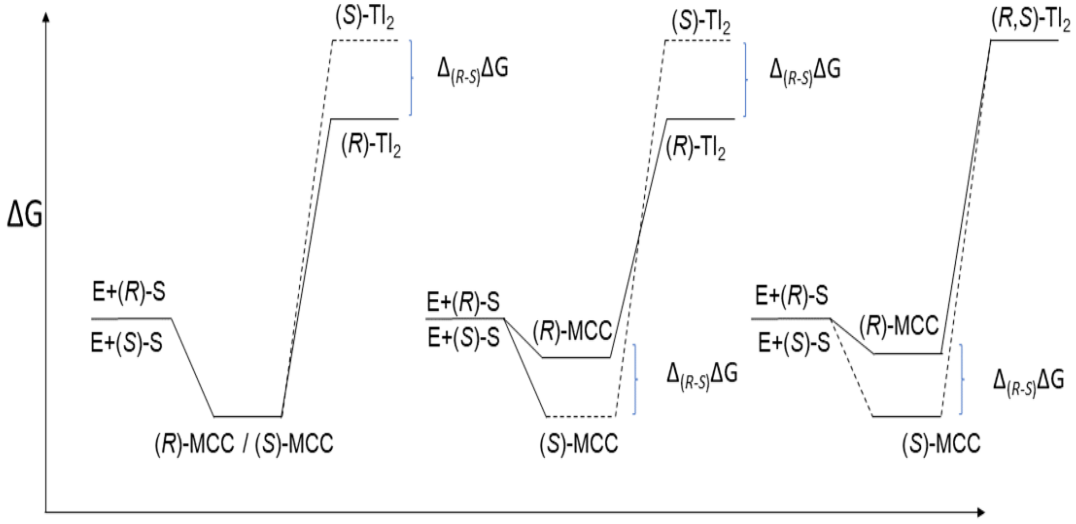

It has been shown that differences in both the enthalpic and the entropic components of the free energy of activation are important to enantioselectivity (Galunsky et al., 1997; Ottosson & Hult, 2001; Overbeeke et al., 1998; Sakai et al., 1997; Van Pham et al., 1989). The entropy can be related, loosely speaking, to the size of the configuration space available to the system at a given temperature (Senn et al., 2009). The differential activation free energy ($\Delta_{(R\text{-}S)}\Delta G^{\ddagger}$) nor differential activation entropy ($-T\Delta_{(R\text{-}S)}\Delta S^{\ddagger}$) are not accounted in any theoretical or experimental work for (*R*)-enantioselective *O*-acylation of (*R,S*)-propranolol catalyzed by CalB until now.

This doctoral dissertation aimed to gain insights into the role of the entropy and analyzes the configurational space in the enantioselective acylation of propranolol catalyzed by lipase B of *Candida antarctica* using a realistic representation of the catalytic system.

In the first place, a detailed analysis of Michaelis and Near-attack complexes (NACs) of the enantioselective step of the acylation of (*R,S*)-propranolol using QM/MM molecular dynamics was performed. The NACs approach, in several cases, permitted to explain the origin of the catalysis or reproduce the catalytic effect. The results indicate that the NACs approach is helpful to gain insights of configurational space between the MCC and the TI-2 formation. Additionally, the effect of different initial velocity distribution on NACs populations was not known, in enzyme kinetic resolution reaction, until the development of this thesis (Barrera Valderrama et al., 2018). Then the time evolution of Tetrahedral Intermediate (TI) at enantioselective step of the reaction was performed. The QM region, including all substrate and catalytic triad amino acidic residues, was higher than in previous analysis (Escorcia et al., 2017). The analysis of the MD simulations of the MCCs and TIs was focused on the dynamic behavior of propranolol, essential hydrogen bond interactions for the catalytic process.

The free energy calculations were performed by QM/MM MD in combination with umbrella sampling and weighted histogram analysis approaches. Free energy profiles of (*R*)-propranolol in binding mode II and (*S*)-propranolol in binding mode I were highly endergonic. Even though these free energy barriers cannot reproduce the experimental enantioselectivity, they are qualitatively comparable to QM (B3LYP-TZVP)/MM results. The PES, calculated by QM/MM relaxed scan, results showed that the minimum energy reaction energy path for each conformational snapshot is influenced by the small structural fluctuations. The minimum energy reaction energy paths that connect to MCC or EPC showed an appreciable propensity: There is one energetic barrier previous

to TI-2 formation from MCC, and there is another energetic barrier, smaller than the latter, to produce the EPC. The finite-temperature effect was calculated as the difference between PMF and PES. This effect was interpreted as entropy effect. The role of the entropy in the *O*-acylation of the propranolol catalyzed by CalB is to increase the energy of the TI-2. In general, the effect of the entropy can reach values of ~8kcal/mol.

This doctoral dissertation consists of six chapters plus appendices and is organized as follows. Chapter 1 contains a theoretical background of (*R*,*S*)-acylation of propranolol catalyzed by *Candida antarctica* lipase B, including experimental and computational approaches. The microscopic basis of the enantioselectivity of lipases explained. Chapter 2 focuses in more detail on the theoretical approaches which were used in the following chapter; this chapter should be welcome by those in the field of computational enzyme catalysis. Chapter 3 describes the analysis of configurational space before the enantioselective step of the reaction by the Near-attack conformation analysis. Chapter 4 describes the Molecular Dynamics of the tetrahedral intermediate at the enantioselective step of the reaction. All further work uses the models generated by the approaches described here in this chapter. Chapter 5 focuses on free energy calculation and the elucidation of the role of the entropy from the Michaelis complex to the Enzyme-Product complexes. Chapter 6 presents the summary and general conclusions.

1. Objectives

1.1 Overall Objective

Contribute to a better understanding of the role of the entropy in the enantioselectivity of acylation of the propranolol catalyzed by lipase B from *Candida antarctica*, using as a donor of acyl vinyl acetate and toluene as solvent.

1.2 Specific Objectives

Obtain and analyze the minimum energy pathways for the acylation reaction of the (*R,S*)-propranolol catalyzed by *Candida antarctica* lipase B.

Obtain and analyze the free energy profile for the acylation reaction of (*R*,*S*)-propranolol catalyzed by *Candida antarctica* lipase B.

Evaluate the differences between minimum energy paths and free energy profiles for the acylation reaction of (*R*,*S*)-propranolol catalyzed by *Candida antarctica* lipase B.

List of papers

This thesis has contributed to the following publication:

Barrera Valderrama, D. I., Doerr, M., & Daza E, M. C. (2018). Función de los confórmeros de ataque cercano en la acilación enantioselectiva del (R,S)-propranolol catalizada por lipasa B de Candida antarctica. Revista Colombiana de Biotecnología, 20(1), 16–30. https://doi.org/10.15446/rev.colomb.biote.v20n1.73652

Manuscript draft:

Barrera Valderrama, D. I., Doerr, M., & Daza E, M. C. "Rol of the entropy during *O*-acylation of (*R,S*)-propranolol catalyzed by *Candida antarctica* lipase B" *In preparation to be submitted to Journal of Biotechnology.*

Participation in conferences:

Daniel I Barrera V., Markus Doerr, Martha C. Daza E. (2017) "Potencial de fuerza media de la *O*-acilación del (*R*,*S*)-propranolol catalizada por Lipasa B de Candida antarctica". XVII Congreso Colombiano de Química. Bucaramanga, octubre 25 al 27.

Daniel I Barrera V. Markus Doerr, Martha C. Daza. (2016) "Comparison of reaction coordinates in the enantioselective step of the acetylation of (*R*,*S*)- Propranolol Catalyzed By Candida Antarctica Lipase B" The 56th Sanibel Symposium by the University of Florida Quantum Theory Project (QTP), St. Simons Island, GA, USA, February 14-19.

Daniel I Barrera V., Markus Doerr, Martha C. Daza E. (2016) "O-acylation of (*R*,*S*)-propranolol catalyzed by *Candida antarctica* lipase B". VI Encuentro nacional de químicos teóricos y computacionales y III Escuela colombiana de ciencias moleculares Bogotá, septiembre 20 al 26.

Daniel I Barrera V., Andrés Escorcia, Markus Doerr, Martha C. Daza. (2014) “Effect of mutations I189S and T138S on the population of Near attack conformations during the *O*-acylation of (*R*,*S*)-propranolol catalyzed by *Candida antarctica* Lipase B”. 10th Triennial Congress of the World Association of the Theoretical and Computational Chemists (WATOC-2014), Santiago, Chile, October 5th to 10th.

Daniel I Barrera V., Andrés Escorcia, Markus Doerr, Martha C. Daza E. (2014) “Efecto de las mutaciones I189S y T138S sobre la enantioselectividad de la Lipasa B de *Candida antarctica* en la acetilación del (*R*,*S*)-propranolol”. V Encuentro nacional de químicos teóricos y computacionales y II Escuela colombiana de ciencias moleculares Guatapé, abril 27 al 30.

Chapter 1. *Candida antarctica* lipase B and the *O*-acylation of (*R,S*)-propranolol

CalB is a globular protein composed of 317 amino acidic residues. It was isolated from the yeast *Candida antarctica*. This yeast also produces another lipase, which is called CalA and CalB. Several three-dimensional structures of CalB, and CalB complexes have been determined by X-ray crystallography Protein Data Bank codes: 3W9B, 4ZV7, 3GUU, 5A6V, 5A71, 4K6G, 2VEO, 1LBS, 1LBT, 1TCC, 1TCB and 1TCA. The last one has been used for modeling the acylation of (*R,S*)-propranolol (Barrera Valderrama et al., 2018; Escorcia et al., 2013, 2014, 2017). The secondary structure includes a core of 9 beta-pleated sheets surrounded by ten alpha-helices. The binding pocket entrance is defined by three alpha-helices and one loop from Val194 to Ala185 and form a channel with hydrophobic walls. The modeled structure of CalB in toluene explicit shows that the binding pocket is constituted by a large hydrophobic pocket above the catalytic triad and a medium pocket below it. The large pocket is created by Ile189 and Val190, Val154, Leu140, Leu144, T138, Asp134, Gln157 side chains. The medium pocket created by the alpha-helix ten residues Leu278 to Ala287 and the Trp104 at the bottom of the pocket. The catalytic triad is composed of Asp187, His224, and Ser105 (Uppenberg et al., 1994), and the oxyanionic hole, is composed by Gln106 and Thr40, complete the active site in CalB (Figure 4). His224 exerts a general acid/base catalysis during the reaction, which mediates in the acylation and deacylation of the Ser105. The deprotonated His224 acts as a base and enhances the nucleophilicity of the S105. The doubly protonated form His224 acts as an acid donating the excess proton. The oxyanionic hole stabilizes the negative charge developing on the carbonyl oxygen coming from the acyl donor.

It is composed of NH function in the backbone of Gln106 and Thr40 and OH function at the side chain of Thr40. Oxyanionic hole is located close to Ser105 (Figure 4).

Figure 4

Substrate binding pocket in Candida antarctica *lipase B. Amino acidic residues surrounding the entrance are represented in solid white translucent van der Waals surface. Catalytic triad is represented as magenta wires. The oxyanionic hole is represented by green wires. Crystal waters at hydrophilic external sites are shown. The representation was made using VMD software (Humphrey et al., 1996).*

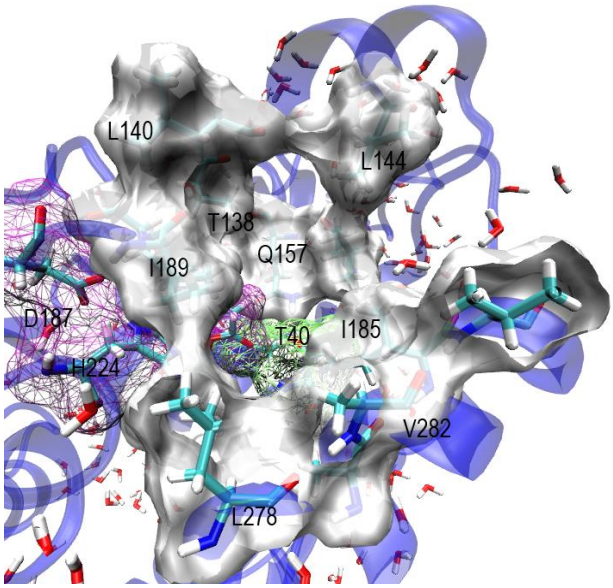

The proposed catalytic mechanism of the *O*-acylation of (*R*,*S*)-propranolol by CalB is similar to the serine proteases mechanism (Ghanem, 2007; Hedstrom, 2002), includes acylation and deacylation of residue Ser 105 and involves two tetrahedral intermediaries (TI-1 and TI-2). TI-1 is the result of the nucleophilic attack of the Ser 105 to the acyl-donor substrate, vinyl acetate, and the product is the acylated enzyme, the AcetylCalB (AceCalB). TI-2 is the product of the nucleophilic attack of the -OH function of (*R,S*)-propranolol, acyl acceptor substrate, to the AceCalB, which ultimately leads to the formation of the propranolol ester and the restitution of the enzyme (Figure 5). Enzyme-substrate complexes called Michaelis complexes (MCCs) are

Figure 5

Reaction mechanism proposed for (R,S)-propranolol acylation by Candida antarctica *Lipase B. Arrow 1 shows the enzyme acylation. Arrow 2 shows the enzyme deacylation and is the enantioselective step of the reaction. The first substrate is vinyl acetate. (R,S)-propranolol is the second substrate. The final reaction product is (R,S)-acetyl-propranolol.*

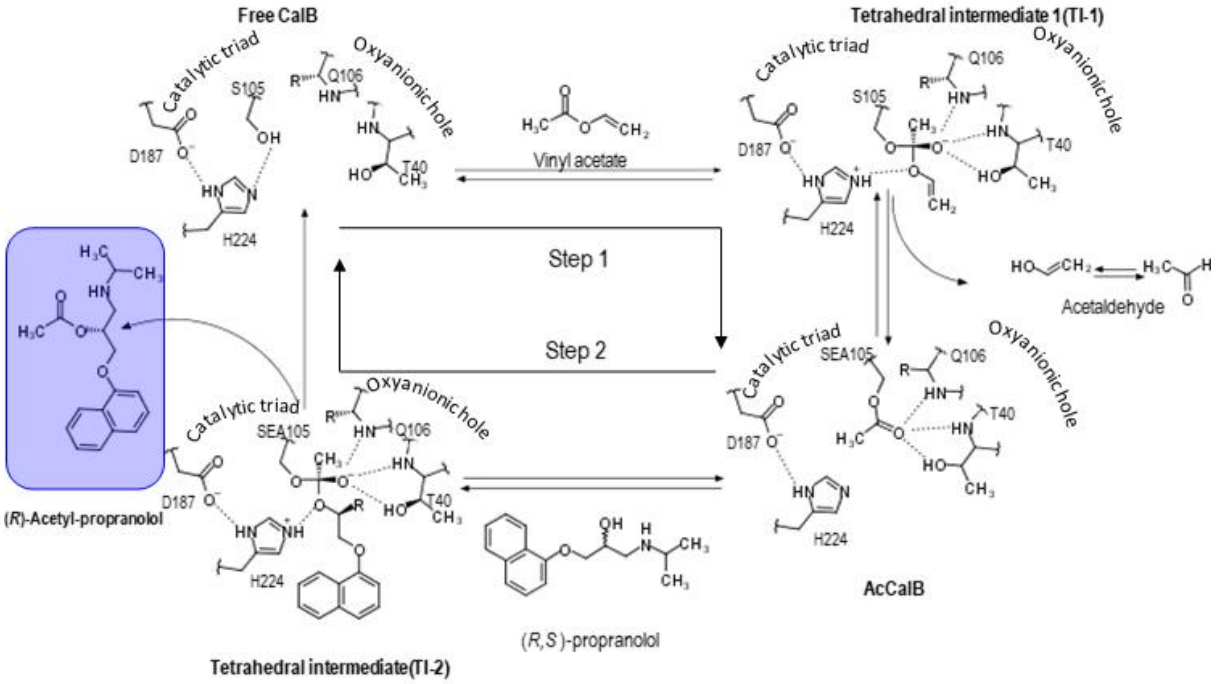

formed before the formation of tetrahedral intermediates. MCCs are stabilized by hydrogen bonds at catalytic triad and oxyanionic hole. In contrast to what is commonly accepted for lipase-catalyzed reactions, QM/MM calculations show that TI-2 is not a transition state analog in the CalB-catalyzed *O*- acetylation of (*R*,*S*)-propranolol in toluene (Escorcia et al., 2017).

Candida antarctica lipase B (CalB)-catalyzed the acetylation of (*R,S*)-propranolol using vinyl acetate as an acyl donor and a mixture of toluene/methanol as solvent *in vitro*. Hydrolysis and alcoholysis of vinyl acetate occurred as a consequence of the presence of residual water and methanol in the reaction medium, in addition to the acetylation of propranolol. This reaction

catalyzed by CalB free or immobilized slightly change the acetylation reaction rate but not the chemo- and enantio-selectivity. Exclusive formation of the *O*-acetyl-propranolol was observed. CalB was also found to be enantioselective (E = 61-63), favoring the transformation of *R*-propranolol (Escorcia et al., 2013).

The molecular modeling studies of this reaction have been focused on the deacylation step, which is responsible for the enantioselectivity. The most important findings are briefly reported here: Molecular docking between (*R*,*S*)-propranolol and AceCalB shows reactive AceCalB-propranolol complexes for *O*-acylation reaction, which is consistent with the chemoselectivity reported experimentally. In these reactive complexes, both propranolol enantiomers fit into the AceCalB binding pocket in two binding modes (Figure 6), with the naphthyl or amino group positioned either at the bottom or the top of the binding pocket (Escorcia et al., 2014). The dynamic behavior of the Michaelis complexes was studied by multiple molecular dynamics simulations in explicit toluene. The analysis of the MD QM (SCC-DFTB)/MM(CHARMM) trajectories shows that different reactive conformations of (*R*)- and (*S*)-propranolol exist, which may be transformed to the corresponding TI-2. These reactive conformations differ in their temporal stability and ability to reach the corresponding transition states. The CH-π interactions established between the naphthyl group of propranolol and the surrounding protein residues at binding pocket are the significant source of the stabilization of propranolol with its OH function near to the catalytic

Figure 6

Binding modes of (R,S)-propranolol in AceCalB. A detailed view of the enzyme binding pocket is shown on the left. Catalytic triad and oxyanionic hole are represented by magenta and green wires. Amino acidic chains of secondary structures surrounding generate two asymmetric pockets. In binding mode I (up to the right), the naphthoxy side chain of propranolol lies in the large pocket of CalB. In contrast, the isopropylamine side chain in the medium pocket and may extends toward the entrance of the binding pocket. In binding mode II (down to the right), the former lies in the medium pocket and the latter in the large pocket.

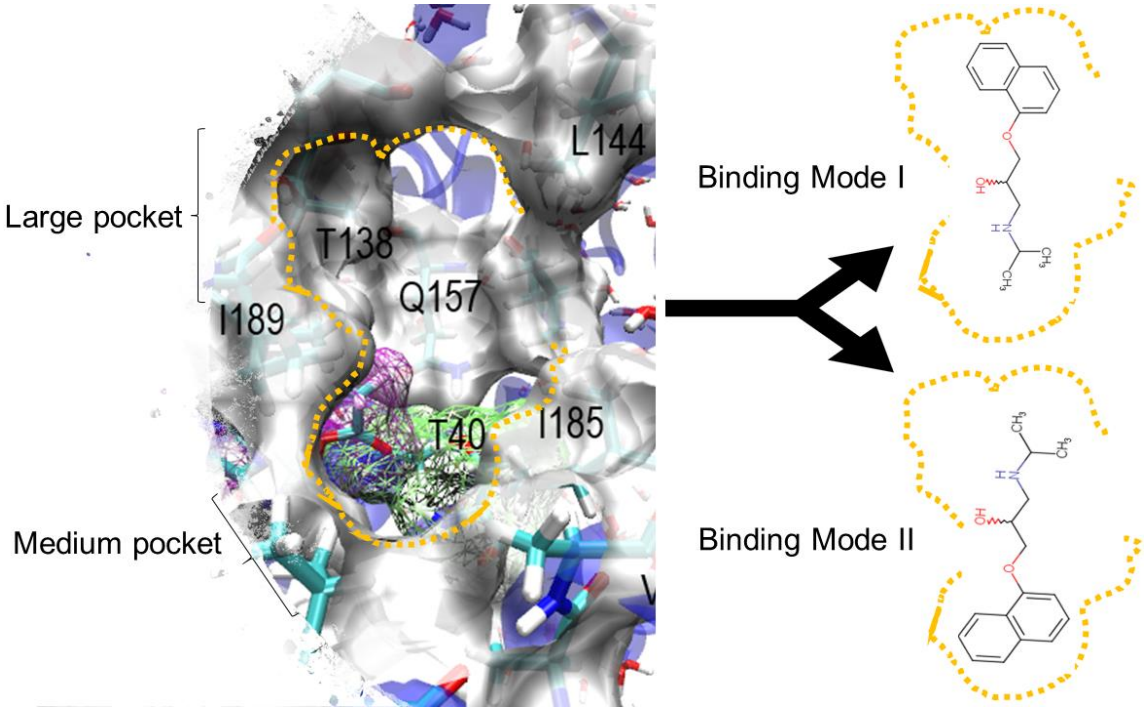

residues. Ile189, Ala282 and Leu278 have been identified as crucial residues for CH- π interactions with *R*-propranolol both in binding mode I and II (Escorcia et al., 2014).

QM (B3LYP/TZVP)/MM(CHARMM) calculations show that the transformation of (*R*)-propranolol to *O*- acetylpropranolol is more exothermic than (*S*)-propranolol acylation. The formation of the second tetrahedral intermediate (TI-2) is found to be the rate-limiting step in the transformation of both enantiomers. The reaction of (*S*)-propranolol in binding mode I is predicted to be slower than that of (*R*)-propranolol in binding modes I and II, with energy barriers for the

Figure 7

*QM(B3LYP/TZVP)/MM(CHARMM) energy profiles for the conversion of (R)- (a) and (S)- propranolol (b) to the O-acetylation in binding modes I and II. ORI-IV and OSI-IV correspond to different configurations of the tetrahedral configurations of (*R*)- and (*S*)- propranolol, respectively. Energies are given relative to the respective complexes between AceCalB and propranolol (Escorcia et al., 2017).*

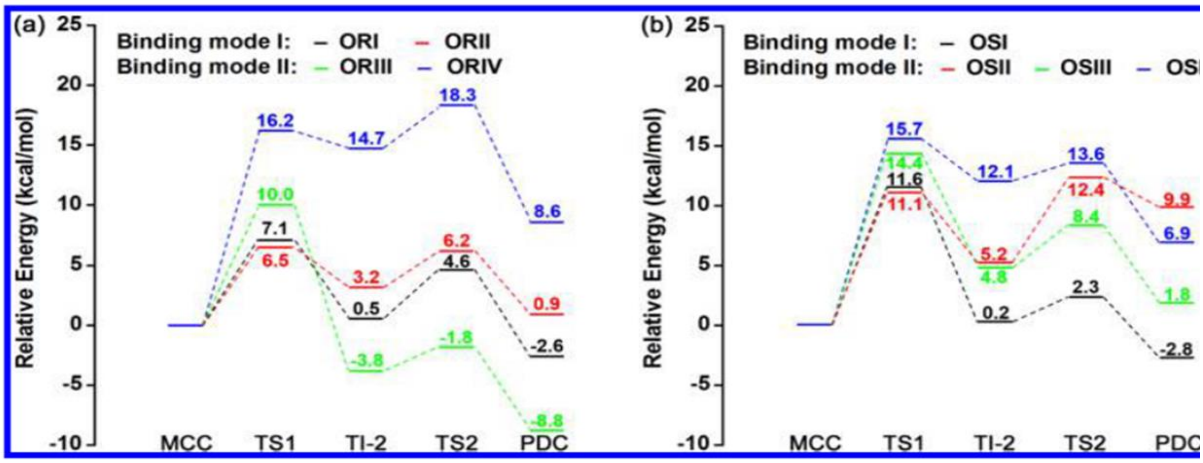

formation of TI-2 which are higher by 4,5 and 1,6 kcal/mol, respectively (**Figure 7**), (Escorcia et al., 2017).

The hydrogen bonds with the residues of the oxyanionic hole play an essential role in the energy profile of the reaction and the enantioselectivity. A weakening of these interactions as the reaction proceeds to the enzyme product complex appears to be the main reason for the unfavorable (endothermic) transformation of (*S*)-propranolol. Tetrahedral intermediates are considered structural and energetic analogs of the transition states in reactions catalyzed by CalB (Bocola et al., 2004; García-Urdiales et al., 2009; Nyhlén et al., 2008; Xu et al., 2010). Interestingly, in contrast to what is commonly accepted for lipase-catalyzed reactions, QM/MM calculations show that TI-2 is not a transition state analog in the CalB-catalyzed *O*- acetylation of (*R,S*)-propranolol in toluene (Escorcia et al., 2017).

Chapter 2 Molecular modeling in enzymatic catalysis
-Theoretical background-

2.1 Molecular modeling in enzymatic catalysis

In computational enzymology, the aim is to understand catalytic events at the atomistic level. Computer models for this purpose must comply with the following criteria: Properly reproduce the covalent and non-covalent interactions of the system under study, make an appropriate description of the breaking and formation of chemical bonds on the system, and include the effects of the environment (the solvent and the crystallization water molecules) on the enzyme and the substrate. In principle, methods based on Quantum Mechanics (QM) can satisfy all criteria of molecular models in enzymatic catalysis. There are several approaches to solve this equation in multi-electronics systems, which can be classified in methods *ab initio*, Theory of the functional of the density (DFT), and semiempirical methods (Foresman & Frisch, 1996; Lewars, 2011; Matta, 2010). The computational effort with *ab initio* or DFT methods is too big to treat an enzyme. Otherwise, the methods based on the empirical formulation of the potential energy of the molecules (Molecular Mechanics (MM)) allow to study systems with several thousand atoms with a relatively low computational cost. Unfortunately, MM methods do not allow to recreate the break or the formation of chemical bonds that, in essence, allows the change of substrate to product in enzymatic reactions, to the exception of reactive force fields. Another drawback associated with MM methods is that there must be parameters for all the molecules under study. The above allows us to conclude that neither the QM methods nor the MM methods separately can understand the

catalytic events to an atomistic level, including the effects of the solvent and changes in the chemical environment close to the active site of the enzyme. The QM / MM hybrid methods were designed to join the advantages shown separately from the QM and MM methods. It is essential to remark that molecular modeling in enzymatic catalysis starts with the prediction of enzyme-substrate complexes using molecular docking approach typically. A brief description of molecular docking and QM/MM methods and free energy calculations will be presented here:

2.1.1. The Molecular Docking method

Molecular docking is a computational procedure that attempts to predict non-covalent or covalent binding of macromolecules or, more frequently, of a macromolecule (receptor) and a small molecule (ligand) efficiently, starting with their unbound structures (Bianco et al., 2016; Sousa et al., 2006; Trott & Olson, 2011). The applications of this computational tool are the determination of the binding mode and site of a ligand on a protein, the prediction the absolute binding affinity between receptor and ligand, and the identification of the potential ligand for a given receptor target by searching a large ligand database, virtual database screening. The success in molecular docking is closed related to the energy scoring function that must be fast and accurate to describe the interactions between protein and ligand(s). Energy scoring functions can be classified into three basic types according to which they are derived: force field-based, empirical, and knowledge-based. Every energy scoring function has its advantages and limitations. The consensus scoring technique has been introduced to improve the probability of finding correct solutions by combining the scores from multiple scoring functions. The reader is encouraged to revise the perspective article of Huang for a deeper explanation of scoring functions (Huang et al., 2010).

The prediction of binding of *R*- or *S*- propranolol into AceCalB active site has been calculated using AutoDock Vina software (Trott & Olson, 2011). The general functional form of the conformation-dependent part of the scoring function AutoDock Vina is:

$c = \sum_{i<j} f_{(titj)}(r_{ij})$ where the summation is over all of the pairs of atoms that can move relative to each other, typically excluding 1–4 interactions, i.e., atoms separated by three consecutive covalent bonds. Here, each atom *i* is assigned a type *ti*, and a symmetric set of interaction functions f_{titj} of the interatomic distance r_{ij} should be defined. This value can be seen as a sum of intermolecular and intramolecular contributions:

$$c = c_{inner} + c_{intra}$$

The optimization algorithm, described in the following section, attempts to find the global minimum of c and other low-scoring conformations, which it then ranks. The predicted free energy of binding is calculated from the intermolecular part of the lowest-scoring conformation, designated as 1:

$$s1 = g(c1 - c_{intra1}) = g(c_{inter}1)$$

where the function *g* can be an arbitrary strictly increasing smooth function. In the output, other low-scoring conformations are also formally given *s* values, but, to preserve the ranking, using c_{intra} of the best binding mode:

$$s_i = g(c_i - c_{intra1})$$

The derivation of AutoDock Vina scoring function combines certain advantages of knowledge-based potentials and empirical scoring functions: it extracts empirical information from both the conformational preferences of the receptor-ligand complexes and the experimental affinity measurements. The hydrogen atoms are not considered explicitly. The interaction functions f_{titj} are defined relative to the surface distance

$$d_{ij} = r_{ij} - R_{ti} - R_{tj}$$

where R_t is the van der Waals radius of atom type *t*.

The weighted sum of steric interactions h_{titj} is identical for all atom pairs, hydrophobic interactions between hydrophobic atoms, and where are applicable, hydrogen bonding.

$$f_{(titj)}(r_{ij}) \equiv h_{titj}(d_{ij})$$

The steric terms are:

$$\text{gauss}_1(d) = e^{-(d/0{,}5\text{Å})^2}$$

$$\text{gauss}_2(d) = e^{-(d-3\text{Å})/2\text{Å}^2}$$

$$\text{repulsion}(d) = d^2, \text{if} d < 0; 0 \text{if} d \geq 0$$

The hydrophobic term equals 1, when $d < 0{,}5$Å; 0, when $d > 1{,}5$Å, and is linearly interpolated between these values. The hydrogen bonding term equals 1, when $d < -0{,}7$Å; 0, when $d > 0$, and is similarly linearly interpolated in between. In this implementation, all interaction functions f_{titj} are cut off at $r_{ij} = 8$Å. For more information, please read the Autodock Vina paper (Trott & Olson, 2011).

2.1.2. The QM/MM method

The QM / MM hybrid methods were designed to join the advantages shown separately from the QM and MM methods. The objective of these methods is to focus the computational effort on the site of interest in the protein (QM region) and use a more economically computational method (MM region) in the rest of the system under study. For detailed information of these methods has been reviewed by Thiel several times (Senn & Thiel, 2007, 2009; SennHM & Thiel W, 2007). The QM methods in a QM/MM approach can vary between semiempirical methods (high-speed), DFT

and *ab initio* methods (perturbational methods such as the Møller-Plesset perturbation theory or coupled cluster methods). The selection of the QM method in the exploration of the reaction route depends on the purpose of the study. Several explorations are usually carried out along the minimum energy path that connects reactants and products, via the transition state, to obtain the energy information.

Any system QM/MM (S) can be partitioned into the inner region (I) to be treated quantum-mechanically and the outer region (O) described by a force field. Because the two regions generally interact, it is not possible to write the total energy of the entire system only as the sum of the energies of the subsystems and coupling terms have to be considered. It will be necessary to take precautions at the boundary between the subsystems, especially if it cuts through covalent bonds (Figure 8). The canonical energy expression for an additive QM/MM method is: $\mathrm{E}^{\mathrm{add}}_{\mathrm{QM/MM}}(\mathrm{S}) = \mathrm{E}_{\mathrm{MM}}(\mathrm{O}) + \mathrm{E}_{\mathrm{QM}}(\mathrm{I}+\mathrm{L}) + \mathrm{E}_{\mathrm{QM-MM}}(\mathrm{I},\mathrm{O})$

Where $\mathrm{S} = \mathrm{QM/MM}$ is the entire system; *I* = inner subsystem, *O* = outer subsystem, and *L* = is (are) the boundary atoms atom(s). In this method, the E_{MM} calculation is performed on the outer subsystem only. Besides, there is an explicit coupling term, $E_{QM\text{-}MM}$ (*I,O*), which collects the interaction terms between the two subsystems. The coupling term used for all QM/MM calculations because of MM force field used (see below), and where:

$$\mathrm{E}_{\mathrm{QM-MM}}(\mathrm{I},\mathrm{O}) = \mathrm{E}^{\mathrm{b}}_{\mathrm{QM-MM}} + \mathrm{E}^{\mathrm{vdW}}_{\mathrm{QM-MM}} + \mathrm{E}^{\mathrm{Elec}}_{\mathrm{QM-MM}}$$

Two boundary approaches were used, the *General Hybrid Orbital* (GHO) method in chapters 4 and 5 and the *link atom* method for potential energy surface calculations in chapter 5. The GHO method recognizes a frontier atom, typically carbon, both as a QM atom and an MM atom. Thus, standard basis orbitals are assigned to this atom. These atomic orbitals on the frontier atoms are

transformed into a set of equivalent hybrid orbitals (typically, the frontier atom is of sp^3 hybridization type). One of the four hybrid orbitals, which points directly to the direction of the neighboring QM atom, is included in QM-SCF orbital optimizations, and is an active orbital. The other three hybrid orbitals are not optimized. Additionally, since the active orbital is being optimized in the SCF procedure, charge transfer between the frontier atom and the QM fragment is allowed. Consequently, the GHO method provides a convenient way for a smooth transition of charge distribution from the QM region into the MM region (Figure 8) (Gao et al., 1998).

The *Link atom* method introduces an additional atomic center "L" (usually a hydrogen atom) that is not part of the real system. It is covalently bound to Q1 and saturates its free valency. The new added atom introduces three structural degrees of freedom does not present in the real system and can present some optimization problems and introduces artificial interaction with other atoms. Despite these issues, the *Link atom* method is the most popular and widely used boundary method (Figure 8) (Senn & Thiel, 2007).

Figure 8

QM/MM approach and Boundary methods used. Left: QM/MM system is partitioned in the outer (O), and the inner system (I), boundary region (L), is represented in red. Centre: Labeling atom at the boundary between the outer region (MM) and inner region (QM) in the link atom method. The L letter represents the new added atom when the covalent bond Q_1-M_1 is broken. Right: Labeling atom boundary between QM and MM regions in the GHO method. The set of localized atoms is placed on M_1 atom, only one is active for calculations and points to Q_1 atom. Adapted from (Senn & Thiel, 2007).

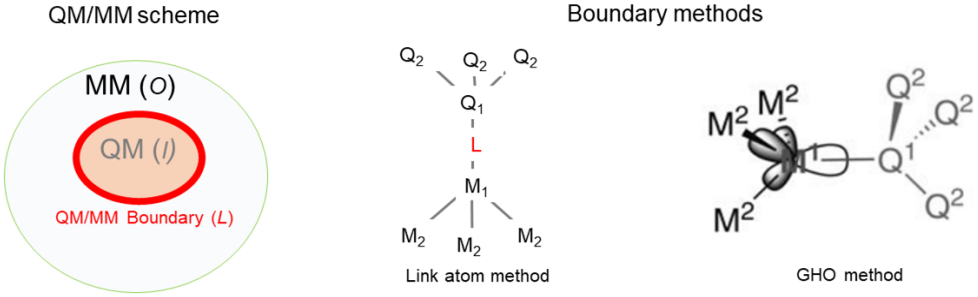

For the calculations of this dissertation the MM region was described by the CHARMM22 force field. In this approach, the energy is:

$$E_{MM} = \sum_{bonds} k_b(d - d_0)^2 + \sum_{angles} k_\theta(\theta - \theta_0)^2 + \sum_{dihedrals} k_\phi[1 + \cos(n\phi + \delta)]$$

$$+ \sum_{non-bondedpairsAB} \{\epsilon_{AB}[(\frac{\sigma_{AB}}{rAB})^{12} - (\frac{\sigma AB}{rAB})^6] + \frac{1}{4\pi\epsilon_0}\frac{q_A q_B}{rAB}\}$$

where d, θ, and φ designate bond distances, angles, and torsions, respectively; d_0 and θ_0 are the corresponding equilibrium values; and n and δ are the torsional multiplicity and phase, respectively. The bonded force constants are k_b, k_θ, and k_Φ. *rAB* is the non-bonded distance, and ε_{AB} and σ_{AB} are the van der Waals parameters between atoms A and B. q_A, q_B are atomic partial charges, and ε_0 is the dielectric constant.

2.1.2.1. Semiempirical QM methods. Many biomolecular QM/MM applications use DFT as the QM method due to its favorable cost/accuracy ration. Nevertheless, when the calculations including MD the semiempirical methods (Lewars, 2011), have been the most popular. In brief, semiempirical methods are an approximation to the Hartree-Fock approach (does not precisely apply to SCC-DFTB, which is an approximation to DFT), where only the valence electrons are treated, a very small basis set is used, and many interaction integrals are neglected. The remaining interactions are parameterized to avoid bad results. In this dissertation, several semiempirical methods were assessed: MNDO, AM1 (Dewar et al., 1985), PM3, OMx family (Tuttle & Thiel, 2008), and SCC-DFTB (Elstner et al., 1998), previous the Umbrella sampling calculations.

2.2. Molecular Dynamics

Newton's equation can be used to propagate the state of a complicated system forward in time. That is, if the initial positions and velocities for each atom are known or assumed, and all the forces

acting on each atom, as a function of the positions of the atoms, can be calculated, it is possible to calculate the positions and velocities a short time later. The basic principle for the calculation of positions and velocities is that if the position and velocity of the i*th* particle at time t_0 are $x_i(t_0)$ and $vi(t_0)$, then to propagate the positions forward, the following relation can be used:

$x_i(t1) = x_i(t_0) + v_i(t_0)\Delta t$, where $\Delta t = t_1 - t_0$. The new velocities are calculated from the old velocities in the same way:

$v_i(t_1) = v_i(t_0) + \Delta v_i(t_0)$, but using the Newton equation $F = ma$, or $F = mdv/dt$ to calculate the change in velocity:

$\Delta v_i(t_0) = \frac{F_i(t_0)}{m_i}\Delta t$. The force on a particle is equal to the negative gradient of the potential energy of the particle. In all cases where molecular dynamics calculation where performed: chapters 3 to 5, the propagation of the velocities and positions of atoms were calculated using the Verlet algorithm. This algorithm is derived from two Taylor series explanations of the coordinates of one particle, one at time $t + \Delta t$ and other at $t - \Delta t$. Hence, two sets of coordinate values are used, those at t and at $t - \Delta t$.

$v_i(t) = \frac{x_i(t+\Delta t) - X_i(t-\Delta t)}{2\Delta t}$.

For a deeper explanation, the reader is encouraged to read the following references (Mackerell, 2004; Schlick, 2010)

2.3. Free energy calculations

Free energy is particularly useful in quantitatively characterizing chemical reactions. The macroscopic observation of enantioselectivity can be related to free energy differences, and a connection must be made to molecular modeling. To this end, Molecular Dynamics simulations at

finite temperature are run, generating trajectories *via* integration the Newton's equation of motion, see above. Thus it is possible to gain access to thermal quantities like free energy or entropy as differences to reference. Specialized sampling techniques are needed to obtain reliable ΔG. All free energy calculations in this dissertation were performed using the *Umbrella sampling* approach; therefore, a proper description is necessary.

Torrie and Valleau in 1977 described the *Umbrella sampling* method to compute free energy differences to investigate a phase transition region (Torrie & Valleau, 1977). One of the early users of this method for biomolecular systems were Karplus and coworkers who calculated the potential of mean force (PMF), the reversible work for the rotation of a tyrosyl ring on the surface of a protein (Northrup et al., 1982). The PMF can be converted into a free energy of activation by multiplication with a correction factor (Schenter et al., 2003). Since we study differential PMFs this correction term is assumed to cancel out. For this reason, the PMF is supposed to be the one-dimensional free energy surface (Callender & Dyer, 2015; Truhlar, 2015).

The foundation of *Umbrella sampling* is the distribution function $\rho[\xi(r_{1,}r_{2,}\ldots,r_{n})]$of some reaction coordinate (RC) $[\xi(r_{1,}r_{2,}\ldots,r_{n})]$

When free energy barriers are present along the RC, standard sampling with unbiased molecular dynamics will not generate a useful distribution function. The simulation rarely visit the barrier regions and then spends most of its time in regions of low free energy of the RC To overcome this issue a biasing potential W $[\xi(r_{1,}r_{2,}\ldots,r_{n})]$is used in addition to the harmonic restraining potential, to truncate high barriers of activated processes, which forces the MD to visit the high energy regions of the RC, and thus, produce an even distribution. The general form of the biasing potential (umbrella potential henceforth) is harmonic $W = k(r_{A-B} - r_{C-D} - S)^2$where *k* is a force constant, *r* is an interatomic distance, and *S* is a variable that defines the equilibrium position. The

application this of umbrella potential allow to obtain a second distribution function ρ^* from which the original distribution ρ can be calculated as:

$$\rho[\xi(r_{1,}r_{2,}\ldots,r_n)] = \frac{[\rho^*[\xi(r_{1,}r_{2,}r\ldots,r_n)]*\exp(+\beta W)(\xi(r_{1,}r_{2,}\ldots,r_n))]}{\langle[\exp(+\beta W)(\xi(r_{1,}r_{2,}\ldots,r_n))]\rangle}$$

The PMF $W(\xi)$is defined from the average distribution function$\langle\rho[\xi(r_{1,}r_{2,}\ldots,r_n)]\rangle$,

$$W(\xi) = W(\xi^*) - k_B T\ln[\frac{\langle\rho(\xi)r_{1,}r_{2,}\ldots,r_n\rangle}{\langle\rho(\xi^*)r_{1,}r_{2,}\ldots,r_n\rangle}]$$

where ξ^* and $W(\xi^*)$are arbitrary constants. The average distribution function along the RC is obtained from a Boltzmann weighted average,

$$\langle\rho[\xi(r_{1,}r_{2,}\ldots r_n)]\rangle = \frac{\int dR\delta(\xi'[R]-\xi)e^{-U(R)/k_B T}}{\int dRe^{-U(R)/k_B T}},$$

where $U(R)$represents the total energy of the system as a function of coordinates Rand $\xi'[R]$is a function depending on a few or several degrees of freedom in the dynamical system, for example, a distance, and angle, a plain or more complicated function of the Cartesian coordinates of the system (Roux, 1995; Souaille & Roux, 2001). For the most practical problems, one biased simulation is not enough to sample the entire RC. It is necessary to perform several biased windows simulations to obtain the PMF. The biased distribution function obtained from the *i*th biased window simulation is

$$\langle\rho(\xi)\rangle_{(i)} = e^{-w_i(\rho)/k_B T}\langle\rho(\xi)\rangle\langle e^{-w_i(\rho)/k_B T}\rangle^{-1}$$

The unbiased PMF from the *i*th windows is

$$W(\xi) = W(\xi^*) - k_B T\ln[\frac{\langle\rho(\xi)r_{1,}r_{2,}\ldots,r_n\rangle_i}{\langle\rho(\xi^*)r_{1,}r_{2,}\ldots,r_n\rangle}] - wi(\xi) + F_i,$$

where F_i represents the free energy associated with introducing the umbrella potential and is defined as $e^{F_i/K_B T} = e^{-w_i(\rho)/k_B T}$To obtain a smooth free energy curve along all RC the constants $F_i$in all windows, sampling must be chosen to make adjacent curve fragments. To this end, different

approaches have been proposed avoiding discarding any information in combining the available data from umbrella sampling simulations.

The Weighted Histogram Analysis Method (WHAM) is an algorithm for unbiasing and combining umbrella sampling data. WHAM provides a built-in estimate of sampling errors, yields an accurate value of PMF by taking into account all simulations minimizing statistical errors, and also allows multiple overlaps of probability distributions (Kumar et al., 1992; Roux, 1995; Souaille & Roux, 2001). If the total distribution is spliced together from several slices, it may be recast as a weighted sum of individually unbiased distributions:

$$\rho[\xi(r_{1,}r_{2,\ldots},r_n)] = C\sum_{i=1}^{N} P_i{*}\rho[\xi(r_{1,}r_{2,\ldots},r_n)]$$

where C is a normalization constant and P_i are weighting functions subject to the condition and N is the number of individual simulations. The total distribution -for all equation derivation see the seminal article of Kumar (Kumar et al., 1992) - ρis:

$$\rho[\xi(r_{1,}r_{2,\ldots},r_n)] = C\frac{\sum_{(i=1)}^{N} n_i{*}\rho_i^{*}[\xi(r_{1,}r_{2,\ldots},r_n)]}{\sum_{j=1}^{N} n_j\exp[-\beta(W_j(\xi(r_{1,}r_{2,\ldots},r_n))) - F_i]}$$

n_i and j_i are the numbers of points that were used to estimate the distributions in windows *I* and *j,* respectively. The free energy constants F_i are calculated from the optimal distribution function, following an iterative procedure to solve self-consistently.

$$\exp(-\beta F_i) = \langle\exp[-\beta W_i(\xi(r_{1,}r_{2,\ldots},r_n))]\rangle$$

$$\exp(-\beta F_i) = \int \exp[-\beta W_i(\xi(r_{1,}r_{2,\ldots},r_n))]\rho[\xi(r_{1,}r_{2,\ldots},r_n)]d\xi$$

Chapter 3. Near-attack conformers during enantioselective acylation of (*R*,*S*)-propranolol catalyzed by *Candida antarctica* Lipase B

3.1 Introduction

The enantioselective step in this reaction is the transfer of an acyl group from the catalytic acylated serine to propranolol. The initial phase of this reaction involves the formation of Michaelis complexes, followed by the formation of near-attack complexes (NACs). NACs are a subgroup of MCCs which closely resembles the transition state. The structure of the NAC has to meet two criteria: (i) the distance of approach of the nucleophilic oxygen to the carbonyl carbon is between 3,2 and 2,8 Å, and (ii) the approach of the nucleophile is within a cone of 30° with the axis being 15° off of the normal to the carbonyl plane (Bruice & Benkovic, 2000; Lightstone & Bruice, 1996). In other words, NACs are a subspace of MCC configurational space. A graphic explanation of the NAC (Appendix A: Graphical representation of a Near Attack Conformer**)**.

The analysis of the NACs populations has in several cases permitted to explain the origin of the catalysis or to reproduce the catalytic effect (Giraldo et al., 2006; Griffin et al., 2012; Mazumder-Shivakumar et al., 2004; Štrajbl et al., 2003), predict the activity of CalB mutants (Linder et al., 2011). At the deacylation of the *O*-acetylation of (*R,S*)-propranolol was studied, and the experimental *E* was correlated to NACs formation observed for the *S*-propranolol (Escorcia et al., 2014).

Interestingly, Cino and coworkers using different initial velocities found clear differences in MD simulations with the same force field and starting structure (Cino et al., 2012). The result is in good agreement with Torres and Bruice results (Torres & Bruice, 2000), who found that the NACs population change almost 60% in MD replicates, changing the seed value for the random number generator that assigns the initial velocities for atoms. These two studies let consider that an exhaustive configurational space sampling of MCC by MD could provide insights about the relation between NACs populations and the reaction enantioselectivity. This Chapter aims to improve the understanding of the role of NACs in the enantioselectivity of the reaction (Figure 9). The NACs populations of seven CalB-propranolol complexes previously reported (Escorcia,

Figure 9

Enantioselective step in the acylation of (R,S)-propranolol catalyzed by CalB. Reaction occurs sequentially via MCC formation. The MCC evolves to Tetrahedral intermediate 2 (TI-2) who connects to Enzyme-product complex. Doted lines show the important hydrogen bond net in the catalytic process. Blue line shows the distance between oxygen, from the OH function at propranolol, and the carbonylic carbon at acetylated serine105 -c-. All shown distances are < 4 Å in MCC.

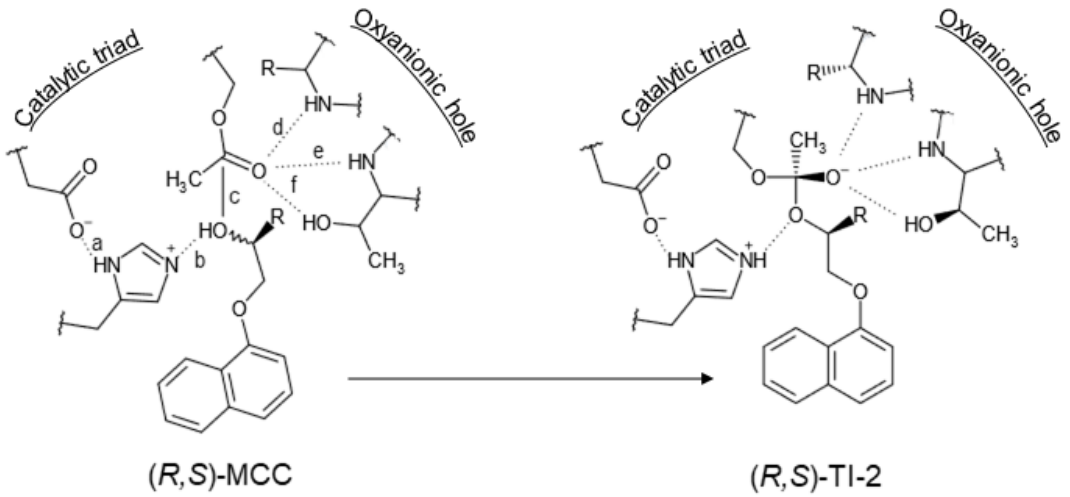

Molina, Daza, & Doerr, 2013) were studied. The results allowed testing the NACs approach in the enzymatic resolution kinetic context.

3.2 Methods

A detailed study of the MCCs and the NACs of the enantioselective step of acylation reaction of (*R*,*S*)-propranolol using six distributions of initial vector velocities and simulations of 2.5 ns, with a time step of 1 fs, and constant temperature, 300 K, for the production phase. The time evolution for the most important hydrogen bonds in the mechanism catalytic, populations of NACs, the distance between the oxygen of the hydroxyl group of propranolol, and the electrodeficient carbon of SEA105 was analyzed in detail. The detailed procedure used for the acylation of CalB was reported previously (Escorcia, Molina, Daza, & Doerr, 2013). A brief description of the modeling of acetylated serine 105 (Appendix B: Computational details for acetylated serine 105 in *Candida antarctica* Lipase B**)**. The initial structures of the MCC were selected from a work previously reported by our group (Escorcia et al., 2013). In binding mode I, two MCCs were selected for the *R*-enantiomer and three for the *S*-enantiomer and assigned the labels ORi-I, ORii-I, and OSi-I, OSii-I, OSiii-I (Figure 10). In binding mode II was the only MCC reported for each of the enantiomers and labeled as ORiii-II and OSiv-II (Figure 11). A detailed naming scheme of the MCC (Appendix C: Naming scheme of computer models**)**.

3.2.1. Molecular dynamics

The MD simulations were carried out using the CHARMM program (version 35b5) (Brooks, B. R. and Brooks, III, C. L. and Mackerell, Jr. et al., 2009). For each complex, six MD simulations with different initial velocity distributions were performed, corresponding to values of the random seed parameter *iseed*. A QM/MM approach was used to describe the system.

Figure 10

Michaelis complexes between AceCalB- and (R)- or (S)-propranolol in binding mode I selected for NACs population sampling (Barrera Valderrama et al., 2018).

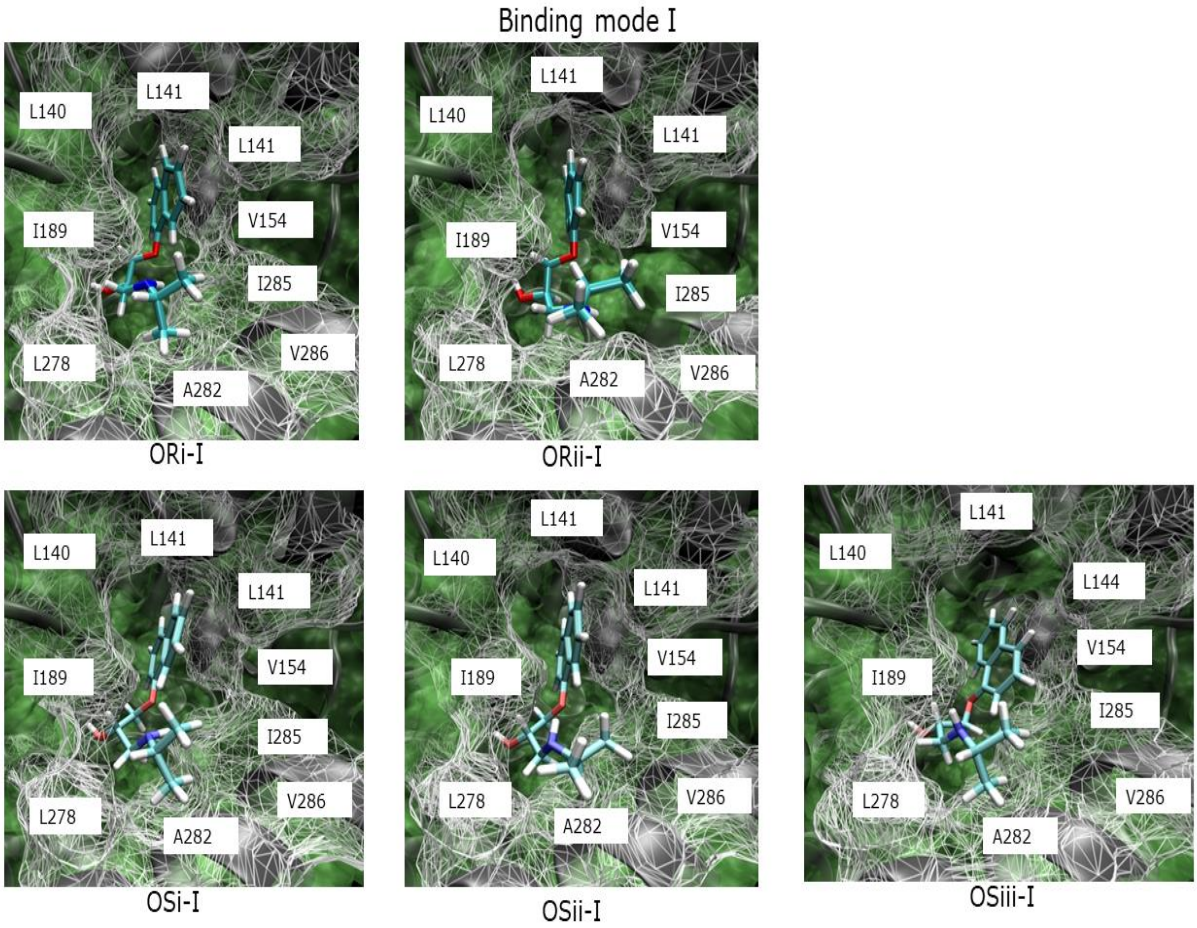

The semiempirical method Self Consistent Charge-Density Functional Tight Binding (SCC-DFTB) (Cui et al., 2001; Elstner et al., 1998; Pu et al., 2004) for (*R*)- or (*S*)- propranolol due to the lack of force field parameters was used. For the rest of the system: AceCalB, the crystallization waters, and the explicit solvent, the CHARMM22 force field was used (Mackerell, 2004). Solvent molecules were placed in a sphere centered on the C alpha of SEA105 with a radius of ***40***

Figure 11

Michaelis complexes between AceCalB- and (R)- or (S)- propranolol in binding mode II selected for NACs population sampling (Barrera Valderrama et al., 2018).

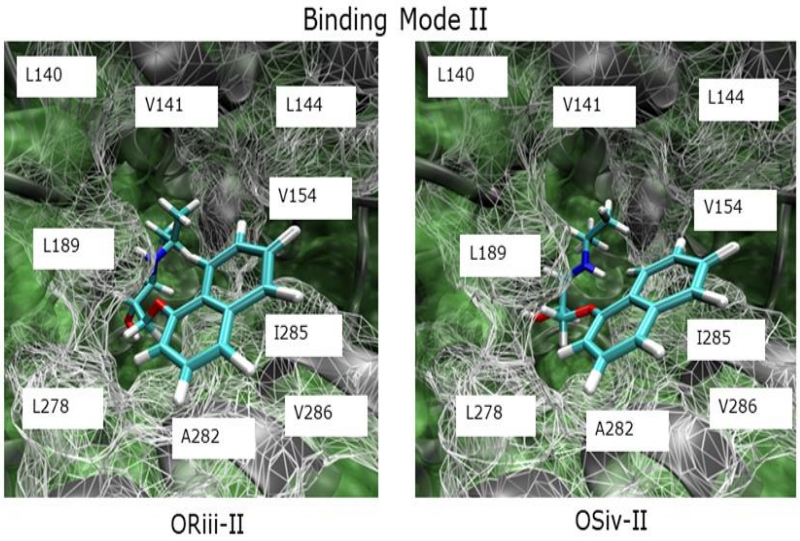

Å. Only one part of the protein could move freely, called the active region. The active region included all the amino acidic residues within a radius of 30 Å. Amino acid residues outside this radius remained fixed during MD. The sphere of explicit solvent was restricted with a quartic potential of spherical boundary initiating with -0,25 kcal/mol to 39,5 Å, increasing to greater distances (parameters: FORCE = 0.25, P1 = 2.25 and DROFF = 38.5). The SHAKE algorithm was used to restrict all distances involving hydrogen atoms (Ryckaert et al., 1977). The electrostatic interactions between the particles within a 14 Å radius of the SEA105 were treated additively

(Stote et al., 1991), and the electrostatic interactions at a larger radius were approximated by the multi-pole approach (Schlick, 2010). In the production phase, the Verlet integration algorithm was used. The simulation time was 2.5 ns, with a timestep of 1 fs. In total, 15 ns were modeled for each MCC.

3.2.1.2. Molecular dynamics analysis. In all MD trajectories, the last 2,4 ns were analyzed using VMD software (Humphrey et al., 1996). The search was focused on MCC evolution and the NACs population.

Figure 12

Secondary structures surrounding the AceCalB active site. The alpha helices 5, 6 (L316 to T159), a section of the alpha helix 10 (L278 to V286) and the loop (V194 to A185), orange color, are surrounding the catalytic residues and the residues of the oxyanionic hole: D187, H224, SEA105, and T40 and Q106 respectively (Barrera Valderrama et al., 2018).

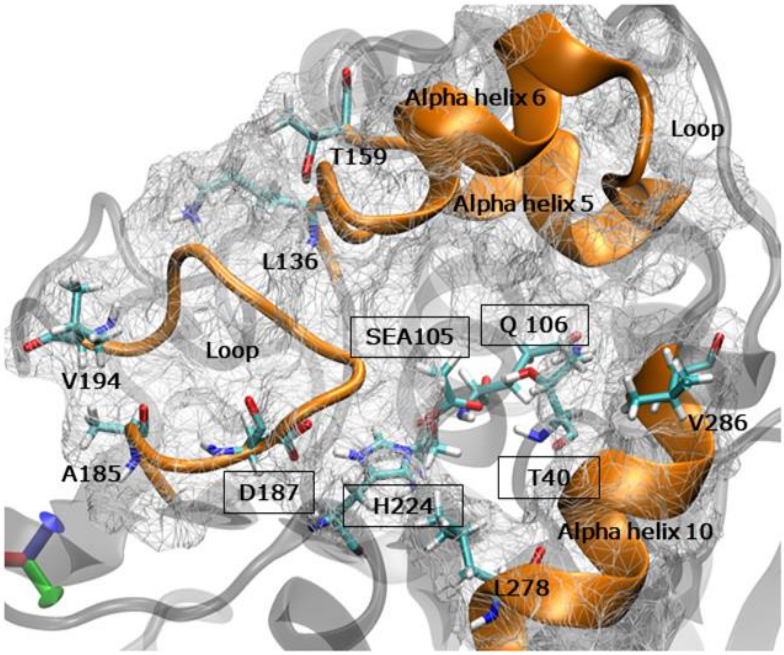

3.3 Results and discussion

The interatomic distance between H224 and D187, (distance -a- in Figure 9) shows the presence of this hydrogen bond in all trajectories. The average distance and angle were 1,9 +/- 0,5 Å and 163 +/- 10°. In principle, H224 can form this hydrogen bond with any of the oxygen at the side chain of D187, nevertheless this bond is only formed with noncarbonilyc oxygen. As an example, the evolution of these distances and angles in ORi-I and OSi-I complexes are shown (Figure 13). The time evolution of these distances and its related angles in all MD for these complexes (

Appendix D: Time evolution of the possible hydrogen bonds between D187 and H224 in ORi-I and OSi-I Michaelis complexes**)**.

The hydrogen bonds between carbonylic oxygen at SEA105 and OH or NH functions at the oxyanionic hole are represented by distances -d-, -e- and -f- (Figure 9). The hydrogen bonds -d- and -e- (Q106:NH-SEA105 and T40:OH-SEA105) are more stable than hydrogen bond -f- (T40:NH-SEA105). The hydrogen bonds at the oxyanionic hole were ≥ 4 Å in all simulations **(**Appendix E: Time evolution of the hydrogen bonds between at the oxyanionic hole in the ORi-I and OSi-I Michaelis complexes).

The distances are independent of the enantiomer or the binding mode (Table 1**)**. The MCC evolution was monitored by distances -b- and -c (Figure 9). Distance -b- (PROP:H-H224:N) can be understood as the proximity between the (*R*) or (*S*)-propranolol and the catalytic histidine and the distance -c- (PROP:O-SEA105: CE) can be understood as the proximity between the propranolol and the electrodefficient carbon at SEA105.

Figure 13

*Time evolution of the potential hydrogen bonds between D187 and H224. **A** ORi-I complex. **B** OSi-I Michaelis complex. The iseed number used was 314159. The distances are shown at the bottom of the graphic and the angles at the*

top. The schematic representation of the more stable hydrogen bond is represented as "distance -a-" in ***Figure 9****. In all cases were analyzed the last 2,4 ns of the productive phase of the QM-MM MD.*

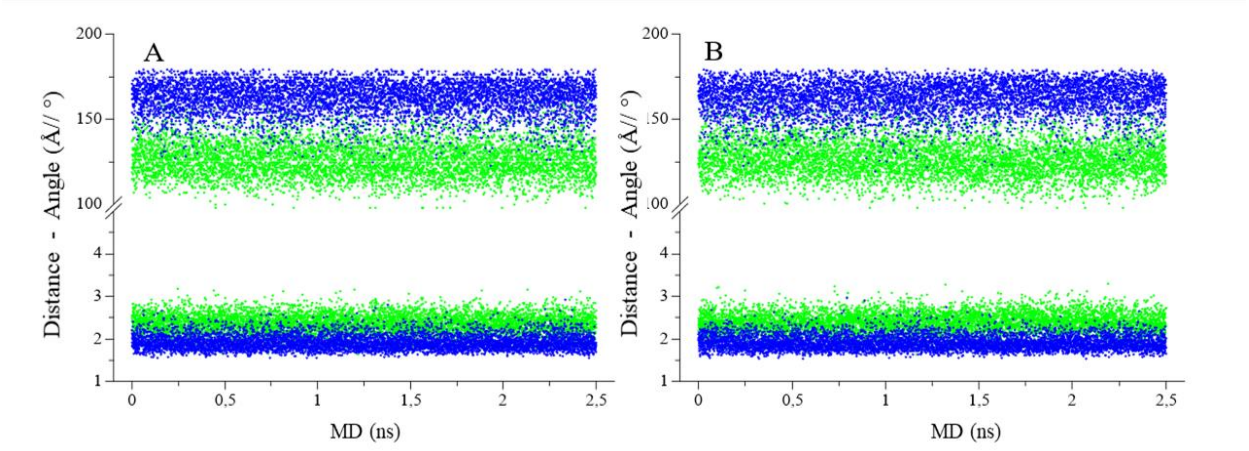

Table 1

Michaelis complexes evolution: Oxyanionic hole hydrogen bonds.

Average distances[a] and angles[b] in six molecular dynamics replicates			
Michaelis Complex	-d- Q106:NH-SEA105	-e- T40:OH-SEA105	-f- T40:NH-SEA105
ORi-I	2,2 (0,2) | 153 (13)	1,8 (0,2) | 162 (11)	2,2 (0,3) | 154 (35)
ORii-I	2,2 (0,2) | 153 (13)	1,8 (0,2) | 161 (11)	2,8 (0,2) | 152 (62)
OSi-I	2,2 (0,2) | 154 (13)	1,8 (0,2) | 162 (10)	2,2 (0,4) | 149 (47)
OSii-I	2,2 (0,2) | 152 (13)	1,8 (0,2) | 152 (11)	2,2 (0,4) | 162 (43)
OSiii-I	2,2 (0,2) | 153 (13)	1,8 (0,2) | 162 (11)	2,1 (0,3) | 151 (40)
ORiii-II	2,2 (0,2) | 153 (13)	1,8 (0,2) | 161 (11)	2,2 (0,4) | 154 (29)
OSiv-II	2,2 (0,2) | 152 (13)	1,8 (0,1) | 162 (10)	2,2 (0,3) | 151 (45)

[a] Values expressed in Ångström and [b] in degrees. Standard deviation in parenthesis. The dotted line separates the Michaelis complexes by Binding modes.

The distances -b- and -c- increased in almost all MD showing the diffusion of the substrate. This result can be interpreted as the low affinity of CalB for this substrate, as an example, the time evolution of these distances in the ORi-I and OSi-I complexes are shown (Figure 14 and in the Appendix F: Time evolution of the interatomic distances -b- and -c- in the ORi-I and OSi-I

Michaelis complexes**)**. The MCC is considered when the hydrogen bonds at the active site are ≥ 4 Å (Figure 9).

Figure 14

Time evolution of the distances -b- (PROP:H-H224:N), black dots, and -c- (PROP:O-SEA105:CE), red dots. ***A*** *ORi-I Michaelis complex.* ***B*** *OSi-I Michaelis complex. In both molecular dynamics, the iseed number used was 314159. The MCC evolution is monitored by these two distances. The MCC is considered when the hydrogen bonds at the active site and the distances -c- are ≥ 4 Å. In both molecular dynamics, the iseed number used was 314159 and 38455 in* ***A*** *and* ***B*** *respectively. In all cases were analyzed the last 2,4 ns of the productive phase of the QM-MM MD.*

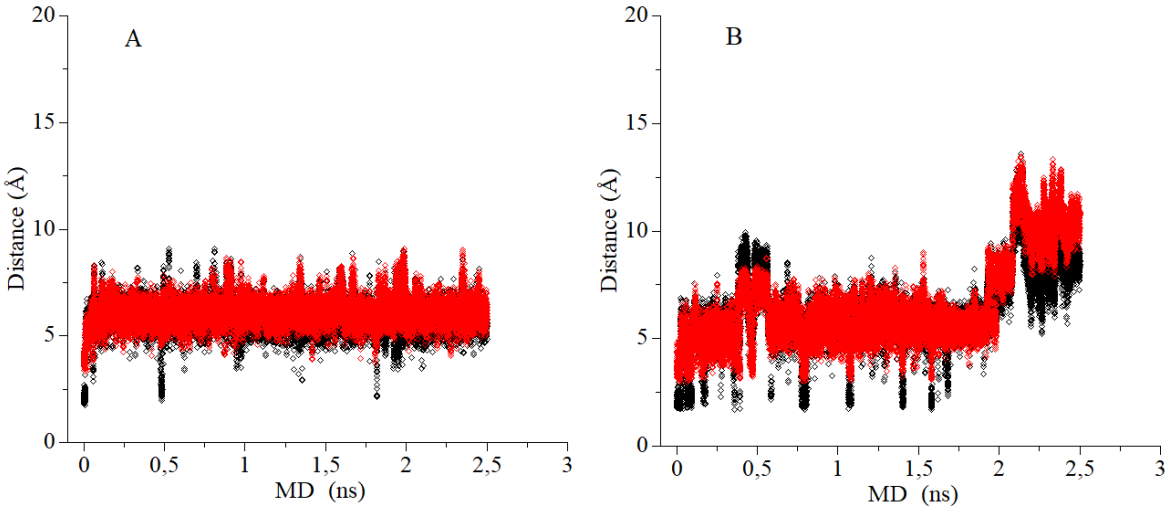

The distances -b- and -c- were higher than this value in almost all MD replicas (Figure 14). To gain insights of the increase in the distances -b- and -c- the root mean square deviation (RMSD) for all heavy atoms of the backbone of the AceCalB, the surrounding secondary structures of the active site (Figure 12), and for all heavy atoms in the substrate were calculated along all MD using as reference the initial structure.

In general, the full backbone of the AceCalB presents the lower RMSD values when is compared to the RMSD values of the surrounding secondary structures of the active site, as an example, the ORi-I and OSi-I RMSD evolution, using Iseed 314159 (Figure 15).

To compare results with other iseed numbers (Appendix G: Time evolution of the RMSD of the backbone of AceCalB and the surrounding secondary structures of the active site in the ORi-I and OSi-I Michaelis complexes). The apparent inflexibility of the full AceCalB backbone (black diamonds) disappear in the secondary structures surrounding the active site, especially in alpha-helix 5 and 6 (L136-T159, red diamonds) and alpha-helix 10 (L278-V286, blue diamonds) in Figure 15.

This is because of the protein mobility is restricted to the active region; see the methodology above. The alpha helix 5 and 6 and the alpha-helix 10 are parallel respect the active site in AceCalB (Figure 12), and this can explain the similarity on the RMSD behavior throughout the MD.

These results are not affected by iseed number modification Appendix G: Time evolution of the RMSD of the backbone of AceCalB and the surrounding secondary structures of the active site in the ORi-I and OSi-I Michaelis complexes).

Figure 15

*RMSD evolution of all heavy atoms of the backbone of the AceCalB (black diamonds), the surrounding secondary structures of the active site: L136-T156 (red diamonds), A185-V194 (green diamonds) and L178-V286 (blue diamonds). To see the localization of these sequences on the tertiary structure (**Figure 12**) ORi-I Michaelis complex. **B** OSi-I Michaelis complex. In both molecular dynamics, the Iseed number used was 314159. In all cases were analyzed the last 2,4 ns of the productive phase of the QM-MM MD.*

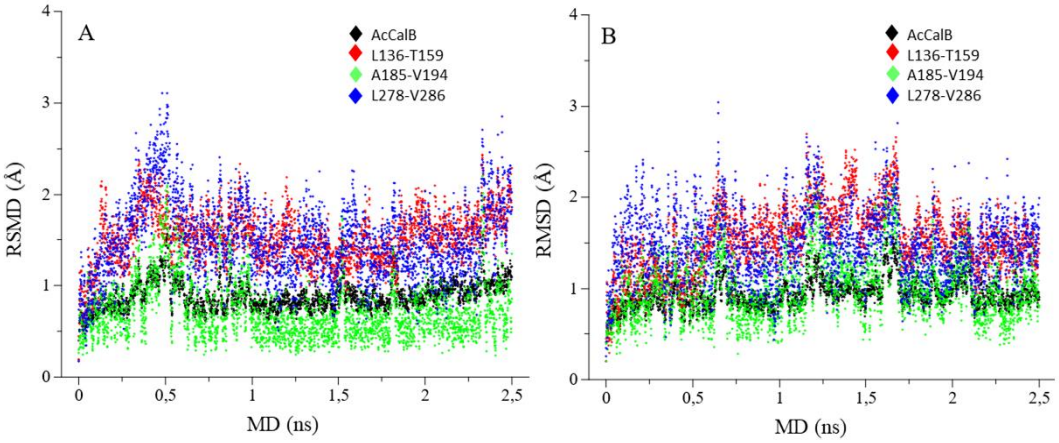

When we turn to analyze the RMSD of the (*R*)- or (*S*)-propranolol, the conformational changes are higher than conformational changes in the protein (Figure 16). Additionally, the RMSD evolution changes dramatically when the iseed number is changed. There is a tendency to diffusion of the MCC complexes indicating that the interaction between (*R*)- or (*S*)-propranolol and the toluene molecules are stronger than the interactions between (*R*)- or (*S*)-propranolol and active site residues.

The stable MCCs along the MD are considered as *reactive* MCCs for *O*-acylation of (*R,S*)-propranolol catalyzed by CalB. (Escorcia et al., 2014), the reactive MCCs populations found in our simulations were different between replicates (Table 2 and Figure 14).

The *reactive* MCCs lifetimes in this table clearly show that the binding mode I is more stable than the binding mode II. This propensity is maintained when the NACs lifetime is analyzed (Table 2). Interestingly, the effect of the iseed number on the MCC or NAC population is evident (Figure 15).

These results show that the system requires extensive sampling of the conformational space, which can be expected for such flexible substrate. Nevertheless is clear that (*S*)-propranolol Michaelis complexes lifetime are higher than (*R*)-propranolol Michaelis complexes lifetime and the binding mode I is favored at the beginning of the enzyme deacylation reaction (Figure 17).

Figure 16

Time evolution of the RMSD of the all heavy atoms on (R)- or (S)-propranolol using different iseed numbers: i) 314159 ii) 835 iii) 38455 iv) 55627 v) 1238 and vi) 234 in black, red, green, blue, turquoise and magenta diamonds. Examples of OR Michaelis complexes (Top row) and OS Michaelis complexes (Bottom row). In all cases were analyzed the last 2,4 ns of the productive phase of the QM-MM MD.

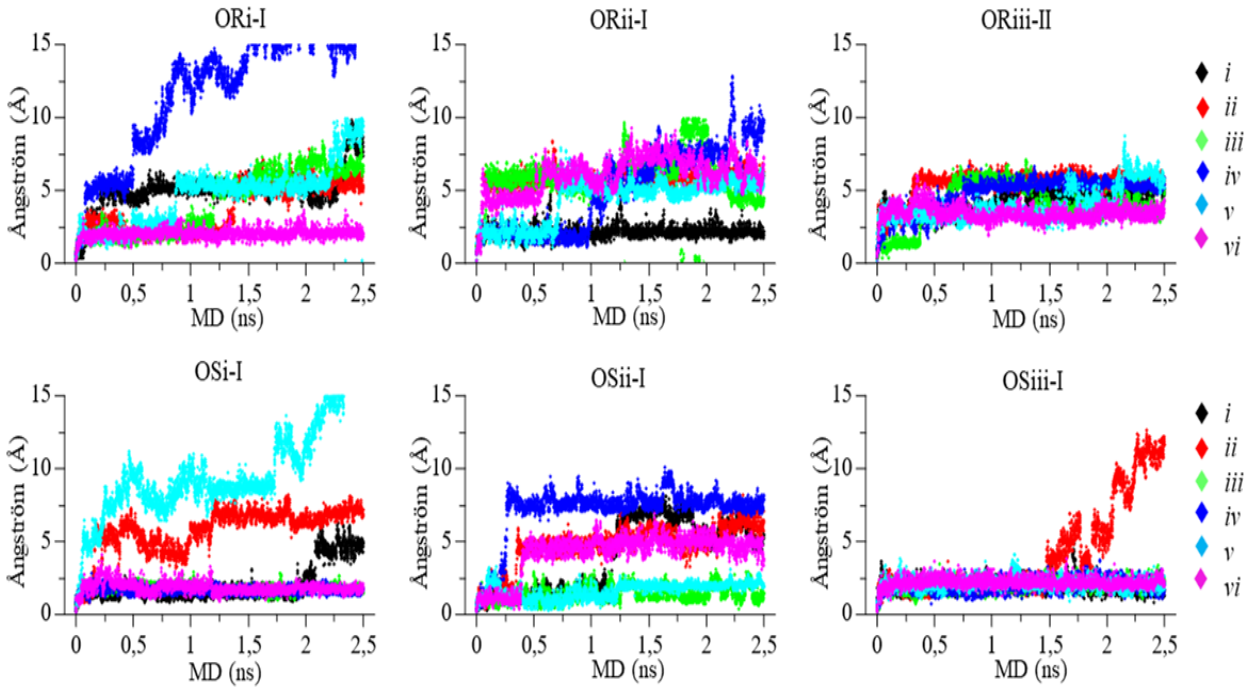

Figure 17

*Michaelis complexes **A** and Near-attack conformations **B** lifetime comparison during AceCalB deacylation step using different Iseed numbers: i) 314159 ii) 835 iii) 38455 iv) 55627 v) 1238 and vi) 234 in blue, orange, gray, yellow, dark blue and green columns. In all cases were analyzed the last 2,4 ns of the productive phase of the QM-MM MD.*

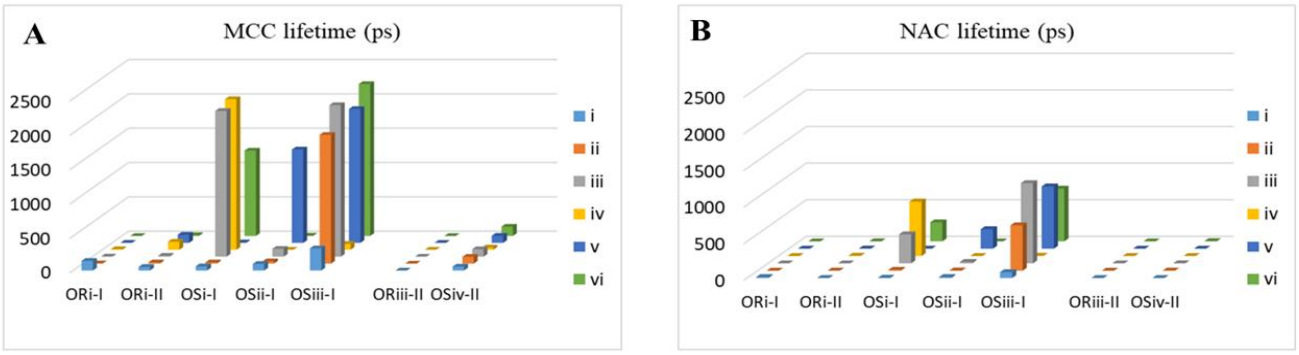

Table 2

Michaelis Complex and Near Attack Conformations lifetime (ps).

Binding Mode		i	ii	iii	iv	v	vi	Average	SD
					ORi-I				
	MCC	139,8	3,2	1,7	8,4	2,3	0,7	26	51,9
	NACs	13,5	0	0,2	0	0,2	0	2,3	5,1
	%	9,7	0	11,8	0	8,7	0	2,5	5,4
					ORii-I				
	MCC	52,1	18,1	13,9	117	119	12,2	55,4	50,7
	NACs	0,6	1,6	0	3,7	1,5	0,5	1,3	1,3
	%	1,2	8,8	0	3,2	1,3	4,1	3,1	3,1
					OSi-I				
	MCC	61,1	18,1	2122	2192	7,5	1242	941	1025
I	NACs	4,1	12	396	744	0,4	260	236	286
	%	6,7	66,3	18,7	34	5,3	21	25,3	23
					OSii-I				
	MCC	95,9	33,5	114	1,1	1357	5,5	268	499
	NACs	13,4	2,9	19,2	0	268	0,2	50,4	98,8
	%	14	8,7	16,8	0	19,7	3,6	10,5	8,1
					OSiii-I				
	MCC	3,21	1874	2207	85,4	1949	22,11	11442	1041
	NACs	80,2	619	1096	3,4	851	720	562	449
	%	25	33	49,7	4	43,7	32,6	31,3	18,8
					ORiii-II				
	MCC	0	0	0,1	0	0	0	0	0
	NACs	0	0	0	0	0	0	0	0
II	%	N/A	N/A	0	N/A	N/A	N/A	0	0
					OSiv-II				
	MCC	57,3	97	107,6	32,9	103	414	136	137
	NACs	0	2,4	0,3	0,4	0	14,1	2,9	5,2
	%	0	2,5	0,3	1,2	0	3,4	1,2	1,4

3.4 Conclusions

In this chapter, we present a detailed study of the effect of the change the initial velocity distributions assigned to the atoms during the QM/MM MD on the formation and evolution of Michaelis complexes (MCCs) and the conformations of close attack (NACs) in the acylation reaction of the (*R*,*S*)- propranolol catalyzed by CalB. Our results show that the populations of the MCCs and the NACs are dependent on sampling of the conformational space as a consequence of the change in the distribution of the initial vector velocities (Iseed number) used in the QM/MM MD. Despite this dependence, appreciable propensities were found: i) The MCCs between (*S*)-propranolol and CalB are more stable than MCCs with (*R*)-propranolol. The results can be interpreted as (*S*)- propranolol is favored at the start of the enantioselective step of the deacylation reaction of AceCalB. ii) The MCCs and the NACs present a longer lifetime when propranolol is oriented in the active site of CalB in binding mode I than in binding mode II. Our results suggest that the study of the free energy profiles during the deacylation reaction of AceCalB will be a useful approach, instead of the NACs approach, to complement the electronic energy reported (Escorcia et al., 2017).

Chapter 4. The tetrahedral intermediate-2 (TI-2) during the enantioselective acylation of (*R*,*S*)-propranolol catalyzed by *Candida antarctica* Lipase B

4.1 Introduction

The computational study of the enzyme deacylation step has been studied in the Grupo de Bioquímica Teórica, starting with the acetylated CalB (AceCalB). AceCalB, as well as the MCCs and TI-2, forward in the reaction, were studied using combined docking and MD simulations (Escorcia et al., 2013, 2014). Additionally, the study of the reaction barriers for the conversion of (*R*)- and (*S*)-propranolol to *O*-acetyl-propranolol were computed for several distinct conformations of TI-2 (Escorcia et al., 2017). The results showed that both (*R*)- and (*S*)-propranolol accommodate in two binding modes (namely, binding modes I and II). These binding modes differ in the orientation of the naphthoxy side chain of the propranolol orientation in the active site (Figure 6). The QM/MM molecular dynamics (QM/MM MD) of the reactive MCCs were performed. The analysis of the trajectories was focused on the interatomic distances important for the catalytic process and the temporal stability of the reactive MCCs, and to explore the ability of the propranolol enantiomers to form NACs (Chapter 3). The results showed that MCC and NAC populations depend on the random seed number for initial velocity assignment; nevertheless, MCC complex and NACs conformations lifetimes are higher in binding mode I than in binding mode II. The reaction barriers for the conversion of (*R*)- and (*S*)-propranolol to *O*-acetylpropranolol were calculated using at the DFT (B3LYP/TZVP)/CHARMM theory level and it was found that the activation energy for the transformation of (*R*)-propranolol to *O*-acetylpropranolol is 4,5 kcal/mol lower than that of the reaction of (*S*)-propranolol (Escorcia et al., 2017). These results gave us insights to rationalize the experimentally observed enantioselectivity in favor of (*R*)-propranolol (Figure 7). However, the crucial quantity to characterize enantioselectivity is the difference in the Gibbs free energy of activation in the enantioselective reaction steps (Overbeeke et al., 1998). To compare absolute energy barriers to absolute

free energy barriers, the QM regions used for calculations must be the same (Figure 18). In this chapter, we modeled the TI-2 behavior following a QM/MM MD protocol (SCCDFTB/CHARMM) previously reported (Escorcia et al., 2017). The principal difference is related to QM regions; in this chapter, the starting structures and the restart files of the MD to perform the free energy calculations (Chapter 5) were obtained. 8 TI-2 structures were selected to be used for free energy calculations; only four structures were quite comparable to the structures used for energetic barriers calculations (Escorcia et al., 2017).

4.2 Methods

The Quantum Mechanics (QM) region was created for 6 TI-2 conformations previously reported: ORI, ORII, ORIII, ORIV, OSI, OSII, OSIII, and OSIV (Appendix H: TI-2 conformations selected to QM/MM MD (SCC-DFT/CHARMM) theory level). All atoms of the (*R*, *S*)-TI-2 conformations and the side chains of the residues belonging to the catalytic triad: SEA105, D187 and H224 were considered as part of this region to be consistent with the QM region previously used for energetic barriers calculations (Escorcia et al., 2017). Technically, the QM region was described by four residues: one residue for the atoms that belong to SEA105 and the TI-2, another residue for the atoms of the side chain of D187, another residue for the atoms of the side chain of H224 and another residue for remaining atoms in the (*R*)- or (*S*)-propranolol (Figure 18). The rest of the atoms of CalB, crystal water molecules and the atoms of the solvent were part of the MM region. The residues of the catalytic triad were cut between the Cα-Cβ bond generating three QM/MM frontiers. The Cα of each residue of the catalytic triad was described with the Generalized Hybrid Orbital (GHO) approach (Gao et al., 1998). The QM region was described by the SCC-DFTB theory level (Cui et al., 2001; Seabra et al., 2007) and the MM region by the CHARMM22 force field (Brooks, B. R. and Brooks, III, C. L. and Mackerell, Jr. et al., 2009) in all cases. The minimizations and subsequent MD were performed following a protocol previously described (Escorcia et al., 2017). Briefly, all TI-2 configurations were minimized with the Steepest Descent and Adopted Basis Newton-Raphson -ABNR algorithms (Lewars, 2011) in an explicit solvent sphere. The solvent

molecules were arranged in a sphere centered on the Cα of SEA105 with a radius of 40 Å. Only a part of the protein could move freely, called the active region within a range of 30 Å. Amino acid residues outside this radius remained fixed during MD. The sphere of explicit solvent was restricted with a spherical border quartic potential starting with -0,25 kcal/mol to 39,5 Å, increasing to greater distances (parameters: FORCE = 0.25, P1 = 2.25 and DROFF = 38.5). The SHAKE algorithm was used to restrict all distances involving hydrogen atoms.

Figure 18

(R,S)-TI-2-propranolol and the QM regions considered in the calculations of the O-acylation reaction of (R, S)-propranolol catalyzed by CalB. ***A*** *Gray shadow represents the QM region used in the previously QM/MM MD reported for this reaction (Escorcia et al., 2017). This region covered the TI-2 and only one residue of the catalytic triad, SEA 105.* ***B*** *Blue shadow represents the QM region used for the calculations of the electronic energy profiles of this reaction (Escorcia et al., 2017) and the QM/MM MD needed for Umbrella Sampling in this chapter. A detailed explanation of the key interatomic distances in the stability of the TI-2 can be found in Figure 9.*

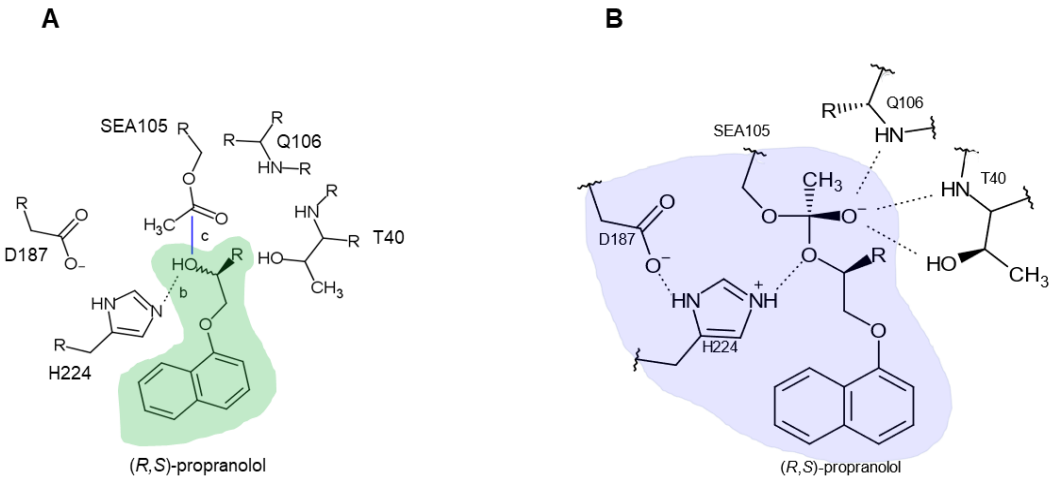

The electrostatic interactions between the particles were treated additive within a 14Å radius of the SEA105, and the electrostatic interactions at a larger radius were approximated by the multi-pole approach. A MD trajectory with the seed number 314159 was calculated. In the production phase, the

Verlet integration algorithm was used. The simulation time was 2ns, with a timestep of 1 fs. The analysis focused on the energy of the system and the geometry of the QM and MM region. All the visualization and analysis of the MD were carried out with the Visual Molecular Dynamics (VMD) program (Humphrey et al., 1996), and we select the TI-2 conformations comparable to those used in the energy barrier calculations previously reported (Escorcia et al., 2017).

4.3 Results and discussion

All the conformations of the TI-2 were stable during the MD trajectories (Appendix J: Time evolution of the key interatomic distances in the stability of the TI-2). The hydrogen bonds and covalent bonds at TI-2 show quite small changes throughout the trajectories. For example, the time evolution of the distances for TI-2-ORI conformations is shown (Figure 19).

Figure 19

*Time evolution of the key interatomic distances in the stability of the TI-2. **A**. Hydrogen bond D187···H224, **B**. Hydrogen bond H224···O39(propranolol), **C**. Hydrogen bonds carbonylic oxygen in SEA105 and amino acidic residues at oxyanionic hole: SEA105OM···Q106NH, SEA105OM···T40NH and SEA105OM···T40OM in black, red, and green diamonds. **D**. The covalent bonds of the TI-2 and the potential hydrogen bond between H224 and SEA105O (distances -d-, -g- and -h-) in black, red, and green diamonds. The detailed scheme of these distances can be found in Figure 9.*

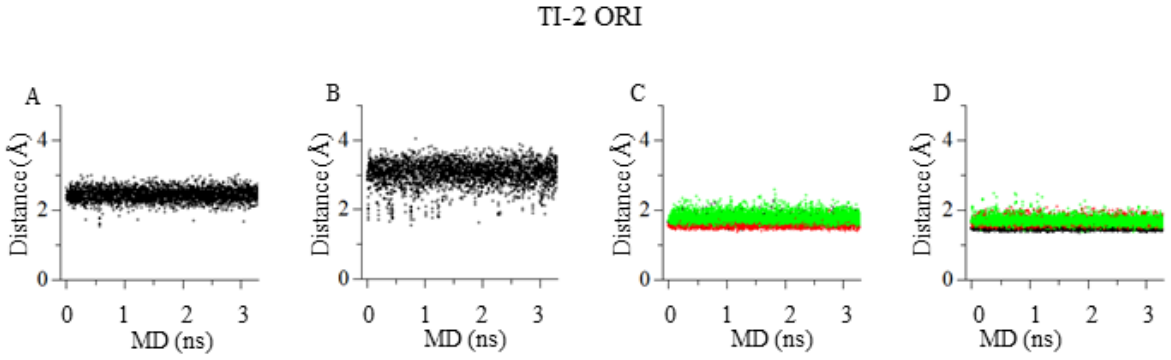

The time evolution of the distances (Figure 9) shows that in all cases, the hydrogen bonds were below 4Å, the hydrogen bonds at the oxyanionic hole were stronger than the hydrogen bonds formed by His 224, and the covalent bonds in TI-2 were below 2Å. This behavior does not depend on the enantiomer or

binding mode (Appendix J: Time evolution of the key interatomic distances in the stability of the TI-2). All the structures of the trajectory, one thousand, were aligned and superimposed to TI-2 starting structures used for the energetic barrier calculations. There were found four conformations quite similar to those previously reported in the calculations of the energetic barrier for the conversion of (*R*)- and (*S*)-propranolol to *O*-acetylpropranolol: ORI and OSI in binding mode I and ORIII and OSIII in binding mode II (Appendix H: TI-2 conformations selected to QM/MM MD (SCC-DFT/CHARMM) theory

Figure 20

Graphical representation of (R)- and (S)-TI-2 conformations selected for Umbrella Sampling exploration. The alpha helix surrounding the TI-2 are A5, A6 and A10 following the Uppenberg nomenclature(Uppenberg et al., 1995) (Figure 12). CalB backbone and TI-2 previously reported in blue(protein) and cyan (R-, or S- propranolol) colored representations. The selected conformations from QM/MM MD in this study are presented in green, orange, and gray colors.

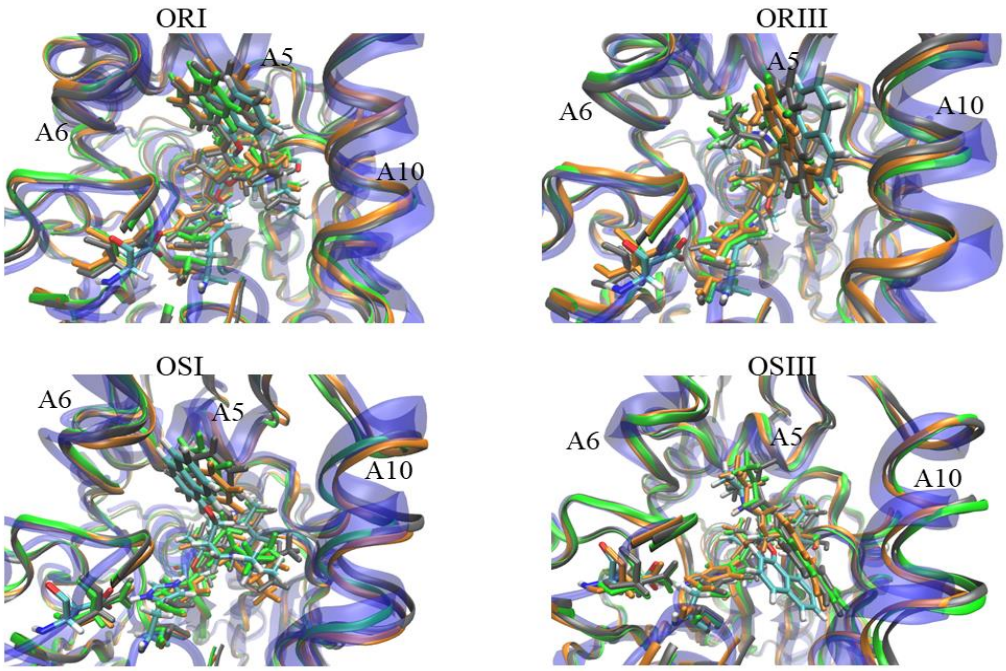

level). The four selected structures in our trajectories, and those previously reported (Escorcia, Sen, Daza, Doerr, & Thiel, 2017) did not show appreciable differences (Figure 20).

Two additional conformations were selected to improve the sampling of the free energy profiles. They had the almost the same RMSD values (variations less than 0,2Å) for all heavy atoms of the backbone of AceCalB. In all cases, the selected conformations were labeled with an additional lower case letter (-

a, -b or -c). “-a” means that the conformation is closer to MCC than EPC geometry, “-b” means that the conformation is between MCC and EPC geometries and “-c” means that the geometry is closer to EPC than MCC, see next chapter. Hence 12 TI-2 conformations were selected as starting structures to free energy calculations (Figure 20).

4.4. Conclusions

The TI-2 of the *O*-acylation of (*R,S*)-propranolol catalyzed by CalB was studied by using a QM/MM MD simulation protocol. The QM region was described by four residues: one for the atoms that belong to SEA105 and the TI-2, another the side chain of D187, another for the side chain of H224 and another for remaining atoms in the (*R*)- or (*S*)-propranolol. The total atoms in the QM region were 67. The critical net of hydrogen bonds and covalent bonds in this reaction were stable throughout all MD (1ns). Interestingly the hydrogen bonds at the oxyanionic hole were stronger than hydrogen bonds formed by H224 with D187, the (*R,S*)-propranolol, or SEA105. The effect of enlargement of the QM region does not affect the stability of the TI-2. The conformational space changed, and only 12 conformations in more than six thousand were comparable to those previously reported and used as starting conformations for electronic energy calculations (Escorcia, 2015).

Chapter 5. Free energy profiles during *O*-acylation of the (*R*,*S*)-propranolol catalyzed by *Candida antarctica* Lipase B

5.1 Introduction

In a previous investigation of this reaction using DFT (B3LYP/TZVP)/CHARMM it was found that the energy barrier of the transformation of (*R*)-propranolol to *O*-acetylpropranolol is 4,5 kcal/mol lower than that of the reaction of (*S*)-propranolol (Escorcia et al., 2017).

In this chapter, we extend our serial study of the CalB-catalyzed acetylation of (*R*,*S*)-propranolol to gain a deeper understanding of the molecular basis of the enantioselectivity and to gain insights of the role of the entropy in this reaction. We performed an exhaustive conformational sampling throughout the enantioselective step of the reaction (MCC→TI-2→EPC) following a QM/MM MD protocol (SCC-DFTB (Cui et al., 2001; Pu et al., 2004; Seabra et al., 2007) /CHARMM (Brooks, B. R. and Brooks, III, C. L. and Mackerell, Jr. et al., 2009)) in combination with the Umbrella sampling approach (Torrie & Valleau, 1977). From this sampling the free energy was obtained, applying the weighted analysis method of histograms (WHAM) approach (Roux, 1995; Souaille & Roux, 2001). These calculations help us to report the free energy profiles, analyze the finite-temperature effects, and determine the role of the entropy throughout the enantioselective step in the *O*-acylation of (*R*,*S*)-propranolol catalyzed by CalB.

5.2. Methods

5.2.1. Umbrella Sampling

The starting structures selected in Chapter 4 were used as the starting structures for *Umbrella sampling*. The conformational sampling throughout the enantioselective step of the reaction, MCC→TI-2→EPC was explored using the Umbrella sampling approach (Kottalam & Case, 1988).To this end, the

sampling was splitted into two reaction coordinates (RCs), as previously was reported for energetic calculations (Escorcia et al., 2017), one from TI-2 to MCC and one from TI-2 to EPC (Figure 21). The sampling along the RCs was divided into sampling windows every 0,125Å. A sampling range of ± 0,5Å was used in each window. All windows were divided every 0,001Å, and each of these sections was called bin (Kottalam & Case, 1988).

Figure 21

Reaction coordinates (ξ_1 and ξ_2) used in the QM/MM calculations: ξ_1 (left) = ((-b-) - (-a-)). ξ_2 (right) = ((-c-) - (-d-). ξ_1 and ξ_2 lead from TI-2 to the corresponding MCC and EPC, respectively. Dotted lines show hydrogen bonds and r -b- and r -c- show covalent bonds.

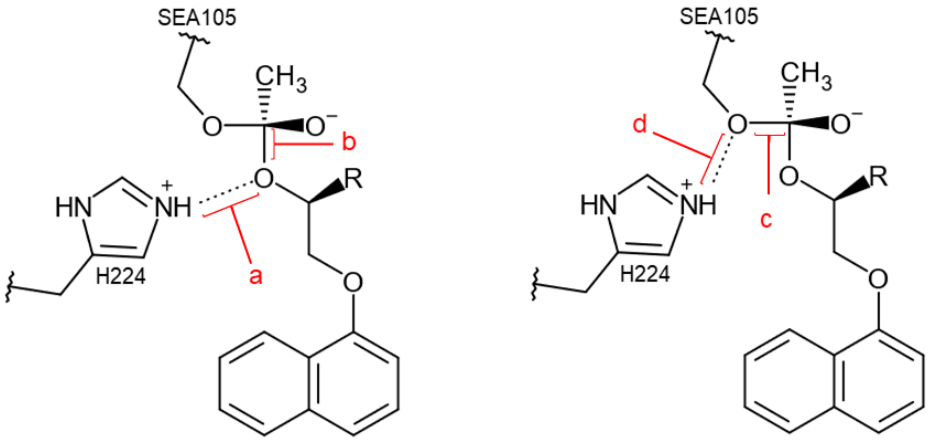

To ensure an exhaustive conformational sampling, the MD was combined with the Umbrella potential and a second bias potential (U_{bias}). The form and parameters for Umbrella potential was:

$$\text{Umbrella potential} = k_u(\text{delta} - \text{delta0})^2 + U_{bias}(\text{delta}) \text{ where:}$$

k_u: is the harmonic restraining potential constant

delta: is the reaction coordinate value for a particular conformation sampled

delta0: is the reaction coordinate value used for centering the window sampling

U_{bias}: is the biasing potential, used in addition to the harmonic restraining potential.

U_{bias} has been implemented in CHARMM as a cubic spline function based on previously tabulated data (Brooks, B. R. and Brooks, III, C. L. and Mackerell, Jr. et al., 2009). In each step of the QM/MM

MD, the value of the RC was evaluated, and the conformation was located in the corresponding bin. Initially, QM/MM MD was performed with sampling times of 6ps was done sequentially: the coordinate (.crd) and restart (.rst) files printed at the end of the sampling window *i* were used to carry out the sampling in the sampling window *i* + 1. Later, the number of conformations found were graphed as histograms. The free energy profile (potential of mean force) was calculated, see below. The U_{bias} was modified manually in each window, ensuring the conformational sampling throughout the RC. The harmonic restraining potential (k_u) was 40 kcal / (mol Å^2).

Additionally, three points were sampled in the opposite direction to the RC to evaluate if the initial structure of TI-2 corresponded to a minimum on the free energy surface. Then, the sampling time was increased to 15ps per window sampling: The coordinate (.crd) and restart (.rst) files printed at the end of the QM/MM MD in the 6ps sampling were used to perform the calculation at 15ps in each window. Then, all the trajectories were calculated in parallel. Once the histograms of the conformational sampling presented a Gaussian behavior centered in each step of the RC, the sampling time was increased, in each window, to 30ps and later to 60ps. Two additional k_u values (30 and 50 kcal /(mol Å^2)) were tested to avoid results dependent on $k_{u,}$. All visualization and trajectory analysis of the MD was made with the VMD program (Humphrey et al., 1996).

The reaction coordinates have a common atom: H224NH for interatomic distances -a- and -d- in ξ_1 and ξ_2 (Figure 21 and Appendix I: Key interatomic distances in the stability of the TI-2), this implies that for a given RC value the geometry can be closer to the MCC than to the EPC, vise versa, or to be found in the middle of these geometries. For this reason, the selected conformations were labeled with an additional: "-a" if the RC is closer to MCC than EPC, "-b" if the RC is right in the middle between MCC and EPC, and "-c" if the RC is closer to EPC than MCC. When no additional letter appears in the nomenclature of the conformation of the TI-2, it means that this geometry was quite similar to the used in the calculations of electronic energy (Escorcia, 2015; Escorcia, Sen, Daza, Doerr, & Thiel, 2017). The three conformations selected for the ORI-TI-2 are shown as an example (Figure 22).

Figure 22

Classification of the conformations of the TI-2 according to their proximity to the geometries of the MCC or the EPC. The relative position of the H224HE1 (involucrated in the ξ1 and ξ2 definition, (Figure 21) was used to classify the conformations of TI-2: A. Conformation close to MMC geometry, B. Conformation in the middle between MCC and EPC geometries and C. Conformation close to EPC geometry. The conformations were labeled as: ORIII-a, ORIII-b, and ORIII-c.

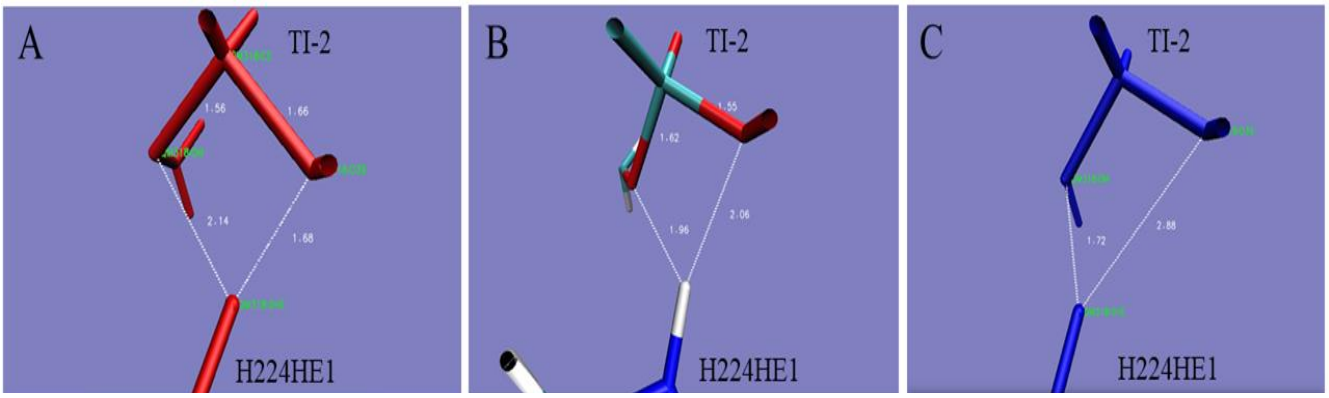

5.2.2. Free energy calculation and conformational analysis

The free energy profiles (Mean Force Potential) between the tetrahedral intermediate and the Enzyme-Substrate and Enzyme-Product complexes were obtained using the weighted analysis of histograms (WHAM) approach (Roux, 1995; Souaille & Roux, 2001). The convergence criterion for the free energy constants was 0,01 kcal/mol. The PMFs calculated with sampling times of 30ps and 60ps were adjusted to a polynomial function of grade 9. The PMF between the minimum free energy of the TI-2 in the reaction coordinates ξ_1 and ξ_2 was calculated to build the complete PMF (MCC→ TI-2→EPC).

All trajectories were merged and analyzed the root mean square deviation (RMSD), between starting TI-2 structure and all structures in trajectory, for the heavy atoms of the AceCalB backbone, and secondary structures surrounding the active site: i) Amino acid residues L136 to T159 of the alpha helix 5, loop and alpha helix 6. ii) Amino acid residues A185 to V194. iii) The segment of the alpha-helix 10, com-

posed of the amino acid residues L278 to V286 and of the (*R*)- or (*S*)-TI-2-propranolol (Barrera Valderrama et al., 2018). The evolution of key hydrogen bonds in the catalytic mechanism, see Figure 1, was compared in all computed free energy profiles.

5.2.3. Finite-temperature effects

To investigate the importance of finite-temperature effects (f.t.e.), we compared the PMF and the potential energy surface (PES) along the reaction coordinate following the approach previously reported (Senn et al., 2009). Several conformations were selected for the calculation of the PES; to this end, all conformations of the TI-2 found at the center of the free energy minimum +/- 0,05 Å in ξ_1 and ξ_2 were analyzed using the cluster a plugin in VMD (Humphrey et al., 1996). The parameters used for clustering were: Number of clusters = 5 and the RMSD for all heavy atoms in the QM region = 0.6, then one snapshot aleatory selected from each one cluster was used to perform the potential energy scan (PES) using the semiempirical methods SCC-DFTB(Cui et al., 2001; Pu et al., 2004; Seabra et al., 2007) for QM region and the CHARMM force field for MM region. One randomly selected snapshot was used as a starting point for the potential energy scan using the semiempirical method SCC-DFTB (Cui et al., 2001; Pu et al., 2004; Seabra et al., 2007) for the QM region and the CHARMM force field for MM region. These optimized structures were used as starting points in PES along the RCs ξ_1 and ξ_2 in steps of 0,125Å. At each step of these scans the reaction coordinate was constrained, and the rest of the active region was relaxed. All PES calculations were performed in Chemshell software (Metz et al., 2014) coupled to MNDO99 software(Thiel, 2007). QM/MM geometry optimization was carried out employing the hybrid delocalized internal coordinates (HDLC) optimizer (Billeter et al., 2000). Only the smooth and comparable PES, were compared to the corresponding PMF and hence analyzed, roughly, the finite temperature effects. The PES of TI-2 conformations selected from the TI-2 minimum in ξ_2 were used only to verify that MCC and EPC could be achieved from these conformations.

5.3 Results and discussion

5.3.1. Umbrella sampling

The conformational space along the RCs ξ_1 and ξ_2 in the 12 selected conformations were initially explored using the Umbrella sampling approach with a sampling time of 6ps per window. Only 66% of the conformations successfully evolved towards MCC and EPC from TI-2.These conformations were 4 for (*R*)-TI-2-propranolol and 4 for (*S*)-TI-2-propranolol. The (*R*)-TI-2-propranolol the binding mode I was favored over binding mode II, for the (*S*)-TI-2-propranolol, just the opposite, the binding mode II was favored over binding mode I (Table 3, column 1). The remaining 34% of the conformations only evolved towards MCC or EPC. These results show a strong propensity: the evolution from (*R*)-TI-2-propranolol to MCC and EPC is, in binding mode I, easier than in binding mode II. The evolution from (*S*)-TI-2-propranolol to MCC and EPC is, in binding mode II, easier than in binding mode I, see free energy discussion below.

The sudden increase in energy because of steric clash in some conformations means that the convergence criteria are not met. These results disclose that convergence problems evidenced during QM/MM MD are tightly related to the binding mode and the enantiomer. This assumption is supported by the asymmetric surface inside of binding pockets in CalB (Figure 6). The distances used for defining the RCs in the starting structures which connect TI-2 with MCC and EPC after umbrella sampling are shown in Table 4. The values of the RC ξ_1 (TI-2 to MCC) ranged from -0,02 to -0,82 in the (*R*)-TI-2-propranolol conformations and between -0,13 to -1,14 in the (*S*)-TI-2-propranolol conformations. The value of the ξ_2 (TI-2 to EPC) ranged from -0,25 and -1,53 in the (*R*)-TI-2-propranolol conformations and from -0,25 to -0,83 in the (*S*)-TI-2-propranolol conformations, see Table ***1***, columns 6 and 7.

Table 3

Root mean square deviation (RMSD) between TI-2 selected conformations for the heavy atoms of the AceCalB backbone, and secondary structures surrounding the active site: i) Residues amino acids L136 to T159, of the alpha helix 5, loop and alpha helix 6. ii) Loop composed of amino acid residues A185 to V194. iii) Segment of the alpha helix 10, composed of the amino acid residues L278 to V286 and iv) of the (R)- or (S)-TI-2-propranolol, for a graphic localization of these secondary structures. The reference structure was ORI for conformations in binding mode I and ORIII-a for conformations in binding mode II.

		RMSD[a] values			
Conformation[#]	AceCalB	i	ii	iii	iv
Binding Mode I					
ORI[*]	na,	na,	na,	na,	na,
ORI-b	0,82	1,18	0,83	2,0	3,69
ORI-c	0,61	0,71	0,48	0,57	1,01
OSI-a	0,74	1,11	0,48	0,77	1,68
Biding Mode II					
ORIII-a[*]	na,	na,	na,	na,	na,
OSIII	0,82	1,18	0,83	2,0	3,69
OSIII-b	0,82	0,74	0,57	2,41	3,70
OSIII-c	0,80	0,77	0,55	2,36	3,45

[a] Calculated using the plugin RMSD tool in VMD. [#]Conformation successfully evolved towards MCC and EPC from TI-2
[*]Conformation used as reference for RMSD calculations.

The differences in ξ_1 or ξ_2 values are mainly due to the variation in the distances of the hydrogen bond between catalytic protonated His224 and the oxygen atom from hydroxyl group at (*R,S*)-propranolol, or the oxygen atom from serine side chain in SEA105, respectively, see distances -a- and -d- (Figure 9).

The H224 is localized at the beginning of alpha helix 9 (Uppenberg et al., 1994, 1995) and it is surrounded by amino acidic side chains from highly flexible secondary structures, including the catalytic D187, that are responsible for the fluctuations in the hydrogen bonds used for RC definitions. The conformations showed in Table ***1*** were used to explore the conformational space using sampling times of 15, 30, and 60ps per window. Although the sampling time of 6ps or 15ps does not provide smooth and continuous PMFs, it allowed to make the necessary manual modifications in the U_{bias} potential to obtain samplings with Gaussian behavior at longer sampling times, 30 or 60ps/window. 60ps/window is three times higher than reported for the study of Diels-Alder reaction in CalB(Świderek & Moliner, 2015).

Table 4

Reaction coordinate values in (R) or (S)-TI-2-propranolol starting conformations.

Conformation[&]	Interatomic distance value (Å)[*]				R,C,[**] value (Å)[*]	
	-a-	-b-	-c-	-d-	ξ_1	ξ_2
Binding mode I						
ORI	1,85	1,65	1,53	2,27	-0,03	-1,53
ORI-b	2,07	1,57	1,51	2,05	-0,5	-0,54
ORI-c	2,32	1,50	1,58	1,83	-0,82	-0,25
OSI-a	1,78	1,55	1,57	2,36	-0,23	-0,79
Binding mode II						
ORIII-a	1,68	1,66	1,56	2,14	-0,02	-0,58
OSIII	2,69	1,55	1,58	1,79	-1,14	-0,65
OSIII-a	1,77	1,64	1,61	2,44	-0,13	-0,83
OSIII-b	1,91	1,62	1,65	1,90	-0,29	-0,25

[&] There are listed only the conformations that successfully evolved to MCC and EPC.

[*] Distances -a- and -b- are used for ξ1 definition. Distances -c- and -d- are used for ξ1 definition (Figure 21).

[**] ξ_1 ξ_2 lead from TI-2 to the corresponding Michaelis complexes and enzyme-product complexes, respectively.

The higher the value in the harmonic restraining potential constant (k_u), the higher is the sampling histograms. In almost all cases, more than 4000 conformations were found in the central bin of each sampled window; this number is nearly seven times higher than reported in recent studies focused on prediction on the enantioselectivity in *Candida rugosa* and *Burkholderia cepacia* lipases (Mathpati & Bhanage, 2018). Besides, histogram overlapping was present (Figure 23 and Figure 24). The initial value of the RC determines the number of windows to be sampled: If the TI-2 geometry is closer to the EPC than the MCC, fewer windows will be needed to find the EPC or MCC, respectively. The number of sampled windows ranged from 21 to 38 from TI-2 to MCC or EPC. The total time sampled ranged from 2,16ns to 2,28ns (Table 5).

Figure 23

Effect of the harmonic restraining potential constant ku effect in Umbrella sampling for ORIII-a conformation. On the top sampling in reaction coordinate ξ1. On the bottom in reaction coordinate ξ2. ku is raising from left to right: 30 , 40 and 50 (kcal/molÅ^2).

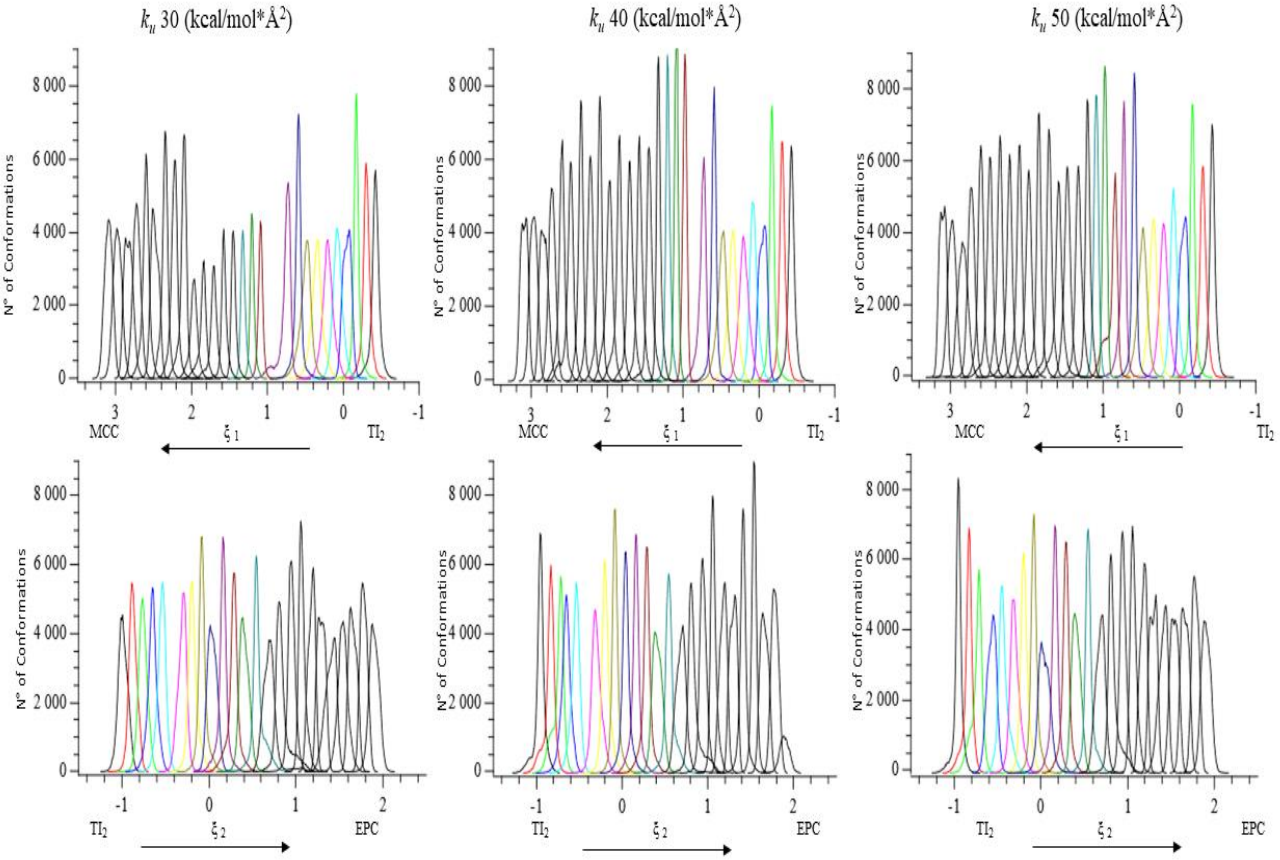

Figure 24

Effect of the harmonic restraining potential constant k_u effect in Umbrella sampling for OSIII conformation. On the top sampling in reaction coordinate ξ1. On the bottom in reaction coordinate ξ2. ku is raising from left to right: 30 , 40 and 50 (kcal/molÅ²).

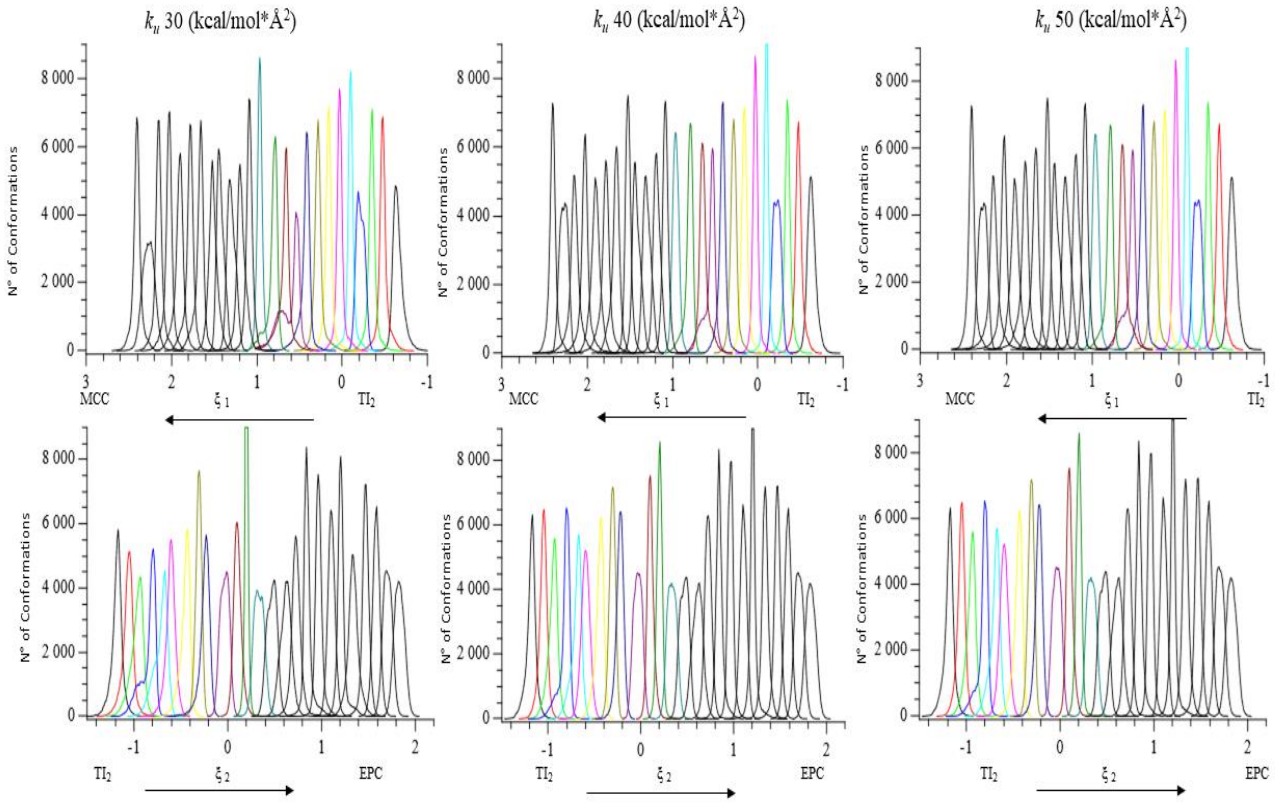

5.3.2. Free energy profiles

The PMF calculated with a time sampling of 30 or 60ps/window have the same shape, even when different harmonic restraining potential constants (k_u) were used. As an example, the PMFs calculated from ξ_1 for the conformation ORIII-a Appendix K: Harmonic restraining constant (*ku*) effect in the PMF for ORIII-a conformation). The adjustment of the PMFs with a polynomial function of grade 9 allows appreciate that the conformation ORIII-a and its MCC corresponds clearly to a minimum and indicates the quality of sampling along the reaction coordinate.

Table 5

Number of windows and total time sampled with umbrella sampling approach.

Umbrella Sampling (60 ps)				
Conformation[&]	N° of Windows -ξ_1[*]-	Sampled time (ns)	N° of Windows -ξ_2[**]-	Sampled time (ns)
Binding Mode I				
OR-I	35	2,1	38	2,28
ORI-b	34	2,04	36	1,26
ORI-c	29	1,74	21	2,16
OSI-a	29	1,74	23	1,38
Binding mode II				
ORIII-a	24	1,44	25	1,5
OSIII	28	1,68	23	1,38
OSIII-a	26	1,74	38	2,28
OSIII-b	31	1,86	21	1,26

[&] There are listed only the conformations that successfully evolved to MCC and EPC.
[*] Reaction coordinate from TI-2 → MCC. [**]Reaction coordinate from TI-2 → EPC.

The free energy barrier to TI-2 formation is ~ 17 kcal/mol using k_u = 40 (kcal/mol*Å^2). In all cases, the PMFs found are not dependent on time sampling after 30ps by window. The k_u effect on PMF can be summarized as the higher value in k_u the higher the absolute value in the PMF, not exceeding 3kcal/mol, except for the conformation OSI-a in ξ_2 where the absolute free energy value was near to 5kcal/mol and EPC were exergonic (Figure 25). Henceforth, we will be focused on discussion of the PMFs calculated using k_u = 40 (kcal/mol*A^2) and sampling time = 60ps/w.

To analyze the free energy throughout the *O*-acylation of (*R*,*S*)-propranolol catalyzed by CalB is necessary to merge the PMF found in ξ_1 or ξ_2 in all selected TI-2 conformations which successfully reached the MCC and the EPC. To this end, the PMF to convert the TI-2 from ξ_1 to the TI-2 in ξ_2 was calculated. The merged PMFs shows the complexity of the free energy landscape in this reaction.

The free energy profile throughout the reaction was calculated for 8 TI-2 conformations. The PMFs from conformations ORI, ORI-b, ORI-c, OSIII, OSIII-a, and OSIII-b had similar shapes and can be considered as plausible reactions paths, see Figure 25. The remaining PMFs from conformations ORIII-a and OSI-a were highly endergonic with 6,4 and 18,2 kcal/mol, respectively (Appendix L: QM (SCC-

DFTB)/MM highly endergonic potential mean force (PMF) for the conversion of (*R,S*)-propranolol to *O-acetylpropranolol* in binding modes I and II).

Figure 25

Effect of the harmonic restraining potential constant on potential mean force PMF. The ku effect on PMF can be summarized as the higher value in k_u the higher the absolute value in the PMF, not exceeding 3kcal/mol, except for the conformation OSI-a in ξ_2 where the absolute free energy value was near to 5kcal/mol, and the EPC were endergonic.

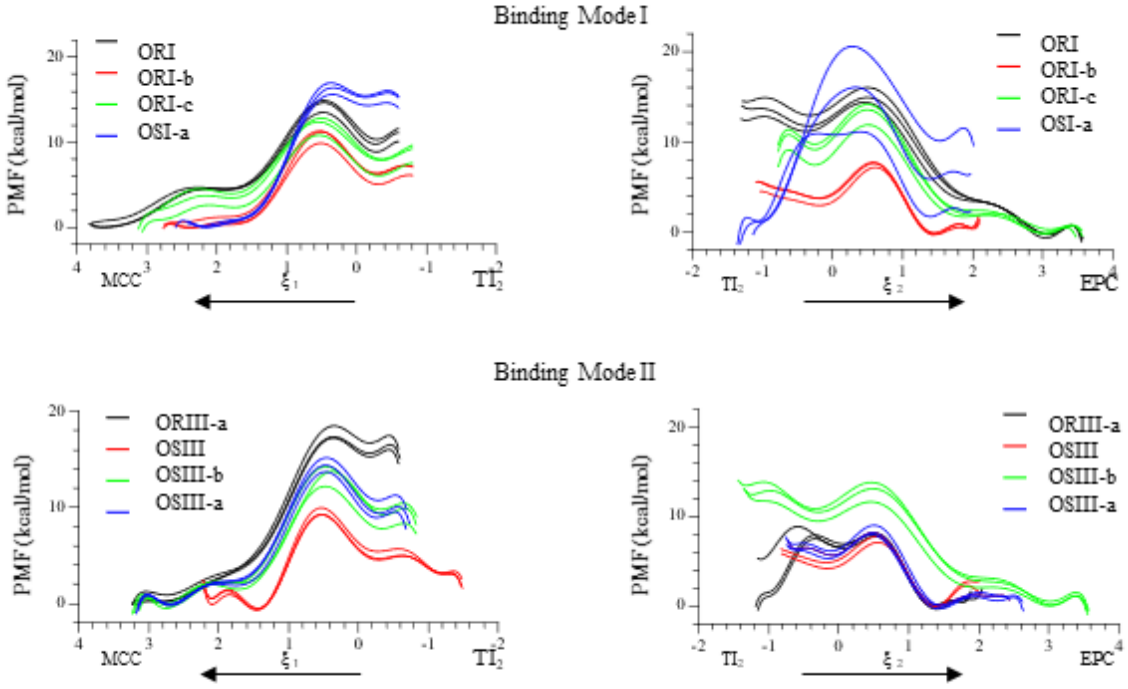

All TI-2 minimum in both ξ_1 and ξ_2 reaction coordinates showed high overlapping, and the PMF value was similar (Figure 22), in no-highly endergonic reaction paths. In highly endergonic reaction paths, the overlapping of RCs was small and had a free energy gap of 1,4 and 4 kcal/mol in conformation ORIII-a and OSI-a (Appendix L: QM (SCC-DFTB)/MM highly endergonic potential mean force (PMF) for the conversion of (*R,S*)-propranolol to *O-acetylpropranolol* in binding modes I and II). The TI-2 is localized between two free energy barriers evidencing that it is not a transition state analog in the CalB-catalyzed *O*-acetylation of (*R,S*)-propranolol in toluene (since $\Delta PMF_{(TI\text{-}2\text{-}Barrier\ 1)}$ is ~-4,5 kcal/mol and $\Delta PMF_{(TI\text{-}2\text{-}Barrier\ 2)}$ is ranged between -2,8 and -4,6 kcal/mol), see columns B1, TI-2 and B2 (Figure 26).

This result is comparable and supports our previous findings: the TI-2 is 6 kcal/mol below transition state 1(Escorcia et al., 2017). Additionally, the TI-2 formation from the MCC is the enantioselective step in the reaction, see columns B1, and B2 (Figure 26), as was previously found in QM (B3LYP/TZVP)/MM energy profiles for thermodynamically favored reaction paths for the conversion of (*R*)- and (*S*)-propranolol to *O*-acetylpropranolol. (Escorcia et al., 2017)

Figure 26

*QM(SCC-DFTB)/MM potential mean force (PMF) for the conversion of (R, S)-propranolol to O-acetylpropranolol in binding modes I and II. ORI, ORI-b, and ORI-c are different conformations in Binding mode I and OSIII, OSIII-a, and OSIII-b are different conformations in Binding mode II. PMF values are relative to Michaelis complex values. * Reaction coordinate after merge RCs ξ_1 and ξ_2, see methodology section. The symbols were graphed by skipping six points in all curves. Table at the left shows the relative PMF value at free energy barrier 1 (B1), Tetrahedral intermediate (TI-2), free energy barrier 2 (B2), and enzyme-product complex (EPC).*

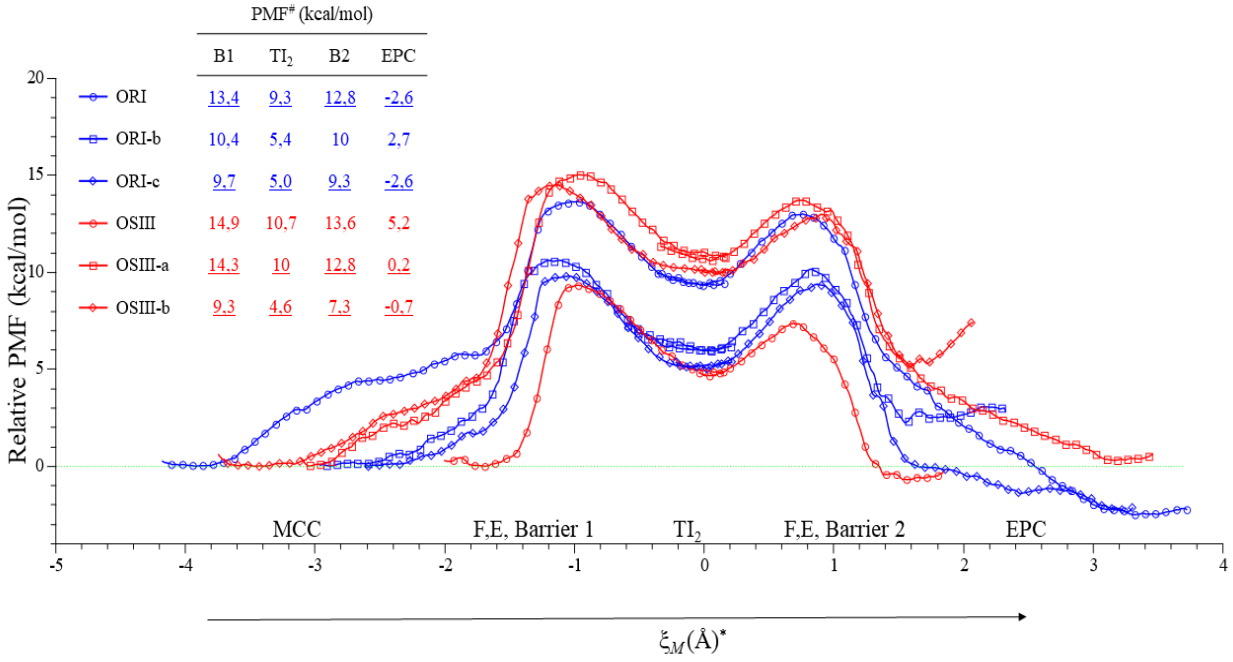

The formation of TI-2 from the MCCs for the (*R,S*)-propranolol indicates that (*R*)-propranolol is favored over (S)-propranolol regardless of starting conformation in binding mode I. The values of the free energy barrier range from 7 to 14 kcal/mol for (*R*) -propranolol and from 15 to 17 kcal/mol for (*S*)-propranolol. The free energy value of EPCs indicates that (*R*)-acetylated-propranolol are more exergonic

than (*S*)-acetylated-propranolol (Figure 26 -column EPC-). The values of the free energy barrier range from 9,7 to 13,4 kcal/mol for (*R*)-propranolol and between 9,3 to 14,9 kcal/mol for (*S*)-propranolol (Figure 26 -column B1). Free energy profiles of (*R*)-propranolol in binding mode II and (*S*)-propranolol in binding mode I are highly endergonic (Appendix L: QM (SCC-DFTB)/MM highly endergonic potential mean force (PMF) for the conversion of (*R,S*)-propranolol to *O-acetylpropranolol* in binding modes I and II. In binding mode I for (*R*)-propranolol and in binding mode II for (*S*)-propranolol, the formation of TI-2 and EPC is the reaction rate-determining step confirming the results previously obtained for the energy barrier (Escorcia et al., 2017). The quantitative analysis of PMFs shows that the free energy barrier for exergonic reaction paths are 9,7 and 13,4 kcal/mol for ORI-c and ORI TI-2 conformations and 9,3 and 14,3 kcal/mol for OSIII-b and OSIII-a TI-2 conformations. The $\Delta PMF_{(ORI\text{-}c\ -\ OSIII\text{-}b)}$ does not show appreciable enantioselective difference between this two reaction paths, the $\Delta PMF_{(ORI\text{-}c\ -\ OSIII\text{-}a)}$ is -4,6 kcal/mol, the $\Delta PMF_{(ORI\ -\ OSIII\text{-}b)}$ is 4,1 kcal/mol, and $\Delta PMF_{(ORI\ -\ OSIII\text{-}a)}$ is 0,9 kcal/mol, the average $\Delta PMF_{(ORI\text{-}c + ORI) - (OSIII\text{-}b + OSIII\text{-}a)}$ is -0,25kcal/mol. Even though these results cannot reproduce the experimental enantioselectivity, they are qualitatively comparable to QM (B3LYP-TZVP)/MM results (Escorcia et al., 2017). The underestimation of the enantioselectivity is associated to the SCC-DFTB precision method. (Cui et al., 2001).

5.3.2.1. Conformational analysis in the free energy surface. The conformational space of TI-2 minimum has hundreds of conformations (Figure 27), in the free energy surface in both RC, and it is as long as ~0,4Å (Figure 28). The cluster analysis helped to avoid artifacts due to the choice of conformation selection in the MD trajectories. The RMSD of 0,6Å value for all heavy atoms in the QM region was selected as a threshold to construct 5 clusters to elucidate the representative structures of TI-2; see the methodology section. The number of conformations of TI-2 in each cluster using the RMSD = 0.6 as threshold is shown as histograms (Figure 29).

One snapshot from each one cluster was selected and used as starting conformations in potential energy explorations using the semiempirical method SCC-DFTB; see methodology section. The hydrogen

bonds between the carbonylic oxygen of SEA105 side chain and the oxyanionic hole: Q106NH···EA105OE, T40NH···SEA105OE, and T40OH···SEA105OE, see distances -d-, -e-, and -f- dotted lines (Figure 9) have a different behavior when the reaction coordinates are explored. This result confirms our previous assumptions (Escorcia et al., 2014, 2017). As the MCC evolve to TI-2, monitoring by ξ_1, the distance all of the three hydrogen bonds being shorter by ~ 0,5Å than in MCC except when the sampling was performed in the EPC direction in the conformations ORI-c, OSI-a, and OSIII.

Figure 27

Conformational space of (R,S)-TI-2-propranolol. Top: ORIII-a conformational space: Top left, the formation of (R)-TI-2-propranolol from MCC. Top right, formation of EPC from TI. Bottom section. OSIII-b conformational space: Top left, the formation of (S)-TI-propranolol from MCC. Top right, formation of EPC from TI. Conformations sampled every 100 frames are represented by lines. Trajectories were colored from starting windows -from umbrella sampling- (white color), intermediates windows (blue color), and final windows (red color). The starting structure in all cases is represented by the licorice drawing method.

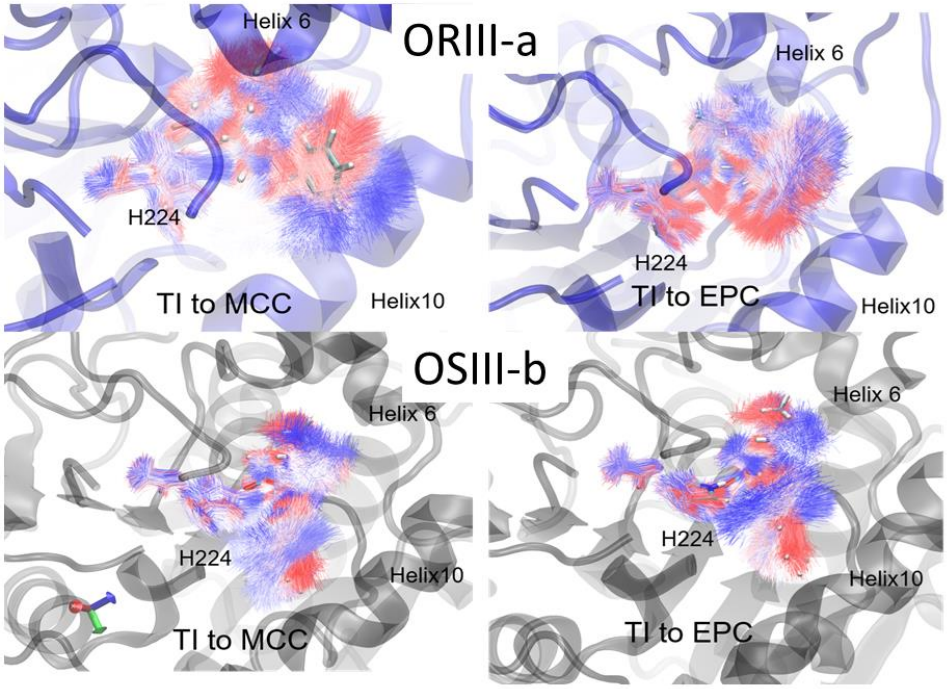

The TI-2 representative snapshots selected from the structural cluster analysis (Figure 28) were similar in all cases, as an example, the superposition of the all heavy atoms in catalytic residues Asp187, His224

and a portion of the TI-2 in the conformations ORI, OSI-a, ORIII-a and OSIII Figure 29). In all cases, the difference in the RC ξ1 was less than 0,1Å.

Figure 28

The number of conformations of TI-2 in each one cluster using the RMSD 0,6Å as threshold is showed as histograms. Black histograms correspond to TI-2 minimum conformation in the reaction coordinate that explores the TI-2 formation from MCC (ξ_1), and the red histograms correspond to TI-2 conformations in the reaction coordinate that explore the EPC formation from TI-2 (ξ_2), see methodology section above. In the cluster 6, all residual conformations were collected.

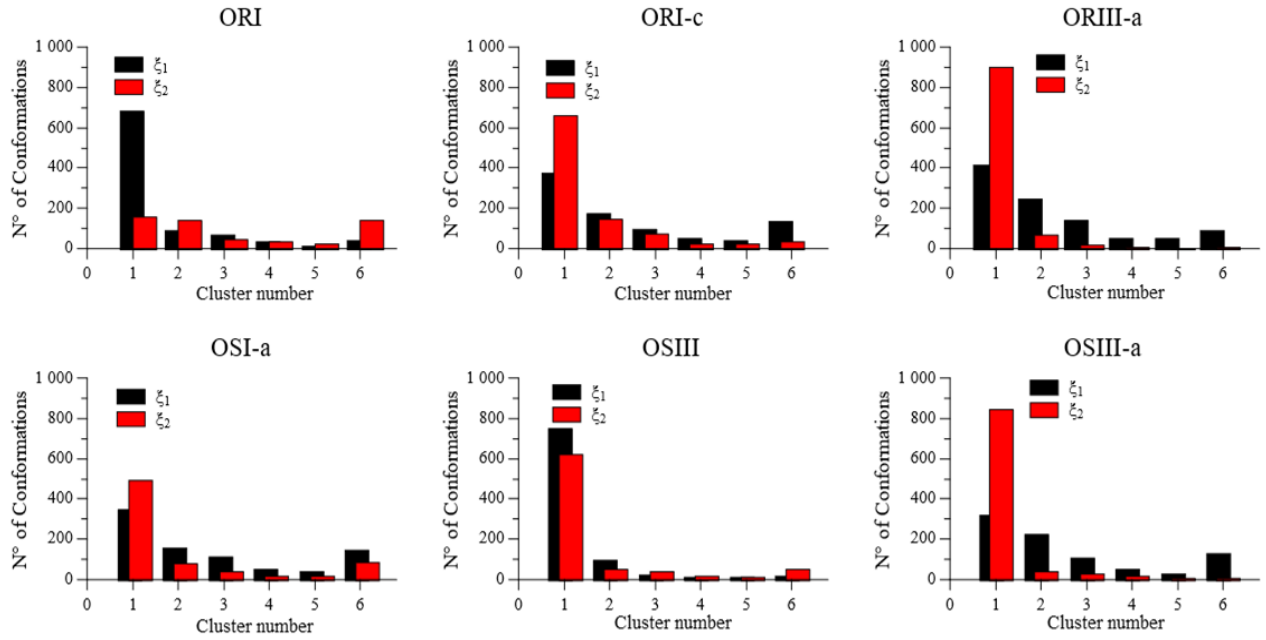

In all representative snapshots, the RMSD for the backbone of the protein, the secondary structures surrounding the active site, and the QM region were smaller than 0,61Å, 0,89Å, and 1,2Å, respectively, using as reference structure the conformation ORI for conformations in binding mode I and the conformation ORII-a for conformation for conformations in binding mode II. Interestingly, the backbone of the alpha helix 10 corresponding to residues L278 to V286 shows a higher mobility in binding mode II than in binding mode I, especially for the conformations of the (*S*)-propranolol. The principal differences in the QM region are related to small changes in the relative position of the naphtoxy group or the isopropylamine chain of the propranolol in the active site.

Figure 29

Superposition of the representative snapshots of TI-2 minimum in (R)- and (S)-propranolol, detail of the catalytic Asp187, and His224 residues. The superposed structures were selected after structural cluster analysis (Figure 28). The RMSD value was smaller than 0,61Å and 1,2Å for the protein backbone or QM region, respectively.

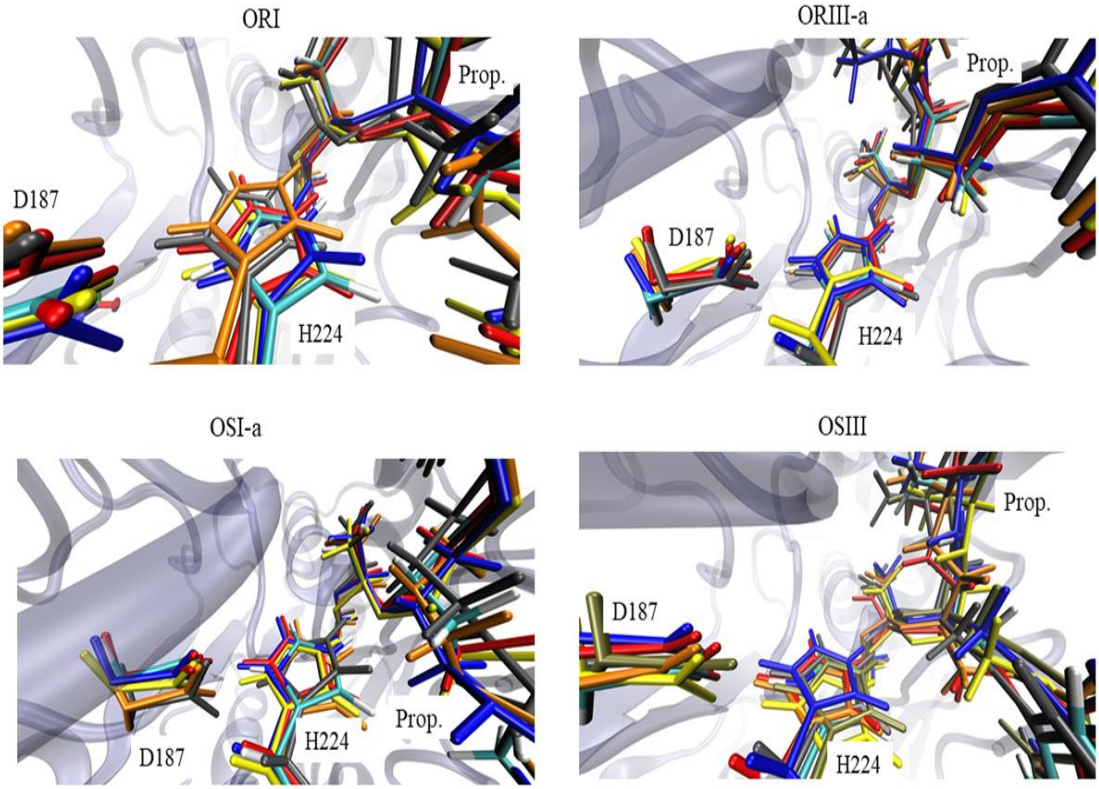

Notwithstanding this high similarity, it was decided to elucidate the influence of the small structural variation of the TI-2 on the energetic barriers in the QM (SCC-DFTB)/CHARMM calculations, see potential energy surface section below.

The conformational analysis throughout the PMF shows that there are several differences between the secondary structures surrounding the active site when the substrate is in binding mode I or binding mode II. In binding mode I the alpha helix 10 backbone shows more mobility than the other backbone surrounding the active site. The RMSD in AceCalB was ~ 1,8 times lower than in the substrate using as reference structure the starting structure of the MD. In binding mode II the alpha helix 10 backbone shows more mobility than the other backbone surrounding the active site. Only in AceCalB and alpha

helix 10 backbone the RMSD value in ξ_1 than in ξ_2. The mobility in AceCalB was ~ 2,1 times lower than in the substrate. The configurational space of the TI-2 was analyzed in six conformations: ORI, ORI-c, and OSI-a in binding mode I and ORIII-a, OSIII, and OSIII-a in binding mode II. The behavior of the RMSD in AceCalB or substrate in deacylation step evidence that the induced-fit between the CalB and (*R,S*)-propranolol is mutual at several points along the reaction coordinate but the substrate rearrangement is higher when the TI-2 is transformed to EPC in binding mode II than in Binding mode I (Figure 30), and the *average* rows in Table 6. This last result is particularly interesting because, in C-H → C hydride-transfer catalyzed by dihydrofolate reductase or the reductive methylation catalyzed by thymidylate synthase, the induced-fit occurs just at the beginning of the reaction (Kohen, 2015).

Table 6

Average root mean square deviation (RMSD) during the enantioselective step of the O-acylation of (R,S)-propranolol catalyzed by CalB for all heavy atoms of the AceCalB backbone, the secondary structures surrounding the active site: i) Residues amino acids L136 to T159, of the helix alpha 5, loop and helix alpha 6. ii) Loop composed of amino acid residues A185 to V194. iii) Segment of the alpha 10 helix composed of the amino acid residues L278 to V286 and of the (R)- or (S)-propranolol.

	RMSD[a] average values				
Conformation[&]	Acetyl-CalB	L136 toT159	A185 toV194	L278 to V286	(*R,S*)-TI-2-propranolol[*]
	ξ_1/ξ_2	ξ_1/ξ_2	ξ_1/ξ_2	ξ_1/ξ_2	ξ_1/ξ_2
Binding Mode I					
ORI[†]	0,56 / 0,60	0,65 / 0,64	0,57 / 0,56	0,56 / 0,68	1,26 / 1,83
ORI-b[††]	0,57 / 0,57	0,64 / 0,6	0,60 / 0,55	0,66 / 0,71	0,96 / 0,95
ORI-c [†]	0,61 / 0,61	0,56 / 0,73	0,58 / 0,55	0,67 / 0,59	1,28 / 1,66
OSI-a[††]	0,55 / 0,60	0,59 / 0,73	0,55 / 0,52	0,75 / 0,69	1,14 / 0,92
Average (SD)	*0,57 / 0,60*	*0,61 / 0,68*	*0,58 / 0,55*	*0,66 / 0,67*	*1,16 / 1,34*
	(0,03) / (0,02)	*(0,04) / (0,07)*	*(0,02) / (0,02)*	*(0,08) / (0,05)*	*(0,15) / (0,47)*
Binding mode II					
ORIII-a[††]	0,58 / 0,57	0,62 / 0,61	0,54 / 0,52	0,79 / 0,72	1,82 / 1,35
OSIII[††]	0,65 / 0,64	0,65 / 0,65	0,62 / 0,57	0,74 / 0,95	1,71 / 1,30
OSIII-a[†]	0,64 / 0,58	0,83 / 0,61	0,61 / 0,59	0,88 / 0,70	1,34 / 1,14
OSIII-b[†]	0,60 / 0,89	0,71 / 0,66	0,58 / 0,49	0,79 / 1,02	1,52 / 2,01
Average (SD)	*0,62 / 0,67*	*0,70 / 0,63*	*0,59 / 0,54*	*0,80 / 0,85*	*1,60 / 1,45*
	(0,03) / (0,15)	*(0,09) / (0,03)*	*(0,04) / (0,05)*	*(0,06) / (0,16)*	*(0,21) / (0,38)*

[&] There are listed only the conformations that successfully evolved to MCC and EPC.
* All heavy atoms of substrate and the SEA105 side chain.
[†] Exergonic reaction path.
[††] Endergonic reaction path.

Figure 30

RMSD for all heavy atoms of (R)- or (S)- and the side chain of SEA105 in the O-acylation catalyzed by Candida antarctica Lipase B In black color when TI-2 is formed from MCC and in blue color the evolution of TI-2 to EPC. ORI, ORI-b, ORI-c are configurations in binding mode I.

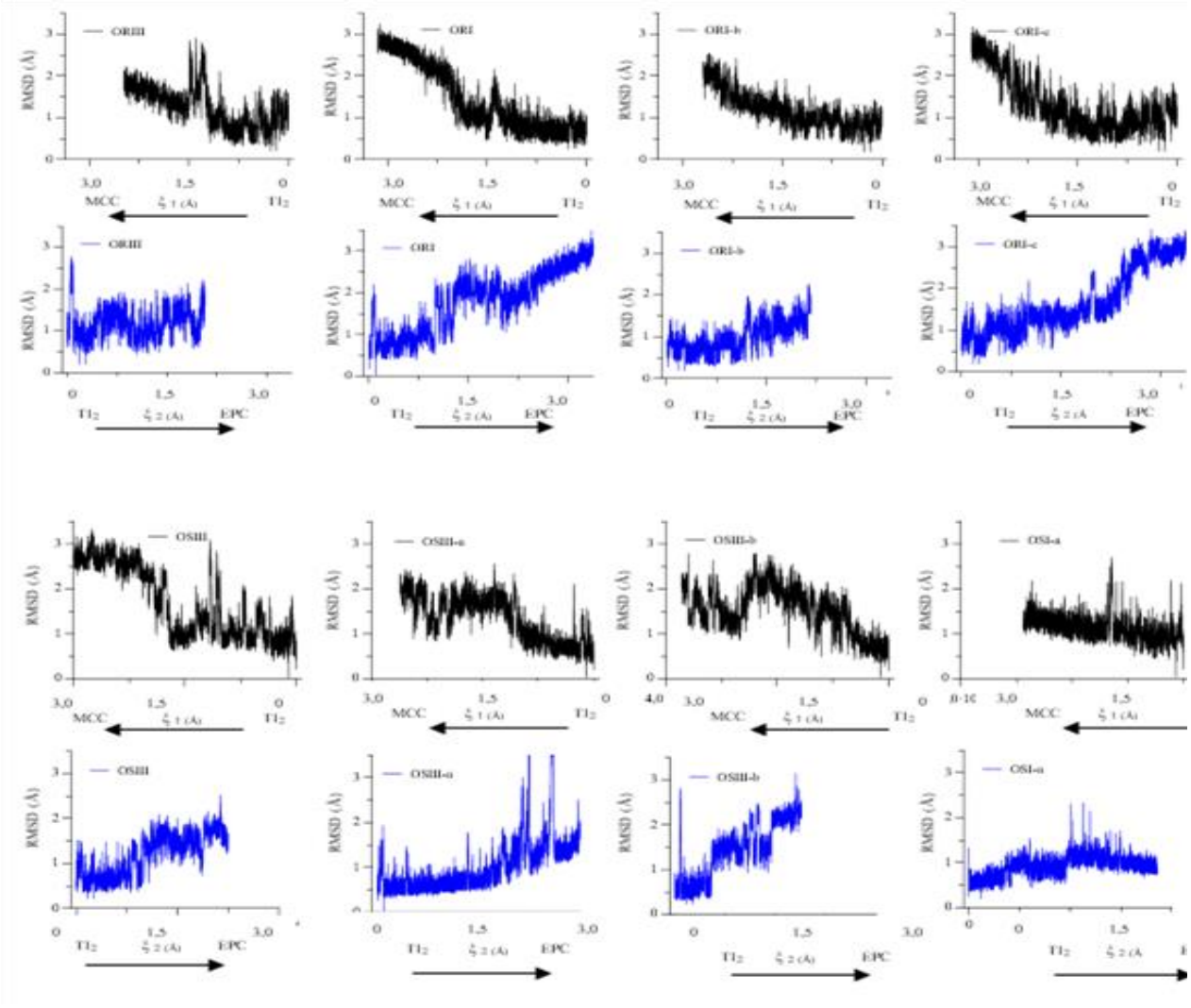

5.3.2.2. Relevant hydrogen bonds and reaction coordinate behavior in the deacylation step. The hydrogen bonds between the carbonylic oxygen of SEA105 side chain and the oxyanionic hole: Q106NH···EA105OE, T40NH···SEA105OE, and T40OH···SEA105OE, see distances -d-, -e-, and -f- dotted lines in Figure 9, have a different behavior when the reaction coordinates are explored. This result confirms the previous assumptions (Escorcia et al., 2017). As the MCC evolve to TI-2 along reaction coordinate ξ_1, the distance of the three hydrogen bonds is ~0,5Å shorter than in the MCC except when the sampling was performed in the EPC direction in the conformations ORI-c, OSI-a, and OSIII. The above indicates that carbonylic oxygen in SEA105 is more stabilized in TI-2 than MCC in the oxyanion hole. As the TI-2 evolve to EPC, monitoring by ξ_2, the hydrogen bonds Q106NH···EA105OE, T40NH···SEA105OE, distance -d-, and -e-, suffer an elongation reaching values near 5Å while the distance of the hydrogen bond T40OH···SEA105OE do not increases (Appendix M: Evolution of the hydrogen bonds between carbonylic oxygen of SEA105 and oxyanionic hole for the O-acylation of (R,S)-propranolol catalyzed by CalB in conformations ORIII-a and OSI-a).

The above indicates that carbonylic oxygen in SEA105 is more stabilized in TI-2 than MCC in the oxyanionic hole. As the TI-2 evolve to EPC, monitoring by ξ_2, the hydrogen bonds Q106NH···EA105OE, T40NH···SEA105OE, distance -d-, and -e-, suffer an elongation reaching values near 5Å while the distance of the hydrogen bond T40OH···SEA105OE do not increases.

These results show that a weakening of these interactions leads to the production of EPC from TI-2. Interestingly, in highly endergonic reaction pathways (ORIII-a and OSI-a TI-2 conformations) all of the three hydrogen bonds are below 3,0Å throughout ξ_2, hence given us a plausible response to the high endergonicity for the EPC production in (*R*)-propranolol in binding mode II and (*S*)-propranolol in binding mode I Appendix M: Evolution of the hydrogen bonds between carbonylic oxygen of SEA105 and oxyanionic hole for the *O-acylation* of (*R,S*)-propranolol catalyzed by CalB in conformations ORIII-a and OSI-a). The hydrogen bonds evolution used for define the reaction coordinates ξ_1 and ξ_2 Hys224N_εH

···PropO39 and Hys224N$_\varepsilon$H···SEA105OM, see distances -a- and -d- (Figure 9), were compared to the covalent bonds involved in the reaction coordinates PropO39—SEA105CE, and SEA105CE—OM, see distances -b- and -c- in (Figure 2), throughout of the acylation reaction along with the reaction coordinates (Figure 31, and Appendix N. Reaction coordinate behavior for the *O-acylation* of the (*R,S*)-propranolol in Binding mode I and II).

Figure 31

Reaction coordinate for the O-acylation of the (R)-propranolol in Binding mode I. Left: TI-2 formation from MCC is monitored by ξ_1, green lines. It is composed of the difference between the distance of covalent bond Prop$_{O39}$-SEA105$_{CE}$ and the hydrogen bond His224N$_\varepsilon$H···Prop$_{O39}$, red and black lines. Right: EPC formation from TI-2 is monitored by ξ_2, green line, and it is the difference between the distance of the covalent bond SEA105$_{CE}$-SEA105$_{OM}$, and the hydrogen bond His224N$_\varepsilon$H···SEA105$_{OM}$ magenta and blue lines (Figure 9).

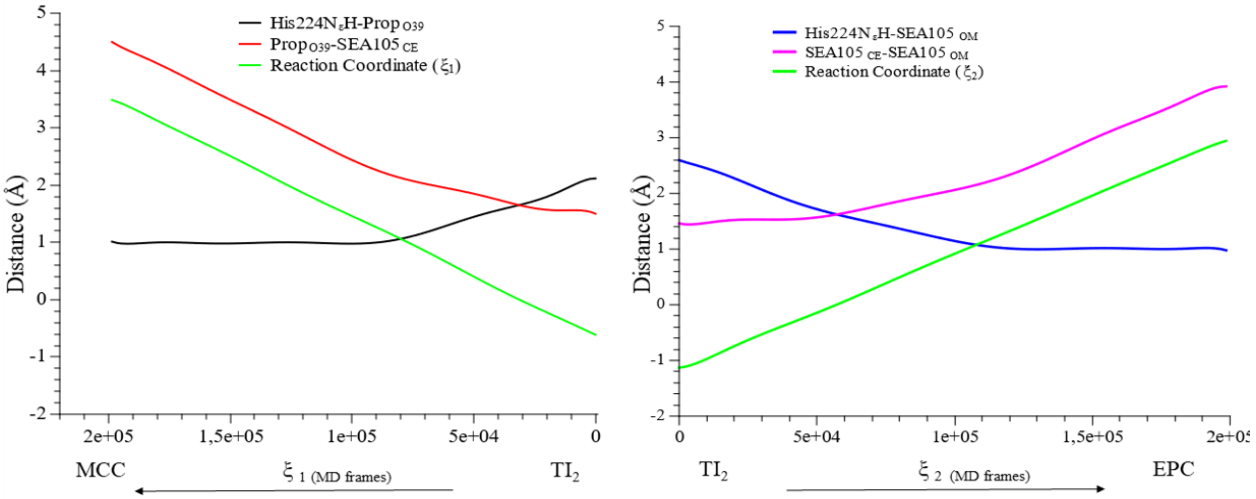

5.3.3. Potential energy surfaces.

Smooth, not fragmented SCC-DFTB-PES were selected. It was necessary to merge the PES found in ξ_1 or ξ_2 in all selected TI-2 conformations to analyze the potential energy throughout the O-acylation of (R,S)-propranolol catalyzed by CalB. To this end, the PES to convert the TI-2 from ξ_1 to the TI-2 in ξ was calculated. Finally, the PES obtained in ξ_1 and ξ_2 were merged. Interestingly, our results show that the minimum energy reaction energy path for each conformational snapshot is highly influenced by the small structural of the structures used in the calculations. This influence on the reaction barriers in the initial step of the acylation of Acetylcholinesterase (AChE) was previously reported (Zhang et al., 2003) interestingly, AChE and CalB share the same catalytic triad. Despite of this dependence, the SCC-DFT/CHARMM energy barriers found in this work are comparable to the DFTB/CHARMM energy barriers found previously reported (Escorcia et al., 2017). Our calculated energy barriers (4,0 kcal/mol to 18,1 kcal/mol) are in the same range as the energy barriers B3LYP/MM found in our previous publication (6,5 kcal/mol to 16,2 kcal mol) (Escorcia et al., 2017). All minimum energy paths from MCC to EPC have two energy barriers. The first leads the formation of the TI-2 from the MCC, the second, smaller one, leads the formation of EPC from TI-2 (Appendix O. QM(SCC-DFTB)/MM potential energy explorations for the conversion of (*R,S*)-propranolol to O-acetylpropranolol in binding modes I and II). This propensity confirms that TI-2 is not a good representation of transition states in this reaction as was previously reported using QM (B3LYP/TZVP)/CHARMM theory level (Escorcia et al., 2017) and in the PMF landscapes found in this work using QM (SCC-DFTB)/CHARMM MD for (*R*)-propranolol (Figure 32), and for (*S*)-propranolol (Appendix P. Finite-temperature effects for the conversion of (*S*)-propranolol to *O-acetylpropranolol* in binding modes I and II).

5.3.4. Finite-temperature effects

The comparison of the PMF and PES provides information about the finite temperature effects. In binding mode I, we analyzed conformations ORI, ORI-c, and OSI-a, and in binding mode II conformations ORIII-a, OSIII, and OSIII-a, see (Figure 32 and Appendix P. Finite-temperature effects for the

conversion of (*S*)-propranolol to *O-acetylpropranolol* in binding modes I and II). As mentioned above, the starting structure affects the potential energy barrier, and thus the calculated final temperature effect. Nevertheless, the PES and PMF are sufficiently different to see some trends: For the enantioselective step of the reaction (MCC → TI-2), finite temperature effects are smaller for (*R*)- than for (*S*)-propranolol. In all investigated reaction pathways, the TI-2 is higher on the free-energy surface than on the potential energy surface, less profound relative to the adjacent transition states, and also higher than the preceding Michaelis complex.

The superposition of the PMF and PES gave us information about the finite-temperature effect (f.t.e =PMF – PES). This effect was estimated in the reaction paths for (*R*)- and (*S*)-propranolol. In binding mode I the conformations ORI, ORI-c, and OSI-a were analyzed. In binding mode II were analyzed the conformations ORIII-a, OSIII, and OSIII-a. The difference between free energy barrier and potential energy barrier, at comparable values of RC, gave us insights about the finite-temperature effects (Table 7). As was previously found, the structural variation of the starting structure affects the potential energy barrier and, in consequence, affect the f.t.e. The f.t.e. values for the energy barrier to produce TI-2, the TI-2 and the energy barrier to produce EPC from TI-2 (Table 7).

For the enantioselective step of the reaction (MCC → TI-2), f.t.e are smaller for the (*R*)- than for the (*S*)-propranolol. f.t.e. help to increase the energy of the TI-2 in most of the reaction pathways explored, thus allowing its energy to be greater than that of the MCC, this result agrees with the energy diagram for the lipase-catalyzed reactions (Ema, 2004; Ema et al., 1998).

Figure 32

Finite-temperature effects for the conversion of (R)-propranolol to O-acetylpropranolol in binding modes I and II. ORI and ORIc are conformations of the TI-2 in binding mode I. ORIII-a is a conformation of the TI-2 in binding mode II. For comparison, the QM(B3LYP/TZVP)/CHARMM results calculations are showed at the top on the right. PMF is the magenta line. PES values are the lines red, black, and blue. Doted lines connect the electronic energy values reported previously.

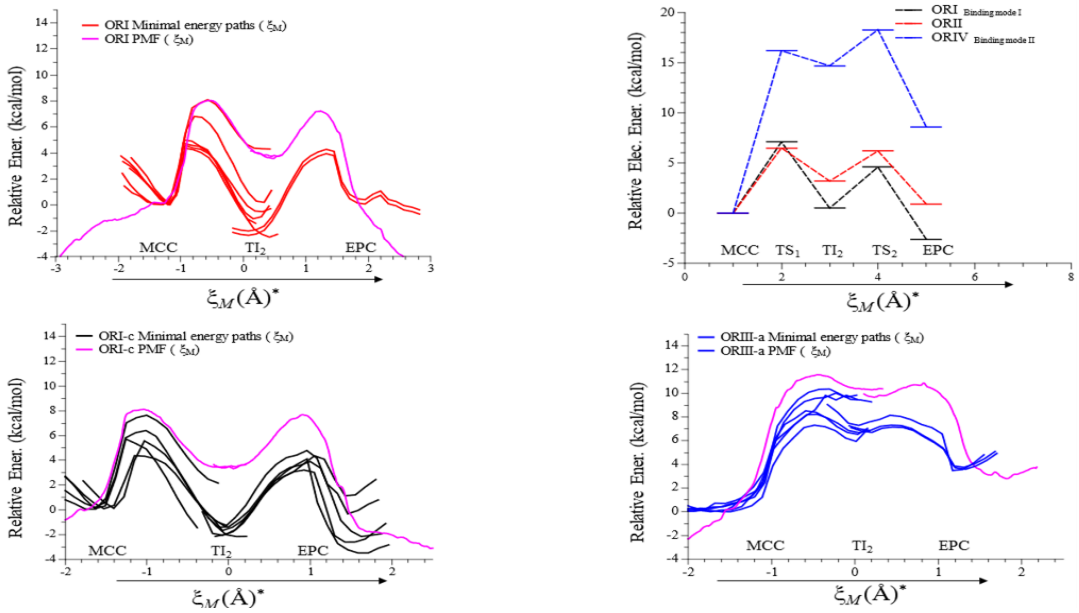

The comparison between PMF calculated with QM (SCC-DFTB/MM) MD and the energy values calculated with QM (B3LYP/TZVP)/MM theory level shows that energy barriers are comparable, in both binding modes (Figure 32 and Appendix P. Finite-temperature effects for the conversion of (*S*)-propranolol to *O-acetylpropranolol* in binding modes I and II).

The precision of the DFT method is higher than the semiempirical method SCC-DFT (Cui et al., 2001) for this reason, the QM (B3LYP/TZVP)/MM values are closer to experimental enantioselectivity than the PMF found in this work., but in the other hand in calculations with DFT we do not include f.t.e. As the f.t.e. was calculated as the difference between PMF and PES is possible to read this effect as the entropy effect.

Table 7

Finite-temperature effects (f.t.e.) for the O-acylation of the (R,S)-propranolol catalyzed by CalB.

TI-2 -conformations	*f.t.e.$_{\text{Barrier 1}}$			f.t.e $_{\text{TI-2}}$			f.t.e.$_{\text{Barrier 2}}$		
	†Min.	††Max.	Aver.	†Min.	††Max.	Aver.	†Min.	††Max.	Aver.
Binding Mode I									
ORI	0	3.7	2.4	0	2.9	1.3	5.7	5.7	5.7
ORI-c	0.5	3.7	2.2	4.5	5.2	4.9	2.8	4.4	3.54
OSI-a	3.3	8.1	6.2	3.1	10.5	7.2	**	**	**
Binding Mode II									
ORIII-a	1.2	4.3	2.6	0.8	4.5	2.8	2.6	3.6	3.2
OSIII	2.7	5.5	4.4	2.7	7.8	5.2	5.5	7.2	5.9
OSIII-a	0	7.8	5.0	-1.8	8.7	5.0	7.93	9.2	8.7

* All values were calculated as the difference between PMF value and PES and are normalized to MCC energy. PES-energy. † f.t.e. calculated as the difference between the PMF value and the highest value of the potential energy of the PES. †† f.t.e. calculated as the difference between the PMF value and the lowest value of the potential energy of the PES.

We can assume that the role of the entropy in the *O*-acylation of the propranolol catalyzed by CalB is to increase the TI-2 energy. In general, the effect of the entropy can reach values of ~8 kcal/mol; nevertheless, this does not have an appreciable effect in the relative energy barriers at the same RC values when is compared to potential energy (Figure 32 and Appendix P. Finite-temperature effects for the conversion of (*S*)-propranolol to *O-acetylpropranolol* in binding modes I and II**)**.

5.4. Conclusions

In this chapter, QM/MM MD simulations combined with umbrella potential have been performed to understand the finite-temperature effect in the CalB-catalyzed *O*-acetylation of (*R,S*)- propranolol in toluene. We calculate the free energy profiles for eight TI-2 conformations throughout the deacylation step of the reaction (MCC →TI-2 →EPC). 12 starting structures in two binding modes (I and II) of the TI-2 were selected for QM (SCC-DFTB)/MM(CHARMM) MD calculations. To this end, the result of the umbrella sampling was analyzed with the WHAM approach. The sampling was made using three different harmonics restraining constant k_u. The higher the value in the harmonic restraining potential constant (k_u), the higher are the population of the bins throughout the RC. The sampling time was seven times

higher than in similar studies focused on the enantioselectivity of lipases, in this way, ensuring none bias as a consequence of low sampling. Six conformations of the TI-2 were able to connect MCC and EPC. The free energy profiles show that in binding mode I the transformation of (*R*)-TI-propranolol to *O*-acetylpropranolol is exergonic and, for (*S*)-propranolol is endergonic. The values of the free energy barrier range from 9,7 to 13,4 kcal/mol for (*R*)-propranolol and between 9,3 to 14,9 kcal/mol for (*S*)-propranolol. Free energy profiles of (*R*)-propranolol in binding mode II and (*S*)-propranolol in binding mode I are highly endergonic. In binding mode I for (*R*)-propranolol and in binding mode II for (*S*)-propranolol, the formation of TI-2 and EPC is the reaction rate-determining step confirming the results previously obtained for the energy barrier. The average $\Delta PMF_{(ORI\text{-}c + ORI) - (OSIII\text{-}b + OSIII\text{-}a)}$ is -0,25kcal/mol. Even though these results cannot reproduce the experimental enantioselectivity, they are qualitatively comparable to QM (B3LYP-TZVP)/MM results. No conclusion concerning the enantioselectivity can be drawn here. To improve these results more reaction paths should be investigated. This would have at least a better statistical basis for the analysis.

To analyze finite temperature effects (f.t.e), we compare the PMF and the potential energy along the reaction coordinate. The role of the entropy is to increase the energy throughout the enantioselective step, and particularly a destabilization of the TI-2, resulting in a much higher barrier for the formation of the TI than for its decomposition. The entropic contribution to the free energy barrier from MCC to TI-2 can reach values as high as ~8kcal/mol for (*R*)-propranolol and between 4 to 5 kcal/mol for (*S*)-propranolol.

Chapter 6. Summary and General conclusions

This doctoral dissertation aimed to gain insights into the role of the entropy and analyzes the configurational space in the enantioselective acylation of (*R*,*S*)-propranolol catalyzed by lipase B of *Candida antarctica.* The research was focused on the analysis of configurational space during the enantioselective step using hybrid QM/MM methods. In the QM region, the semiempirical method SCC-DFTB was used, and the MM region was described by the CHARMM force field in all calculations. This dissertation started with the study of the MCCs, focusing on the conformational subspace of the NACs. Then a detailed study of the evolution in time of the TI-2 was carried out, including in the active region all the atoms of the lateral chains of the amino acid residues of the catalytic triad. From the selected structures of the TI-2, a sampling was carried out using the Umbrella sampling approach that, in conjunction with the WHAM method, allowed to know the free energy profiles of this reaction. Additionally, the exploration of the potential energy surface was performed. Smooth, and not fragmented SCC-DFTB-PES were selected to build the complete PMF (MCC→ TI-2→EPC) and were compared to free energy profiles to calculate the entropic effect.

The detailed analysis of Michaelis and Near-attack complexes (NACs) of the enantioselective step of the acylation of (*R*,*S*)-propranolol using a QM/MM MD simulation protocol indicates that NACs approach is helpful to gain insights of configurational space between MCC and the TI-2. The effect of different initial velocity distributions on NACs populations was not known, in enzyme kinetic resolution reactions, until the development of this thesis. Our results showed that the populations of the MCCs and the NACs are dependent on the distribution of the initial velocities (iseed number) used in the QM/MM MD. Despite this dependence, several propensities were found: i) The MCCs between (*S*)-propranolol and CalB are more stable than MCCs with (*R*)-propranolol. ii) The MCCs and the NACs present a longer lifetime when propranolol is oriented in the active site of CalB in binding mode I than in binding mode

II. This suggests that the prediction of the enantioselectivity of a reaction through NACs is not a reliable strategy; however, it gives light on the passage between the MCCs and the TI-2.

The time evolution of TI-2 of the *O*-acylation of (*R,S*)-propranolol catalyzed by CalB by a QM/MM MD approach indicated that the critical net of hydrogen bonds and covalent bonds in this reaction were stable throughout all MD (1ns). The hydrogen bonds at the oxyanionic hole were stronger than hydrogen bonds formed by H224 with D187, the (*R*,*S*)-propranolol, or SEA105. Additionally, it was found that the effect of an increase in the QM region does not affect the stability of the TI-2, but the conformational space change. Only 12 conformations in more than six thousand were comparable to those previously reported and used as starting conformations for electronic energy calculations.

Starting structures in two binding modes (I and II) of the TI-2 were selected for QM (SCC-DFTB)/MM(CHARMM) MD (umbrella sampling) calculations. The sampling was done using three different harmonics restraining constant k_u, and the sampling time was seven times higher than in similar studies focused on the enantioselectivity of lipases, in this way ensuring none bias as a consequence of low sampling. The free energy value of EPCs indicates that (*R*)-acetylated-propranolol are more exergonic than (*S*)-acetylated-propranolol. In binding mode I for (*R*)-propranolol and in binding mode II for (*S*)-propranolol, the formation of TI-2 and EPC is the reaction rate-determining step confirming the results previously obtained for the energy barrier. The average ΔPMF(ORI-c + ORI) – (OSIII-b + OSIII-a) is -0,25kcal/mol.

The minimum energy reaction energy path for each snapshot is highly influenced by the small structural fluctuations. However, for the minimum energy reaction energy paths that connect to MCC or EPC showed an appreciable propensity: There is one energetic barrier previous to TI-2 formation from MCC, and there is another energetic barrier, smaller than the latter, to produce the EPC.

The superposition of the PMF and PES gave us information about the finite-temperature effect (f.t.e =PMF – PES). This effect was estimated in the reaction paths for (*R*)- and (*S*)-propranolol. The difference

between free energy barrier and potential energy barrier, at comparable values of RC, gave us insights about the finite-temperature effect. As the finite-temperature effect was calculated as the difference between PMF and PES is possible to read this effect as the entropy effect. However, due to the number of PMF found and the precision of the SCC-DFTB semiempirical method, no conclusion respect to the enantioselectivity can be drawn here.

References

Ansorge-Schumacher, M. B., & Thum, O. (2013). Immobilised lipases in the cosmetics industry. *Chemical Society Reviews*, *42*(15), 6475–6490. https://doi.org/10.1039/c3cs35484a

Bangalore, S., Messerli, F. H., Kostis, J. B., & Pepine, C. J. (2007). Cardiovascular Protection Using Beta-Blockers. A Critical Review of the Evidence. *Journal of the American College of Cardiology*, *50*(7), 563–572. https://doi.org/10.1016/j.jacc.2007.04.060

Bangalore, S., Parkar, S., Grossman, E., & Messerli, F. H. (2007). A Meta-Analysis of 94,492 Patients with Hypertension Treated With Beta Blockers to Determine the Risk of New-Onset Diabetes Mellitus. *American Journal of Cardiology*, *100*(8), 1254–1262. https://doi.org/10.1016/j.amjcard.2007.05.057

Barbosa, O., Ariza, C., Ortiz, C., & Torres, R. (2010). Kinetic resolution of (R/S)-propranolol (1-isopropylamino-3-(1-naphtoxy)-2-propanolol) catalyzed by immobilized preparations of Candida antarctica lipase B (CAL-B). *New Biotechnology*, *27*(6), 844–850. https://doi.org/10.1016/j.nbt.2010.07.015

Barrera Valderrama, D. I., Doerr, M., & Daza E, M. C. (2018). Función de los confórmeros de ataque cercano en la acilación enantioselectiva del (R,S)-propranolol catalizada por lipasa B de Candida antarctica. *Revista Colombiana de Biotecnologia*, *20*(1), 16–30. https://doi.org/10.15446/rev.colomb.biote.v20n1.73652

Barrett, A. (1985). Cardiac beta-adrenoceptor blockade: the quest for selectivity. *Journal de Pharmacologie*, *16*(2), 95–108. http://www.ncbi.nlm.nih.gov/pubmed/2867254

Bianco, G., Forli, S., Goodsell, D. S., & Olson, A. J. (2016). Covalent docking using autodock: Two-point attractor and flexible side chain methods. *Protein Science*, *25*(1), 295–301. https://doi.org/10.1002/pro.2733

Billeter, S. R., Turner, A. J., & Thiel, W. (2000). Linear scaling geometry optimisation and transition state search in hybrid delocalised internal coordinates. *Physical Chemistry Chemical Physics*, *2*(10), 2177–2186. https://doi.org/10.1039/a909486e

Bocola, M., Otte, N., Jaeger, K. K., Reetz, M. M. T., & Thiel, W. (2004). Learning from Directed Evolution: Theoretical Investigations into Cooperative Mutations in Lipase Enantioselectivity. *Chembiochem : A European Journal of Chemical Biology*, *5*(2), 214–223. https://doi.org/10.1002/cbic.200300731

Brooks, B. R. and Brooks, III, C. L. and Mackerell, Jr., A. D. and, Nilsson, L. and Petrella, R. J. and Roux, B. and Won, Y. and A., G. and Bartels, C. and Boresch, S. and Caflisch, A. and Caves, L.

and, Cui, Q. and Dinner, A. R. and Feig, M. and Fischer, S. and Gao, J. and, Hodoscek, M. and Im, W. and Kuczera, K. and Lazaridis, T. and Ma, J., and Ovchinnikov, V. and Paci, E. and Pastor, R. W. and Post, C. B. and, Pu, J. Z. and Schaefer, M. and Tidor, B. and Venable, R. M. and, & Woodcock, H. L. and Wu, X. and Yang, W. and York, D. M. and Karplus, M. (2009). CHARMM: The Biomolecular Simulation Program. *Journal of Computational Chemistry*, *30*, 1545–1614. https://doi.org/10.1002/jcc.21287

Bruice, T. C. (2002). A view at the millennium: The efficiency of enzymatic catalysis. *Accounts of Chemical Research*, *35*(3), 139–148. https://doi.org/10.1021/ar0001665

Bruice, T. C., & Benkovic, S. J. (2000). Chemical basis for enzyme catalysis. In *Biochemistry* (Vol. 39, Issue 21, pp. 6267–6274). https://doi.org/10.1021/bi0003689

Busto, E., Gotor-Fernández, V., & Gotor, V. (2011). Hydrolases in the stereoselective synthesis of N-heterocyclic amines and amino acid derivatives. *Chemical Reviews*, *111*(7), 3998–4035. https://doi.org/10.1021/cr100287w

Callender, R., & Dyer, R. B. (2015). The dynamical nature of enzymatic catalysis. *Accounts of Chemical Research*, *48*(2), 407–413. https://doi.org/10.1021/ar5002928

Chiou, T.-W., Chang, C.-C., Lai, C.-T., & Tai, D.-F. (1997). Kinetic Resolution of Propranolol by a Lipase-Catalyzed N-Acetylation. *Bioorganic & Medicinal Chemistry Letters*, *7*(4), 433–436. https://doi.org/10.1016/S0960-894X(97)00028-0

Cino, E. A., Choy, W. Y., & Karttunen, M. (2012). Comparison of secondary structure formation using 10 different force fields in microsecond molecular dynamics simulations. *Journal of Chemical Theory and Computation*, *8*(8), 2725–2740. https://doi.org/10.1021/ct300323g

Cui, Q., Elstner, M., Kaxiras, E., Frauenheim, T., & Karplus, M. (2001). A QM/MM Implementation of the Self-Consistent Charge Density Functional Tight Binding (SCC-DFTB) Method. *The Journal of Physical Chemistry B*, *105*(2), 569–585. https://doi.org/10.1021/jp0029109

Dewar, M. J. S., Zoebisch, E. G., Healy, E. F., & Stewart, J. J. P. (1985). Development and use of quantum mechanical molecular models. 76. AM1: a new general purpose quantum mechanical molecular model. *Journal of the American Chemical Society*, *107*(13), 3902–3909. https://doi.org/10.1021/ja00299a024

Dral, P. O., Wu, X., Spörkel, L., Koslowski, A., & Thiel, W. (2016). Semiempirical Quantum-Chemical Orthogonalization-Corrected Methods: Benchmarks for Ground-State Properties. *J. Chem. Theory Comput.* https://doi.org/10.1021/acs.jctc.5b01047

Elstner, M., Porezag, D., Jungnickel, G., Elsner, J., Haugk, M., Frauenheim, T., Suhai, S., & Seifert, G. (1998). Self-consistent-charge density-functional tight-binding method for simulations of complex materials properties. In *Physical Review B* (Vol. 58, Issue 11, pp. 7260–7268). https://doi.org/10.1103/PhysRevB.58.7260

Ema, T. (2004). Mechanism of Enantioselectivity of Lipases and Other Synthetically Useful Hydrolases. *Current Organic Chemistry*, *8*(11), 1009–1025. https://doi.org/10.2174/1385272043370230

Ema, T., Kobayashi, J., Maeno, S., Sakai, T., & Utaka, M. (1998). Origin of the Enantioselectivity of Lipases Explained by a Stereo-Sensing Mechanism Operative at the Transition State. *Bulletin of the Chemical Society of Japan*, *71*, 443–453. https://doi.org/10.1246/bcsj.71.443

Escorcia, A. M. (2015). *Enantioselective and Chemoselective Acylation of (R,S)-Propranolol Catalyzed by Candida antarctica Lipase B: A Theoretical and Experimental Approach*. Universidad Industrial de Santander.

Escorcia, A. M., Daza, M. C., & Doerr, M. (2014). Computational study of the enantioselectivity of the O-acetylation of (R,S)-propranolol catalyzed by Candida antarctica lipase B. *Journal of Molecular Catalysis B: Enzymatic*, *108*, 21–31. https://doi.org/10.1016/j.molcatb.2014.06.010

Escorcia, A. M., Molina, D., Daza, M. C., & Doerr, M. (2013). Acetylation of (R,S)-propranolol catalyzed by Candida antarctica lipase B: An experimental and computational study. *Journal of Molecular Catalysis B: Enzymatic*, *98*, 21–29. https://doi.org/10.1016/j.molcatb.2013.09.019

Escorcia, A. M., Sen, K., Daza, M. C., Doerr, M., & Thiel, W. (2017). Quantum Mechanics/Molecular Mechanics Insights into the Enantioselectivity of the O-Acetylation of (R,S)-Propranolol Catalyzed by Candida antarctica Lipase B. *ACS Catalysis*, *7*(1), 115–127. https://doi.org/10.1021/acscatal.6b02310

Ferrari, F., Paris, C., Maigret, B., Bidouil, C., Delaunay, S., Humeau, C., & Chevalot, I. (2014). Molecular rules for chemo- and regio-selectivity of Candida antarctica lipase B in peptide acylation reactions. *Journal of Molecular Catalysis B: Enzymatic*, *101*, 122–132. https://doi.org/10.1016/j.molcatb.2013.12.007

Foresman, J., & Frisch, A. (1996). Exploring chemistry with electronic structure methods, 1996. In *Gaussian Inc, Pittsburgh, PA*.

Galunsky, B., Ignatova, S., & Kasche, V. (1997). Temperature effects on S1- and S'1-enantioselectivity of α- chymotrypsin. *Biochimica et Biophysica Acta - Protein Structure and Molecular Enzymology*, *1343*(1), 130–138. https://doi.org/10.1016/S0167-4838(97)00136-2

Gao, J., Amara, P., Alhambra, C., & Field, M. J. (1998). A Generalized Hybrid Orbital ({G}{H}{O}) Method for the Treatment of Boundary Atoms in Combined {Q}{M}/{M}{M} Calculations. *J. Phys. Chem. A*, *102*(98), 4714. https://doi.org/10.1021/jp9809890

García-Urdiales, E., Ríos-Lombardía, N., Mangas-Sánchez, J., Gotor-Fernández, V., & Gotor, V. (2009). Influence of the nucleophile on the Candida antarctica lipase B-catalysed resolution of a chiral acyl donor. *Chembiochem : A European Journal of Chemical Biology*, *10*(11), 1830–1838. https://doi.org/10.1002/cbic.200900204

Ghanem, A. (2007). Trends in lipase-catalyzed asymmetric access to enantiomerically pure/enriched compounds. *Tetrahedron*, *63*(8), 1721–1754. https://doi.org/10.1016/j.tet.2006.09.110

Ghanem, A., & Aboul-Enein, H. Y. (2004). Lipase-mediated chiral resolution of racemates in organic solvents. *Tetrahedron: Asymmetry*, *15*(21), 3331–3351. https://doi.org/10.1016/j.tetasy.2004.09.019

Giraldo, J., Roche, D., Rovira, X., & Serra, J. (2006). The catalytic power of enzymes: Conformational selection or transition state stabilization? *FEBS Letters*, *580*(9), 2170–2177. https://doi.org/10.1016/j.febslet.2006.03.060

Giustino, T. F., Fitzgerald, P. J., & Maren, S. (2016). Revisiting propranolol and PTSD: Memory erasure or extinction enhancement? *Neurobiology of Learning and Memory*, *130*, 26–33. https://doi.org/10.1016/j.nlm.2016.01.009

Gotor-Fernández, V., Brieva, R., & Gotor, V. (2006). Lipases: Useful biocatalysts for the preparation of pharmaceuticals. *Journal of Molecular Catalysis B: Enzymatic*, *40*(3–4), 111–120. https://doi.org/10.1016/j.molcatb.2006.02.010

Griffin, J. L., Bowler, M. W., Baxter, N. J., Leigh, K. N., Dannatt, H. R. W., Hounslow, A. M., Blackburn, G. M., Webster, C. E., Cliff, M. J., & Waltho, J. P. (2012). Near attack conformers dominate β-phosphoglucomutase complexes where geometry and charge distribution reflect those of substrate. *Proceedings of the National Academy of Sciences of the United States of America*, *109*(18), 6910–6915. https://doi.org/10.1073/pnas.1116855109

Hedstrom, L. (2002). Serine Protease Mechanism and Specificity. *Chemical Reviews*, *102*(12), 4501–4524. https://doi.org/10.1021/cr000033x

Huang, S.-Y., Grinter, S. Z., & Zou, X. (2010). Scoring functions and their evaluation methods for protein-ligand docking: recent advances and future directions. *Physical Chemistry Chemical Physics : PCCP*, *12*(40), 12899–12908. https://doi.org/10.1039/c0cp00151a

Humphrey, W., Dalke, A., & Schulten, K. (1996). VMD - Visual Molecular Dynamics. *J. Molec. Graphics*, *14*, 33–38. https://doi.org/10.1016/0263-7855(96)00018-5

Hur, S., & Bruice, T. C. (2003). The near attack conformation approach to the study of the chorismate to prephenate reaction. *Proceedings of the National Academy of Sciences of the United States of America*, *100*(21), 12015–12020.

Jia, X., Zhang, L., & Mao, X. (2015). S-propranolol protected H9C2 cells from ischemia/reperfusion-induced apoptosis via downregultion of RACK1 Gene. *International Journal of Clinical and Experimental Pathology*, *8*(9), 10335–10344.

Joubioux, F. Le, Bridiau, N., Henda, Y. Ben, Achour, O., Graber, M., & Maugard, T. (2013). The control of Novozym® 435 chemoselectivity and specificity by the solvents in acylation reactions of amino-alcohols. *Journal of Molecular Catalysis B: Enzymatic*, *95*, 99–110. https://doi.org/10.1016/j.molcatb.2013.06.002

Kamal, A., Sandbhor, M., & Ali Shaik, A. (2004). Chemoenzymatic synthesis of (S) and (R)-propranolol and sotalol employing one-pot lipase resolution protocol. *Bioorganic and Medicinal Chemistry Letters*, *14*(17), 4581–4583. https://doi.org/10.1016/j.bmcl.2004.05.084

Khan, N., McAlister, F. A., & McCormack, J. P. (2007). Rebuttal: Do beta-blockers have a role in treating hypertension? Yes. *Can Fam Physician*, *53*(5), 800–803. https://doi.org/53/5/800 [pii]

Kohen, A. (2015). Role of dynamics in enzyme catalysis: Substantial versus semantic controversies. *Accounts of Chemical Research*, *48*(2), 466–473. https://doi.org/10.1021/ar500322s

Korth, M., & Thiel, W. (2011). Benchmarking semiempirical methods for thermochemistry, kinetics, and non-covalent interactions: OMx methods are almost as accurate and robust as DFT-GGA methods for organic molecules. *Journal of Chemical Theory and Computation*, *7*(9), 2929–2936. https://doi.org/10.1021/ct200434a

Kottalam, J., & Case, D. A. (1988). Dynamics of ligand escape from the heme pocket of myoglobin. *Journal of the American Chemical Society*, *110*(23), 7690–7697. https://doi.org/10.1021/ja00231a018

Kumar, S., Rosenberg, J. M., Bouzida, D., Swendsen, R. H., & Kollman, P. A. (1992). THE weighted histogram analysis method for free???energy calculations on biomolecules. I. The method. *Journal of Computational Chemistry*, *13*(8), 1011–1021. https://doi.org/10.1002/jcc.540130812

Leaute-Labreze, C., Boccara, O., Degrugillier-Chopinet, C., Mazereeuw-Hautier, J., Prey, S., Lebbe, G., Gautier, S., Ortis, V., Lafon, M., Montagne, A., Delarue, A., & Voisard, J.-J. (2016). Safety of Oral Propranolol for the Treatment of Infantile Hemangioma: A Systematic Review. *Pediatrics*, *138*(4), e20160353–e20160353. https://doi.org/10.1542/peds.2016-0353

Lewars, E. (2011). *Computational Chemistry. Introduction to the Theory and Applications of Molecular and Quantum Mechanics* (dept. C. Prof. Errol Lewars (Trent University (ed.); 2nd ed.). Springer Science+Bussines Media BV https://doi.org/10.1007/978-90-841-3762-3

Lightstone, F. C., & Bruice, T. C. (1996). Ground state conformations and entropic and enthalpic factors in the efficiency of intramolecular and enzymatic reactions .1. Cyclic anhydride formation by substituted glutarates, succinate, and 3,6-endoxo-Delta(4)-tetrahydrophthalate monophenyl esters. *Journal of the American Chemical Society*, *118*(11), 2595–2605. https://doi.org/10.1021/ja952589l

Linder, M., Hermansson, A., Liebeschuetz, J., & Brinck, T. (2011). Computational design of a lipase for catalysis of the Diels-Alder reaction. *Journal of Molecular Modeling*, *17*(4), 833–849. https://doi.org/10.1007/s00894-010-0775-8

Mackerell, A. D. (2004). Empirical force fields for biological macromolecules: Overview and issues. *Journal of Computational Chemistry*, *25*(13), 1584–1604. https://doi.org/10.1002/jcc.20082

Mathpati, A. C., & Bhanage, B. M. (2018). Prediction of enantioselectivity of lipase catalyzed kinetic resolution using umbrella sampling. *Journal of Biotechnology*, *283*(July), 70–80. https://doi.org/10.1016/j.jbiotec.2018.07.024

Matta, C. F. (2010). Quantum Biochemistry. In Matta Chérif F. (Ed.), *Quantum Biochemistry*. WILEY-VCH Verlag GmbH & Co. KGaA. https://doi.org/10.1002/9783527629213

Mazumder-Shivakumar, D., Kahn, K., & Bruice, T. C. (2004). Computational Study of the Ground State of Thermophilic Indole Glycerol Phosphate Synthase: Structural Alterations at the Active Site with Temperature. *J. Am. Chem. Soc.*, *126*, 5936–5937. https://doi.org/10.1021/ja049512u

Metz, S., Kästner, J., Sokol, A. A., Keal, T. W., & Sherwood, P. (2014). ChemShell - a modular software package for QM/MM simulations. *WIREs Comput. Mol. Sci.*, *4*, 101–110. https://doi.org/10.1002/wcms.1163

Naik, S., Basu, A., Saikia, R., Madan, B., Paul, P., Chaterjee, R., Brask, J., & Svendsen, A. (2010). Lipases for use in industrial biocatalysis: Specificity of selected structural groups of lipases. *Journal of Molecular Catalysis B: Enzymatic*, *65*(1–4), 18–23. https://doi.org/10.1016/j.molcatb.2010.01.002

Neri, C. (2015). Recent Advances in Stereoselective Drug Targeting. *Chirality*, *27*, 589–597. https://doi.org/10.1002/chir

Northrup, S., Pear, M., Lee, C., McCammon, J., & Karplus, M. (1982). Dynamical theory of activated processes in globular proteins. *Proc. Natl. Acad. Sci. USA*, *79*, 4035–4039. https://doi.org/10.1073/pnas.79.13.4035

Nyhlén, J., Martín-Matute, B., Sandström, A. G., Bocola, M., & Bäckvall, J. J. (2008). Influence of delta-functional groups on the enantiorecognition of secondary alcohols by Candida antarctica lipase B. *Chembiochem : A European Journal of Chemical Biology*, *9*(12), 1968–1974. https://doi.org/10.1002/cbic.200800036

Ottosson, J., & Hult, K. (2001). Influence of acyl chain length on the enantioselectivity of Candida antarctica lipase B and its thermodynamic components in kinetic resolution of sec-alcohols. *Journal of Molecular Catalysis - B Enzymatic*, *11*(4–6), 1025–1028. https://doi.org/10.1016/S1381-1177(00)00088-6

Ottosson, J., Rotticci-mulder, J. C., & Rotticci, D. (2001). Rational design of enantioselective enzymes requires considerations of entropy. *Protein Science*, *10*, 1769–1774. https://doi.org/10.1101/ps.13501.would

Overbeeke, P. L. a, Orrenius, S. C., Jongejan, J. a., & Duine, J. a. (1998). Enthalpic and entropic contributions to lipase enantioselectivity. *Chemistry and Physics of Lipids*, *93*(1–2), 81–93. https://doi.org/10.1016/S0009-3084(98)00031-0

Pu, J., Gao, J., & Truhlar, D. G. (2004). Combining self-consistent-charge density-functional tight-binding (SCC-DFTB) with molecular mechanics by the generalized hybrid orbital (GHO) method. *Journal of Physical Chemistry A*, *108*, 5454–5463. https://doi.org/10.1021/jp049529z

Qin, B., Liang, P., Jia, X., Zhang, X., Mu, M., Wang, X.-Y., Ma, G.-Z., Jin, D.-N., & You, S. (2013). Directed evolution of Candida antarctica lipase B for kinetic resolution of profen esters. *Catalysis Communications*, *38*, 1–5. https://doi.org/10.1016/j.catcom.2013.03.040

Rabkin, R., Stables, D. P., & Levin, N. W. (1966). The Prophylactic Value of Propranolol in Angina Pectoris. *The American Journal of Cardiology*, *18*, 370–380. https://doi.org/10.1016/0002-9149(66)90056-7

Roux, B. (1995). The calculation of the potential of mean force using computer simulations. *Computer Physics Communications*, *91*, 275–282. https://doi.org/10.1016/0010-4655(95)00053-I

Ryckaert, J., Ciccotti, G., & Berendsen, H. (1977). Numerical integration of the cartesian equations of motion of a system with constraints: molecular dynamics of n-alkanes. *J. Comput. Phys.*, *23*, 327–341.

Sakai, T., Kawabata, I., Kishimoto, T., Ema, T., & Utaka, M. (1997). *Enhancement of the Enantioselectivity in Lipase-Catalyzed Kinetic Resolutions of 3-Phenyl-2 H -azirine-2-methanol by Lowering the Temperature to - 40 ° C out preferentially at - 40 ° C in ether under unusual conditions for enzyme . We disclosed that a lip*. *3*(16), 4906–4907.

Salihu, A., & Alam, M. Z. (2015). Solvent tolerant lipases: A review. *Process Biochemistry*, *50*(1), 86–96. https://doi.org/10.1016/j.procbio.2014.10.019

Sasai, H., Itoh, N., Suzuki, T., & Shibasaki, M. (1993). Catalytic asymmetric nitroaldol reaction: An efficient synthesis of (S) propranolol using the lanthanum binaphthol complex. *Tetrahedron Letters*, *34*(5), 855–858. https://doi.org/10.1016/0040-4039(93)89031-K

Schenter, G. K., Garrett, B. C., & Truhlar, D. G. (2003). Generalized transition state theory in terms of the potential of mean force. *Journal of Chemical Physics*, *119*(12), 5828–5833. https://doi.org/10.1063/1.1597477

Schlick, T. (2010). *Molecular Modeling and Simulation: An Interdisciplinary Guide* (Antman S (University of Maryland/Institute fo Physical Science and Technology),) M. J. (California I. of T. C. and D. S., & S. L. (Mt. S. S. of M. of Biomathematics) (eds.); 2nd ed.). Springer Science+Bussines Media, LLC 2010. https://doi.org/10.1007/978-1-4419-6351-2

Seabra, G. D. M., Walker, R. C., Elstner, M., Case, D. a., & Roitberg, A. E. (2007). Implementation of the SCC-DFTB method for hybrid QM/MM simulations within the Amber molecular dynamics package. *Journal of Physical Chemistry A*, *111*, 5655–5664. https://doi.org/10.1021/jp0700711

Senn, H. M., Kästner, J., Breidung, J., & Thiel, W. (2009). Finite-temperature effects in enzymatic reactions — Insights from QM/MM free-energy simulations. *Canadian Journal of Chemistry*, *87*(10), 1322–1337. https://doi.org/10.1139/V09-092

Senn, H. M., & Thiel, W. (2007). QM / MM Methods for Biological Systems. *Topics in Current Chemistry*, *268*(November 2006), 173–290. https://doi.org/10.1007/128_2006_084

Senn, H. M., & Thiel, W. (2009). QM/MM methods for biomolecular systems. *Angewandte Chemie (International Ed. in English)*, *48*(7), 1198–1229. https://doi.org/10.1002/anie.200802019

SennHM, & Thiel W. (2007). QM/MM Methods for Biological Systems. In Atomistic Approaches in Modern Biology. In Markus Reiher (Ed.), *Atomistic Approaches in Modern Biology From Quantum Chemistry to Molecular Simulations* (pp. 173–290). Springer Berlin Heidelberg. https://doi.org/10.1007/128_2006_084

Souaille, M., & Roux, B. (2001). Extension to weighted histogram analysis method: combined umbrella sampling with free energy calculations. *Computer Physics Communications*, *135*, 40–57.

Sousa, S. F., Fernandes, P. A., & Joao, R. M. (2006). Protein–Ligand Docking: Current Status and Future Challenges. *Proteins: Structure, Function, and Bioinformatics*, *65*, 15–26. https://doi.org/10.1002/prot

Steenen, S. A., Van Wijk, A. J., Van Der Heijden, G. J. M. G., Van Westrhenen, R., De Lange, J., & De Jongh, A. (2016). Propranolol for the treatment of anxiety disorders: Systematic review and meta-analysis. *Journal of Psychopharmacology*, *30*(2), 128–139. https://doi.org/10.1177/0269881115612236

Stote, R., States, D., & Karplus, M. (1991). On the treatment of electrostatic interactions in biomolecular simulation. *J. Chim. Phys.*, *88*, 2419–2433.

Štrajbl, M., Shurki, A., Kato, M., & Warshel, A. (2003). Apparent NAC effect in chorismate mutase reflects electrostatic transition state stabilization. *Journal of the American Chemical Society*, *125*(34), 10228–10237.

Świderek, K., & Moliner, V. (2015). Computational Studies of Candida Antarctica Lipase B to Test Its Capability as a Starting Point to Redesign New Diels-Alderases. *The Journal of Physical Chemistry B*, *120*, 2053–2070. https://doi.org/10.1021/acs.jpcb.5b10527

Torres, R. A., & Bruice, T. C. (2000). The mechanism of phosphodiester hydrolysis: Near in-line attack conformations in the hammerhead ribozyme. *Journal of the American Chemical Society*, *122*(5), 781–791. https://doi.org/10.1021/ja993094p

Torrie, G., & Valleau, J. (1977). Nonphysical sampling distributions in monte carlo free-energy estimation: Umbrella sampling. *J Comp Phys*, *23*, 187–199.

Trott, O., & Olson, A. J. (2011). AutoDock Vina: improving the speed and accuracy of docking with a new scoring function, efficient optimization and multithreading. *Journal of Computational Chemistry*, *29*(2), 455–461. https://doi.org/10.1002/jcc.21334

Truhlar, D. G. (2015). Transition state theory for enzyme kinetics. *Archives of Biochemistry and Biophysics*, *582*, 10–17. https://doi.org/10.1016/j.abb.2015.05.004

Turki, S. (2013). Towards the development of systems for high-yield production of microbial lipases. *Biotechnology Letters*, *35*(10), 1551–1560. https://doi.org/10.1007/s10529-013-1256-9

Tuttle, T., & Thiel, W. (2008). OMx-D: semiempirical methods with orthogonalization and dispersion corrections. Implementation and biochemical application. *Physical Chemistry Chemical Physics : PCCP*, *10*(16), 2159–2166. https://doi.org/10.1039/b718795e

Uppenberg, J., Hansen, M. T., Patkar, S., & Jones, T. A. (1994). The sequence, crystal structure determination and refinement of two crystal forms of lipase B from Candida antarctica. *Structure*, *2*(4), 293–308. https://doi.org/10.1016/S0969-2126(00)00031-9

Uppenberg, J., Ohrner, N., Norin, M., Hult, K., Kleywegt, G. J., Patkar, S., Waagen, V., Anthonsen, T., & Jones, T. A. (1995). Crystallographic and molecular-modeling studies of lipase B from Candida

antarctica reveal a stereospecificity pocket for secondary alcohols. *Biochemistry*, *34*(51), 16838–16851. https://doi.org/10.1021/bi00051a035

Ursoiu, A., Paul, C., Kurtán, T., & Péter, F. (2012). Sol-gel entrapped Candida antarctica lipase B--a biocatalyst with excellent stability for kinetic resolution of secondary alcohols. *Molecules (Basel, Switzerland)*, *17*(11), 13045–13061. https://doi.org/10.3390/molecules171113045

Van Pham, V., Phillips, R. S., & Ljungdahl, L. G. (1989). Temperature-Dependent Enantiospecificity of Secondary Alcohol Dehydrogenase from Thermoanaerobacter ethanolicus. *Journal of the American Chemical Society*, *111*(5), 1935–1936. https://doi.org/10.1021/ja00187a089

Veloo, R. A., & Koomen, G.-J. (1993). Synthesis of Enantiomerically Pure (S) - (-) -Propranolol from Sorbitol. *Tetrahedron: Asymmetry*, *4*(12), 2401–2404. https://doi.org/10.1016/S0957-4166(00)82209-0

Xu, T., Zhang, L., Su, E., Cui, D., Wang, X., & Wei, D. (2010). Disparity in productive binding mode of the slow-reacting enantiomer determines the novel catalytic behavior of Candida antarctica lipase B. *Journal of Molecular Catalysis B: Enzymatic*, *62*(3–4), 288–296. https://doi.org/10.1016/j.molcatb.2009.11.011

Zelaszczyk, D., & Kiec, K. (2007). Biocatalytic Approaches to Optically Active -Blockers. *Current Medicinal Chemistry*, *14*, 53–65. https://doi.org/10.2174/092986707779313480

Zhang, Y., Kua, J., & Mccammon, J. A. (2003). Influence of Structural Fluctuation on Enzyme Reaction Energy Barriers in Combined Quantum Mechanical / Molecular Mechanical Studies. *Journal of Physical Chemistry B.*, *107*, 4459–4463. https://doi.org/10.1021/jp022525e

Appendix A: Graphical representation of a Near Attack Conformer

Figure 33

Near-attack conformation: This conformation is characterized by having reacting atoms within 3,2 Å and an approach angle for reaction of +/- 15° of the bonding angle in the transition state. A distance of 3,2 Å places the reacting atoms at a contact distance equal to about the sum of their van der Waals radii. The energy of the conformers does not change when the angle of approach deviates by +/-15° from the bonding angle in the transition state for nucleophilic attack on Sp3 or Sp2 carbons. (Bruice, 2002; Bruice & Benkovic, 2000; Hur & Bruice, 2003).

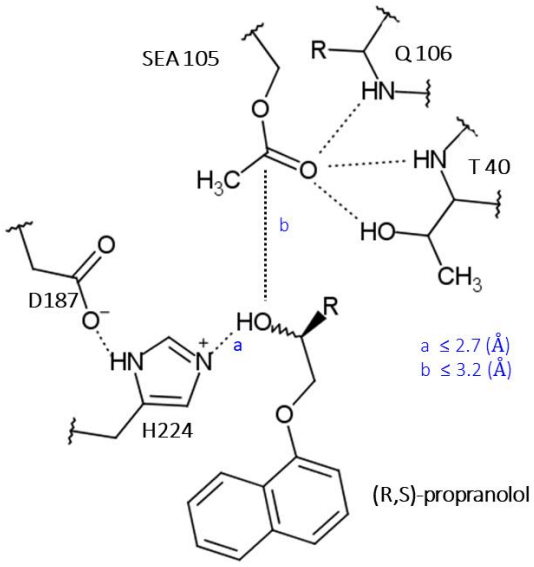

Appendix B: Computational details for acetylated serine 105 in *Candida antarctica* Lipase B

CHARMM parameters for the acetylated serine (SEA) The topology for the SEA residue (see below) was created by removing a hydrogen atom from the methyl group of methyl acetate (top-par_all22_prot_model.str, MAS) and replacement of the side chain of the serine residue (top_all27_prot_lipid.rtf, SER) by the rest of MAS. For an accurate description of the SEA residue, the name of some atoms belonging to MAS with the same name of atoms in the preserved part of the serine residue was modified (C by CE, O by OE). The charge of the C2 carbon atom in MAS was adjusted from -0,14 to -0,05 (this value was obtained by adding the charge (0,09) of the hydrogen atom, which was removed from MAS). The C2 atom was assigned to be a CT2 (CH2) atom type instead of CT3 (CH3). The parameters missing for describing the bond OS-CT2 and the angle bending OS-CT2-CT1 in SEA were assigned in analogy to the parameters for OSL-CTL2-CTL1 and OSL-CTL2 in lipids (par_all27_prot_lipid.prm) (Escorcia, Molina, Daza, & Doerr, 2013).

Solvation cycles Run	Number of toluene molecules added*	k (mol/Å^2)*
1	860	fixed
2	100	50
3	19	45
4	12	40
5	26	35
6	14	30
7	8	25
8	10	20
9	7	15
10	13	10
11	9	5
12	11	3
13	9	1

*MD simulation of ACE03 **force constant of harmonic constraints on all residues within 30 Å around CA (SEA) –active region-, toluene and crystal water molecules are free to move, all other residues are fixed (Escorcia, Molina, Daza, & Doerr, 2013).

Appendix C: Naming scheme of computer models

Michaelis complexes (MCC):

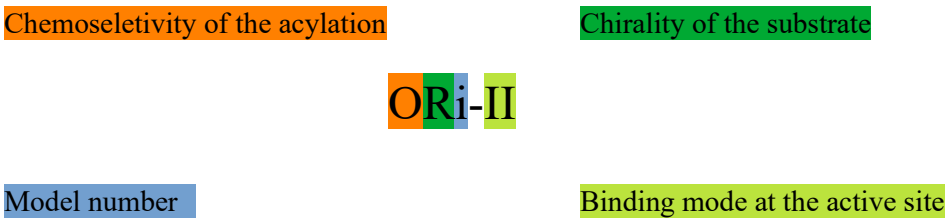

Tetrahedral Intermediate -2 (TI-2)

Appendix D: Time evolution of the possible hydrogen bonds between D187 and H224 in ORi-I and OSi-I Michaelis complexes

Figure 34

Effect of the Iseed number on the potential hydrogen bonds between D186 and H224. The distances are showed at the bottom of the graphic and the angles at the top. The hydrogen bond between H224 and non-carbonylic oxygen in D224 shows lower distances and angles closer to 180° (blue color dots) than hydrogen bond between H224 and cabonylic oxygen in D224 (green color dots). The schematic representation of the more stable hydrogen bond is represented as "distance -a-" (Figure 9) ORi-I and OSi-I complexes are selected as examples.

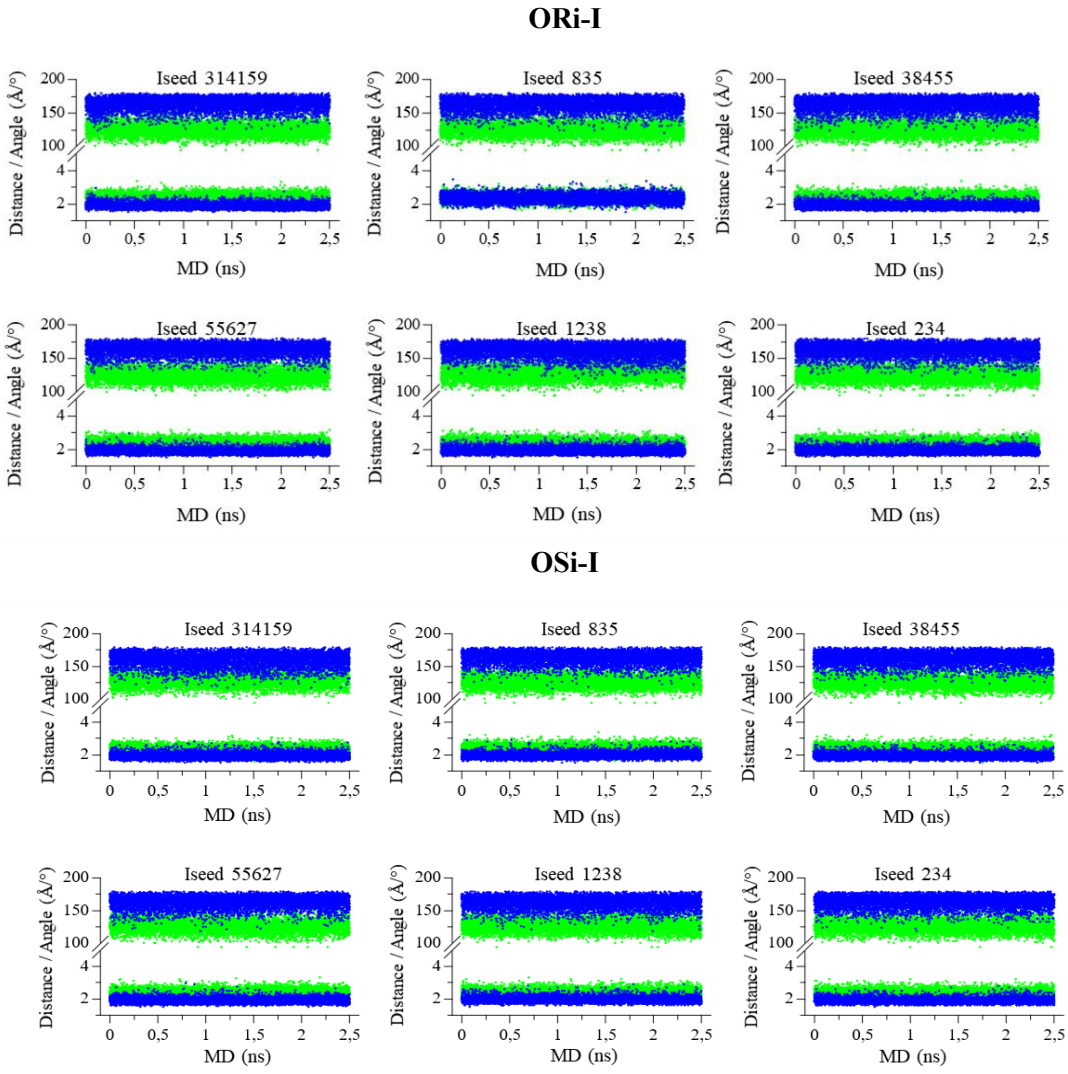

Appendix E: Time evolution of the hydrogen bonds between at the oxyanionic hole in the ORi-I and OSi-I Michaelis complexes

Figure 35

*Effect of the Iseed number on the hydrogen bonds at the oxyanionic hole. The hydrogen bonds -d- (Q106:NH-SEA105), -e- (T40:OH-SEA105), and -f- (T40:NH-SEA105) (**Figure 9**), are represented in black, red, and green colors. ORi-I and OSi-I complexes are selected as examples.*

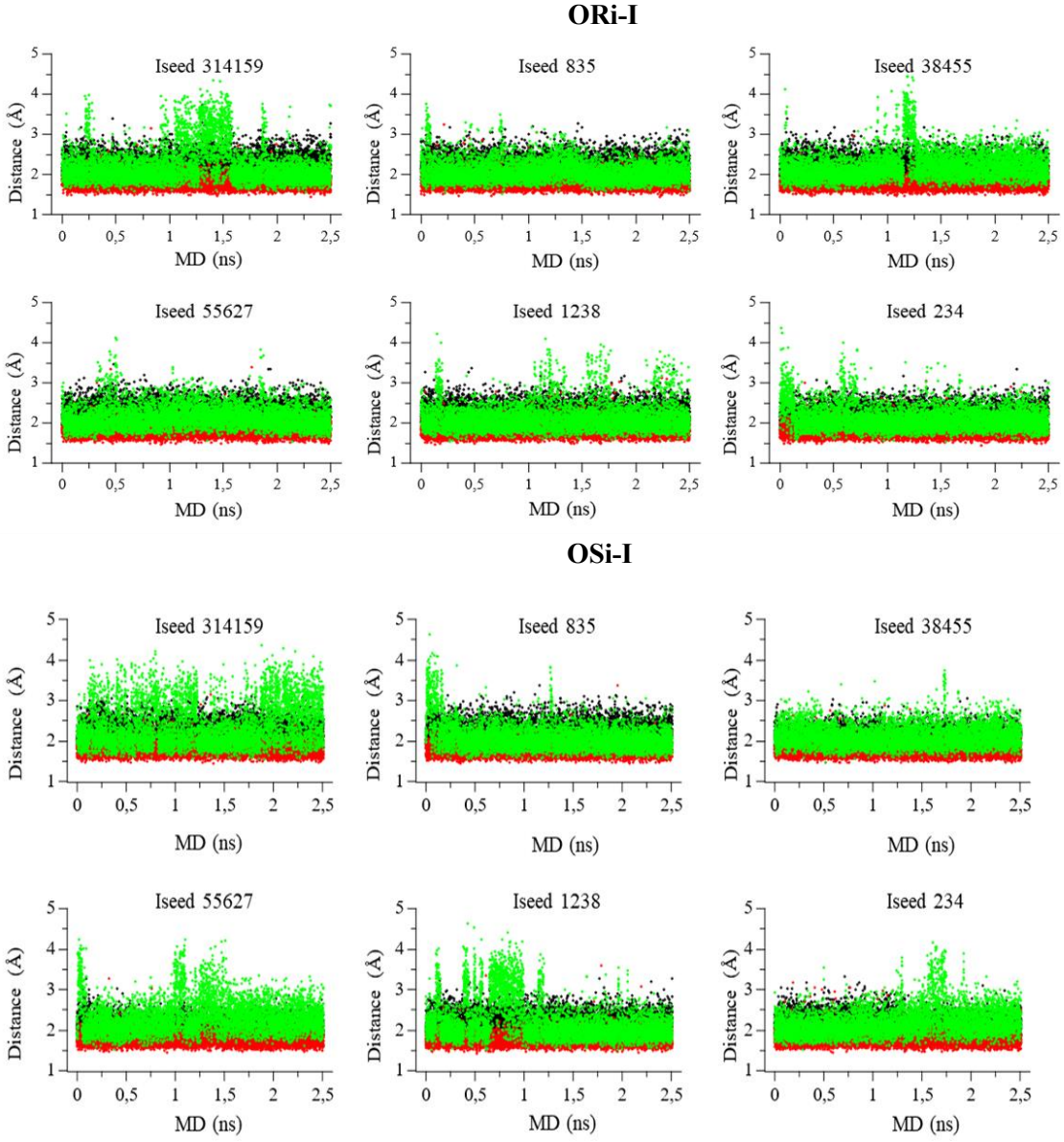

Appendix F: Time evolution of the interatomic distances -b- and -c- in the ORi-I and OSi-I Michaelis complexes

Figure 36

Effect of the Iseed number on the distances -b- (PROP:H-H224:N), black dots and -c- (PROP:O-SEA105:CE), red dots. ORi-I and OSI-I complexes are selected as examples.

ORi-I

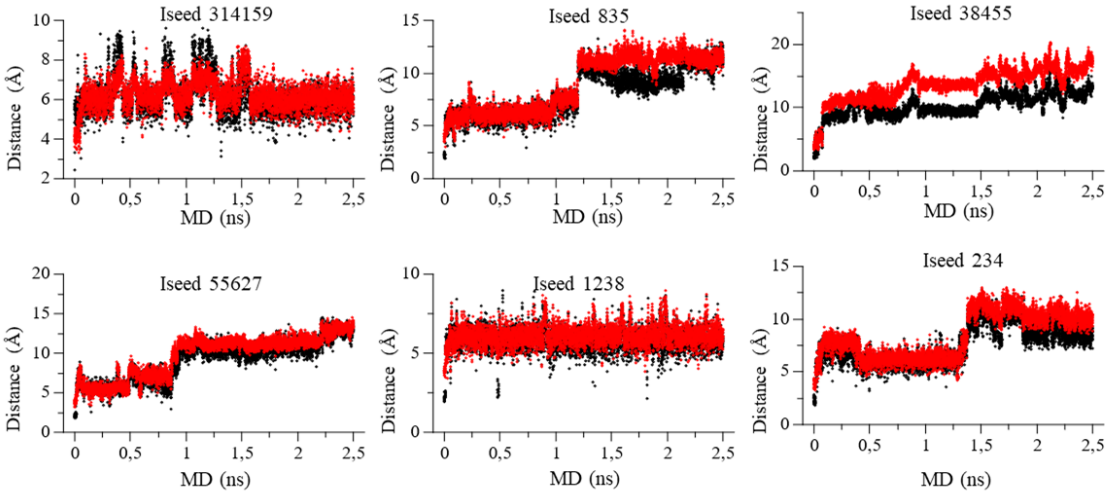

OSi-I

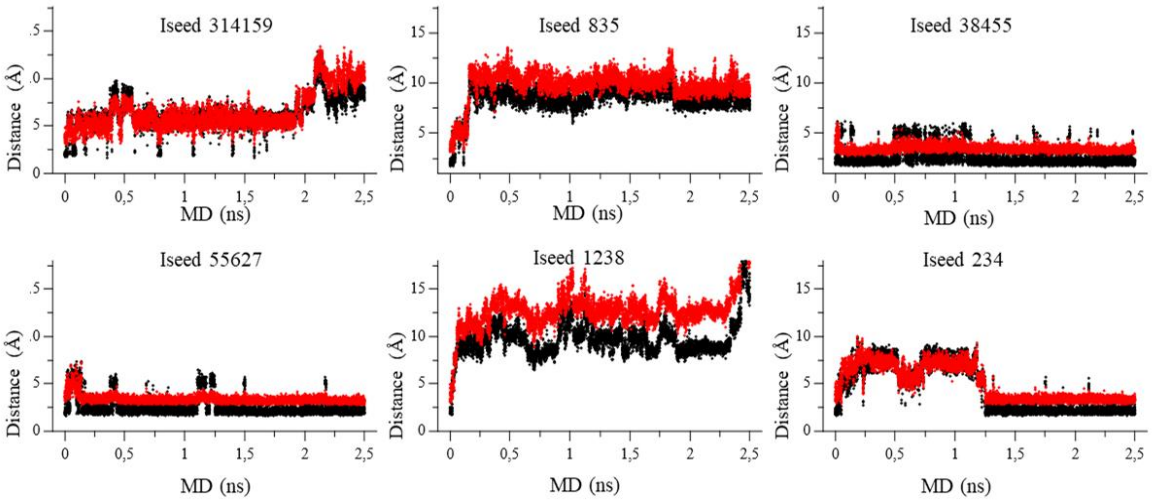

Appendix G: Time evolution of the RMSD of the backbone of AceCalB and the surrounding secondary structures of the active site in the ORi-I and OSi-I Michaelis complexes

Figure 37

RMSD evolution of the all heavy atoms of the backbone of the AceCalB (black diamonds), the surrounding secondary structures of the active site: L136-T156 (red diamonds), A185-V194 (green diamonds) and L178-V286 (blue diamonds). To see localization of these sequences on the tertiary structure, see Figure 12.

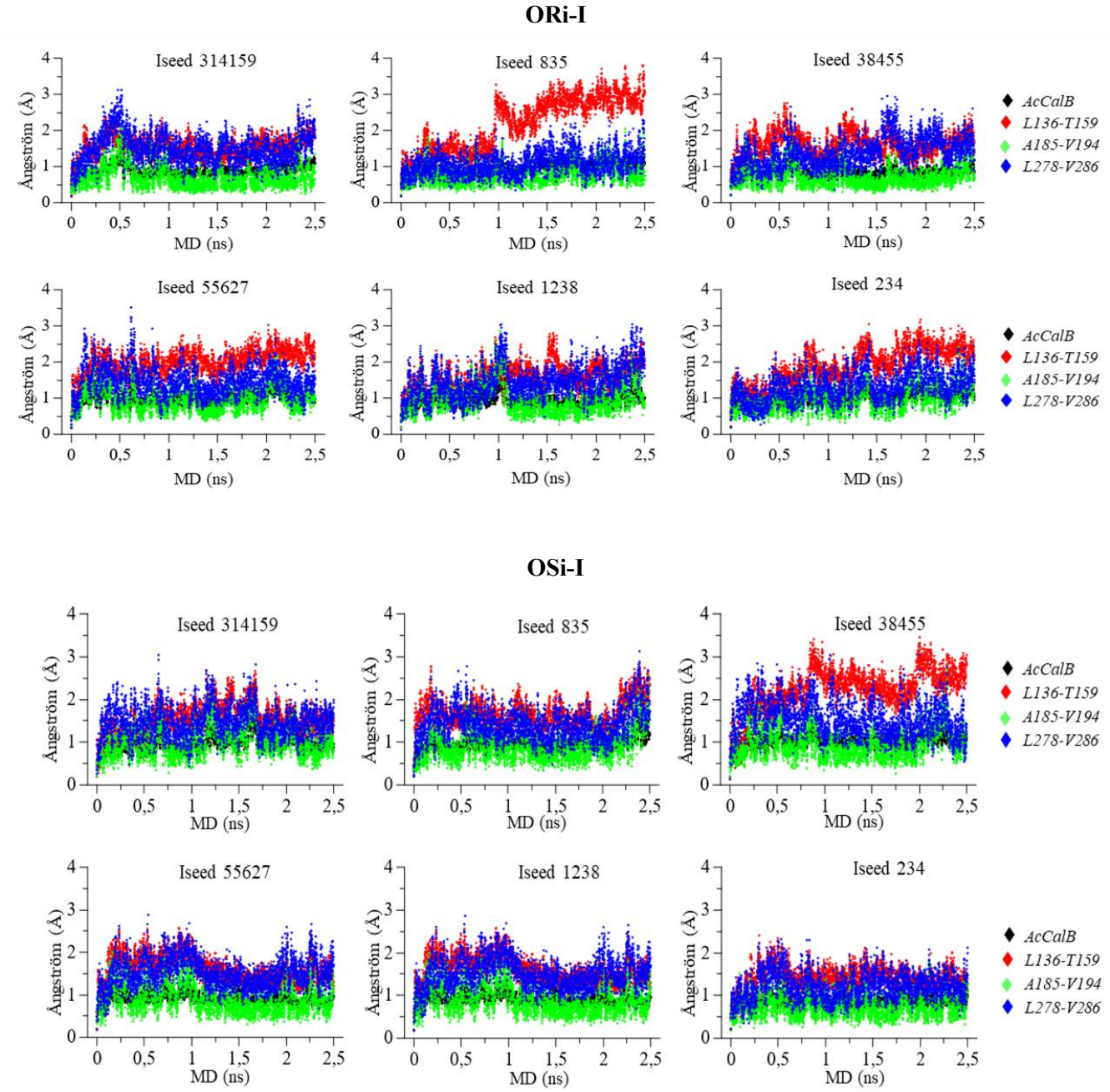

Appendix H: TI-2 conformations selected to QM/MM MD (SCC-DFT/CHARMM) theory level

Figure 38

Tetrahedral Intermediate-2 (TI-2)conformations selected to QM/MM MD (SCC-DFT/CHARMM) theory level. The conformations for (R)- or (S)-propranolol in binding modes I (ORI, OSI) and II (ORII, ORIII, OSII, OSIII), originally these structures were optimized at the QM(B3LYP/TZVP)/ CHARMM level and was used as starting structures for energetic barriers calculations. The substrate, catalytic triad, and oxyanion hole are shown in licorice with the carbon atoms in green. Protein residues surrounding the substrate are shown in licorice and transparent magenta color(Escorcia, 2015).

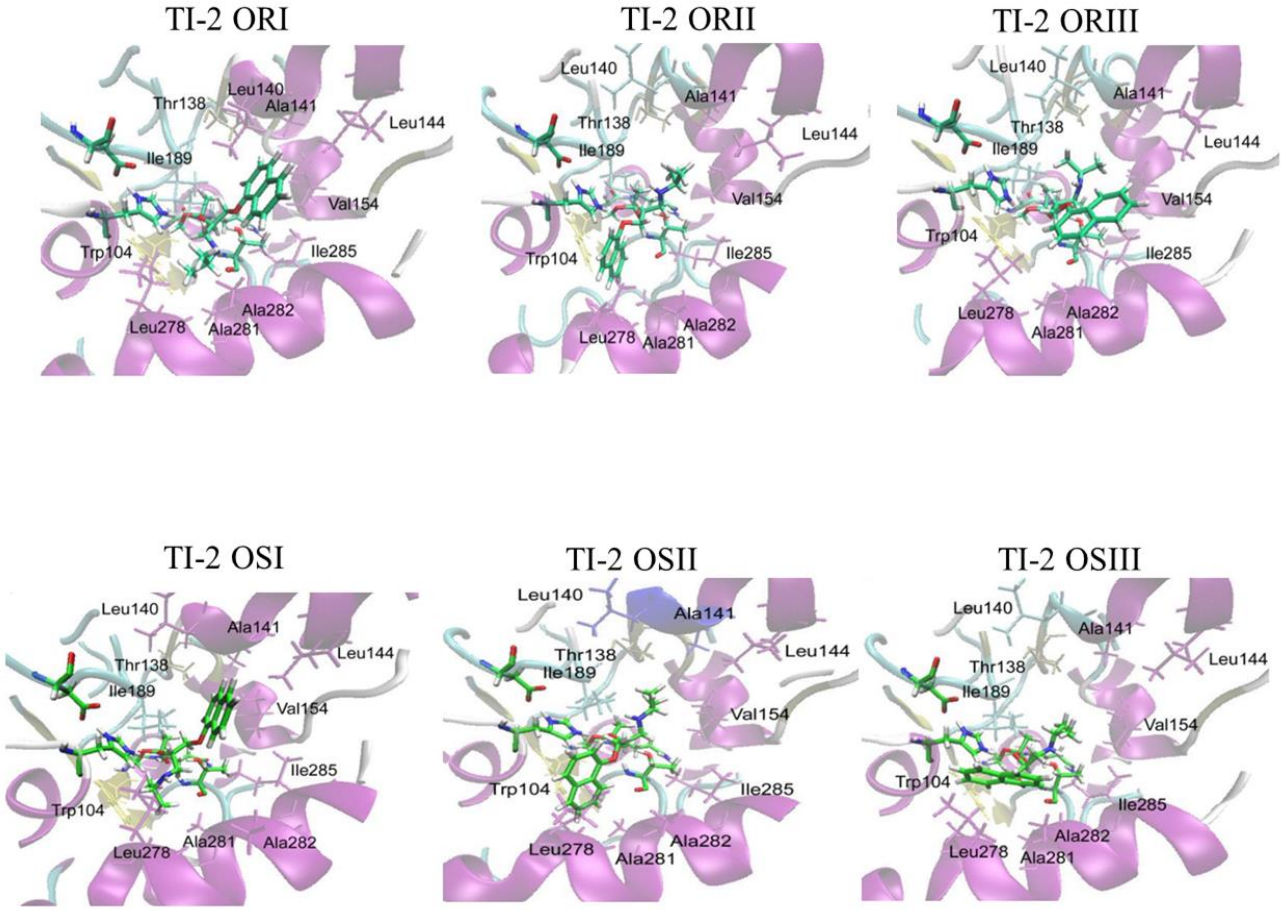

Appendix I: Key interatomic distances in the stability of the TI-2

Figure 39

Key interatomic distances in the tetrahedral intermediate 2 (TI-2). Left: TI-2 in the enantioselective step of the acylation reaction. The dotted lines indicate the key hydrogen bonds in the catalytic mechanism. The blue line indicates the distance between the oxygen of the hydroxyl group of propranolol and the electrodefficient carbon of SEA105. Right: Scheme of the connectivity of residues SEA 105, D187, and H224 as were designed at the topological residue file (.rtf) in CHARMM, the involucrated atoms in these distances are highlighted in green. The distances are: -a- hydrogen bond D187OD"···H224HD1, -b- hydrogen bond H2242HE···SEA105O39, -c- covalent bond SEA105O39—SEA105CE, -d- hydrogen bond SEA105OE···Q106NH, -e- hydrogen bond SEA105OE···T40NH, -f- hydrogen bond SEA105OE···T40OH, -g- covalent bond SEA105CE—SEA105OM and -h- potential hydrogen bond SEA105OM ···H2242HE.

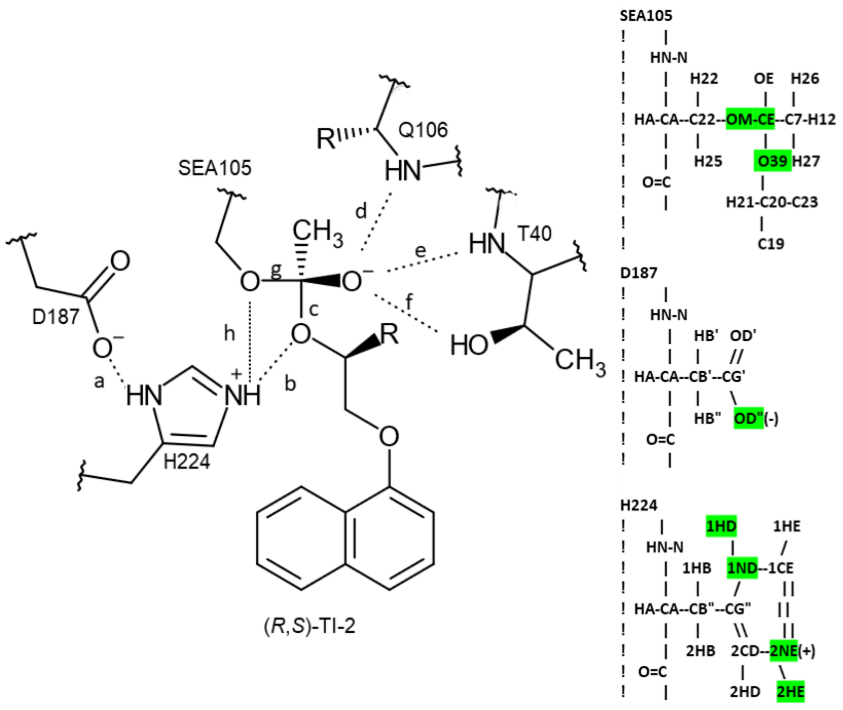

Appendix J: Time evolution of the key interatomic distances in the stability of the TI-2

Figure 40

*Time evolution of the key interatomic distances in the stability of the tetrahedral intermediate 2 (TI-2). **A**. Hydrogen bond D187···H224, **B**. Hydrogen bond H224···O39(propranolol), **C**. Hydrogen bonds carbonylic oxygen in SEA105 and aminoacidic residues at oxyanionic hole: SEA105OM ···Q106 and SEA105OM···T40 in black, red, and green diamonds. **D**. The covalent bonds of the TI-2 and the potential hydrogen bond between H224 and SEA105O (distances -d-, -g- and -h-) in black, red, and green diamonds. The scheme of these distances can be found in Figure 9.*

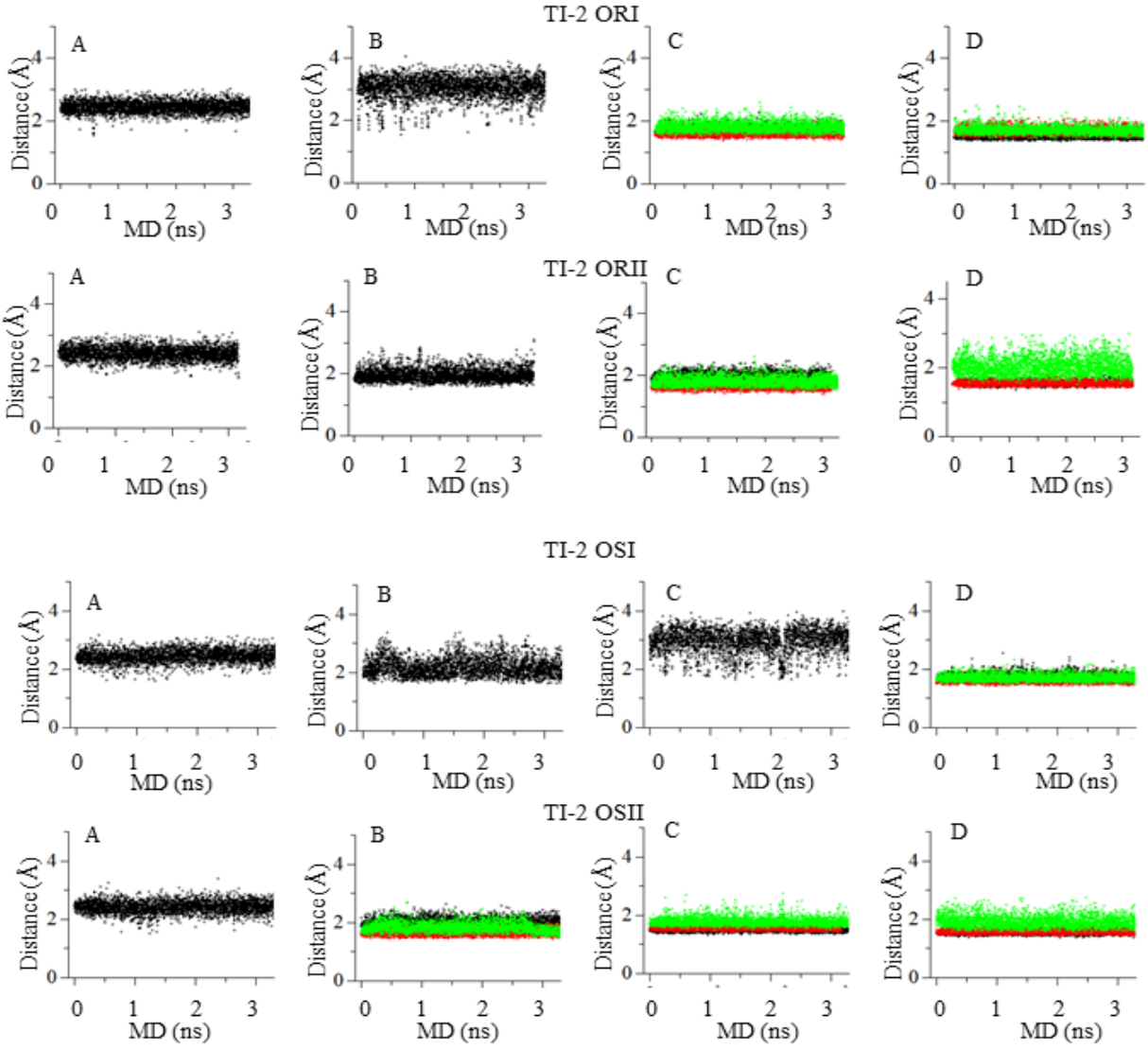

Appendix K: Harmonic restraining constant (k_u) effect in the PMF for ORIII-a conformation

Figure 41

*Harmonic restraining constant (k_u) effect in the PMF for ORIII-a conformation. On the left PMF from the WHAM output file. On the right, the polynomial fit. The sampling was performed in reaction coordinate ξ1. The arrow indicates the sampling direction. The k_u used were 30, 40, and 50 (kcal/mol*Å^2) and are represented in black, red, green, and blue colors, respectively. The histograms from time sampling of 60ps used for WHAM calculations are shown the Figure 5S in the supporting information.*

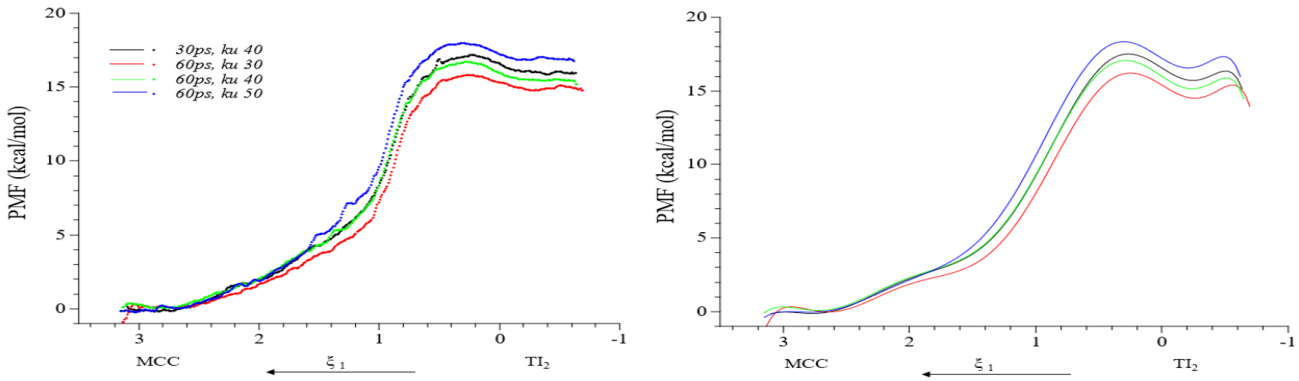

Appendix L: QM (SCC-DFTB)/MM highly endergonic potential mean force (PMF) for the conversion of (*R,S*)-propranolol to *O*-acetylpropranolol in binding modes I and II

Figure 42

*QM(SCC-DFTB)/MM highly endergonic potential mean force (PMF) for the conversion of (R,S)-propranolol to O-acetylpropranolol in binding modes I and II: OSI-a and ORIII-a respectively. # Relative to Michaelis complex values. * Reaction coordinate after merge RCs ξ1 and ξ2, see methodology section. The symbols were graphed by skipping six points in all curves. Table at the left shows the relative PMF value at free energy barrier 1 (B1), Tetrahedral intermediate (TI-2), free energy barrier 2 (B2), and enzyme-product complex (EPC).*

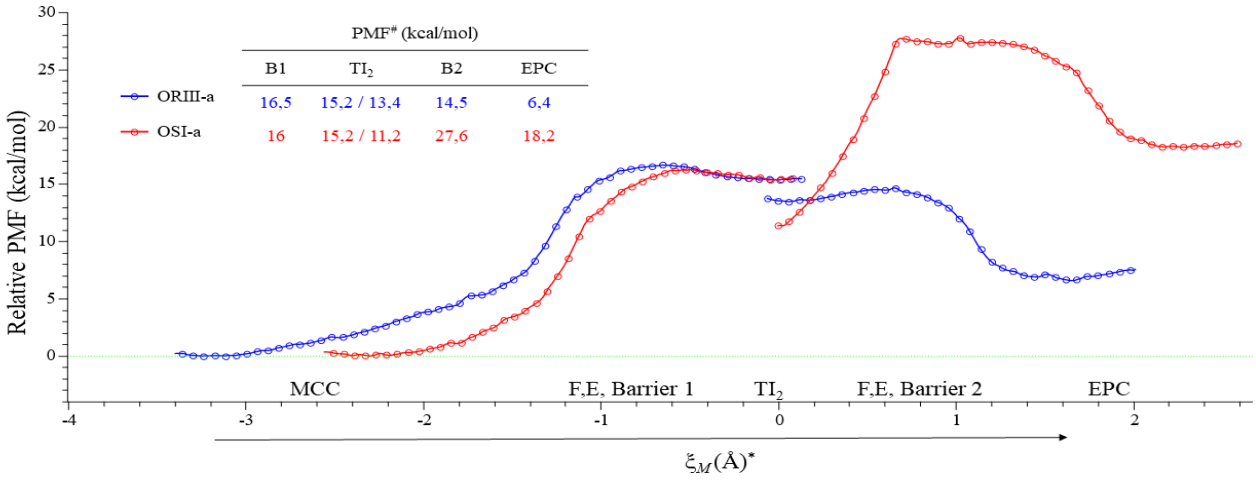

Appendix M: Evolution of the hydrogen bonds between carbonylic oxygen of SEA105 and oxyanionic hole for the *O*-acylation of (*R,S*)-propranolol catalyzed by CalB in conformations ORIII-a and OSI-a

Figure 43

*Evolution of the hydrogen bonds between carbonylic oxygen of SEA105 and oxyanionic hole for the O-acylation of (*R,S*)-propranolol catalyzed by CalB. The hydrogen bonds Q106NH···SEA105OE, T40NH···SEA105OE, and T40OH···SEA105OE (distances -d-, -e-, and -f- Figure 9) are represented as lines black, red, and green. The evolution is shown in the reaction coordinate that explores the TI-2 formation from MCC (ξ1) or EPC formation from TI-2 (ξ2); see the methodology section. Arrows indicate the sampling sense. The conformations ORIII-a and OSI-a had highly endergonic pathways.*

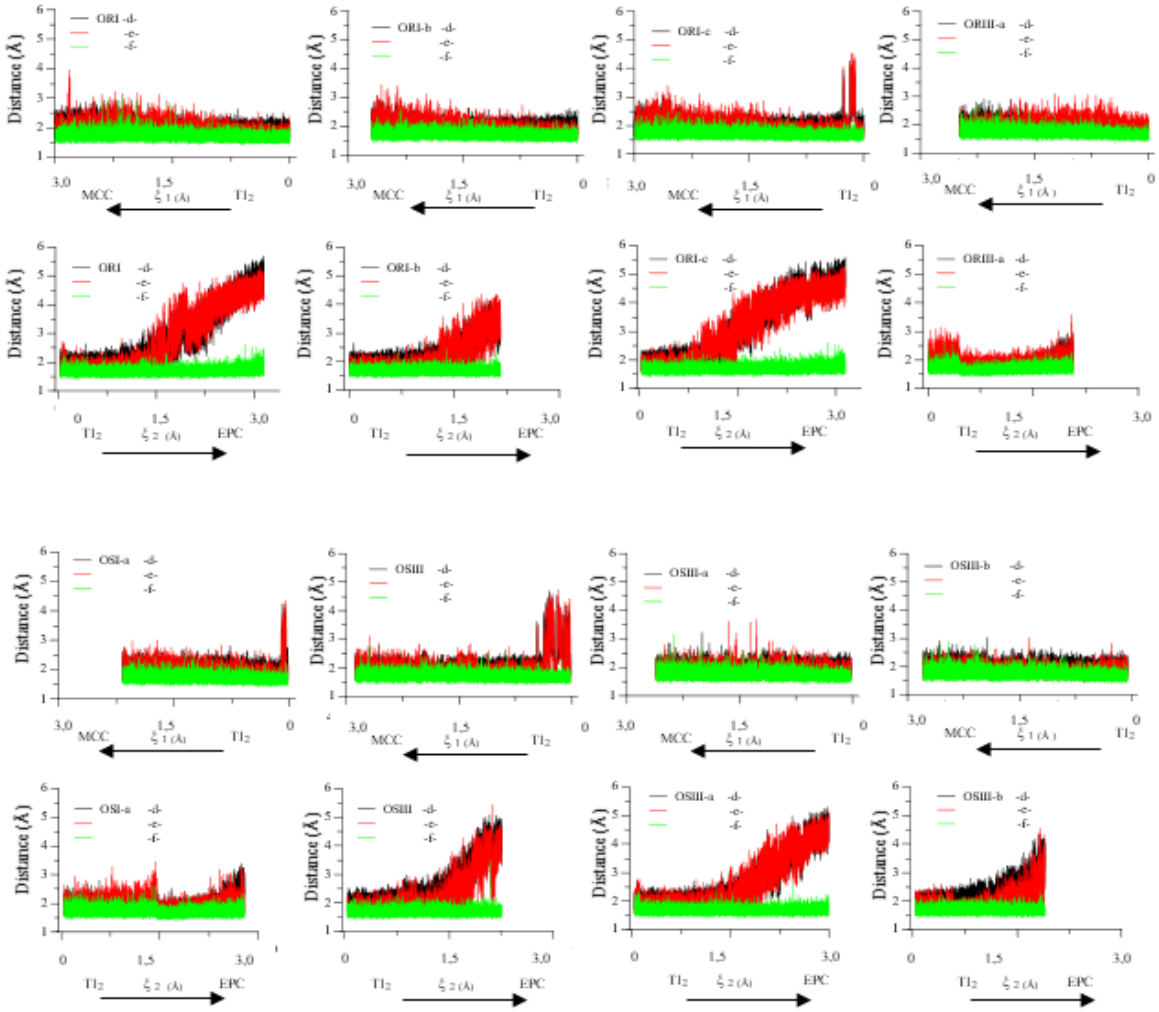

Appendix N. Reaction coordinate behavior for the *O*-acylation of the (*R,S*)-propranolol in Binding mode I and II

Figure 44

Reaction coordinate behavior for the O*-acylation of the (*R,S*)-propranolol in Binding mode I and II. Left: TI-2 formation from MCC is monitored by ξ_1, green dots, and it is composed of the difference between the distance of covalent bond $Prop_{O39}$-$SEA105_{CE}$ and the hydrogen bond $His224N_{\varepsilon}H\cdots Prop_{O39}$, red and black dots. Right: EPC formation from TI-2 is monitored by ξ_2, green dotes, and it is the difference between the distance of the covalent bond $SEA105_{CE}$-$SEA105_{OM}$, and the hydrogen bond $His224N_{\varepsilon}H\cdots SEA105_{OM}$ magenta and blue dots. r -a- ($His224N_{\varepsilon}H\cdots Prop_{O39}$), r -b- ($Prop_{O39}$-$SEA105_{CE}$), r -c- ($SEA105_{CE}$-$SEA105_{OM}$), and r -d- ($His224N_{\varepsilon}H\cdots SEA105_{OM}$), (**Figure 9**).*

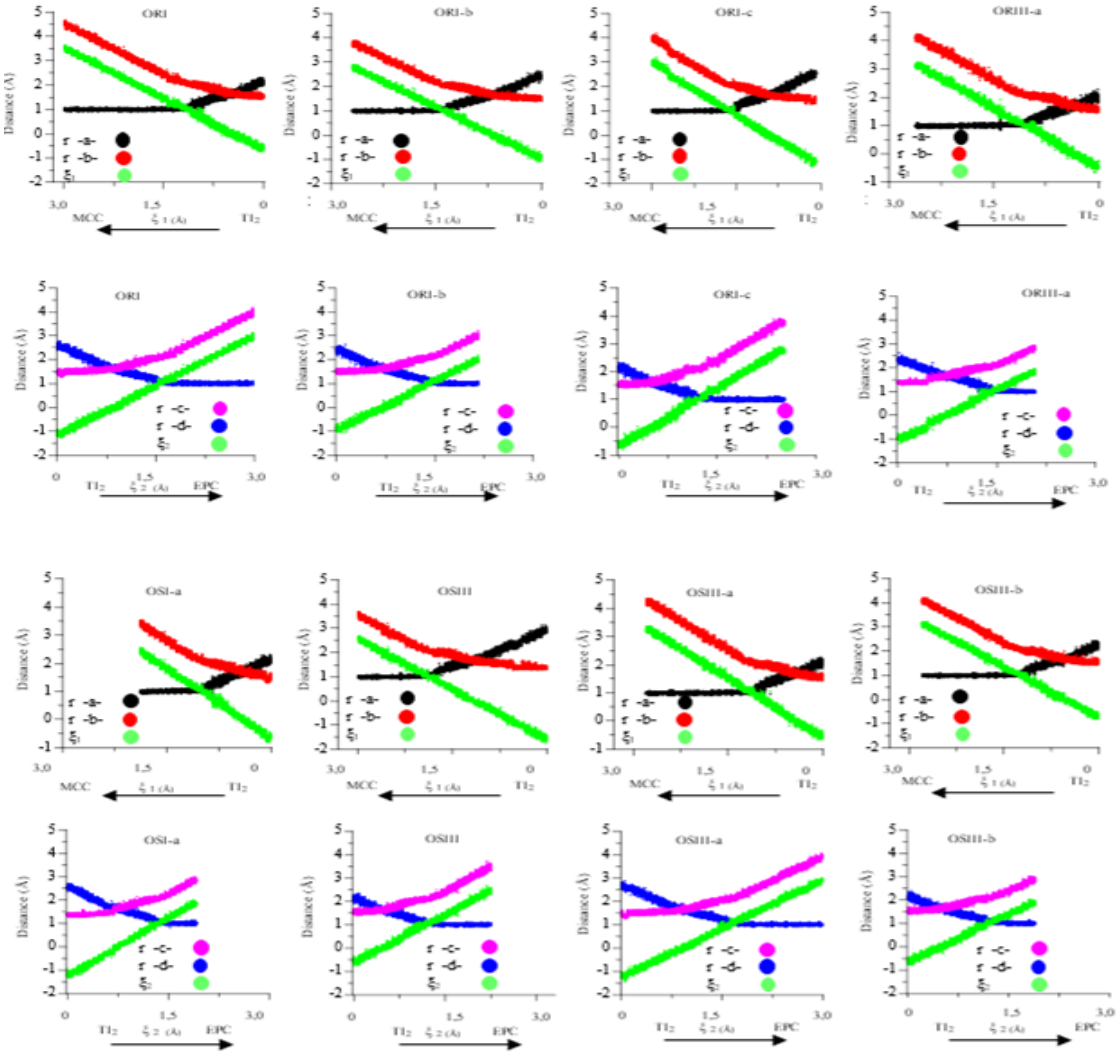

Appendix O. QM(SCC-DFTB)/MM potential energy explorations for the conversion of (*R,S*)-propranolol to *O*-acetylpropranolol in binding modes I and II

Figure 45

*QM(SCC-DFTB)/MM potential energy explorations for the conversion of (R,S)-propranolol to O-acetylpropranolol in binding modes I and II. ORI, ORI-b, and ORI-c are different conformations in Binding mode I and OSIII, OSIII-a, and OSIII-b are different conformations in Binding mode II. All energy values are relative to the Michaelis complex. The initial structures correspond to the snapshots selected from structural cluster analysis. *Reaction coordinate after merge RCs ξ_1 and ξ_2, see methodology section. Michaelis Complex (MCC), Tetrahedral intermediate (TI-2), and enzyme-product complex (EPC).*

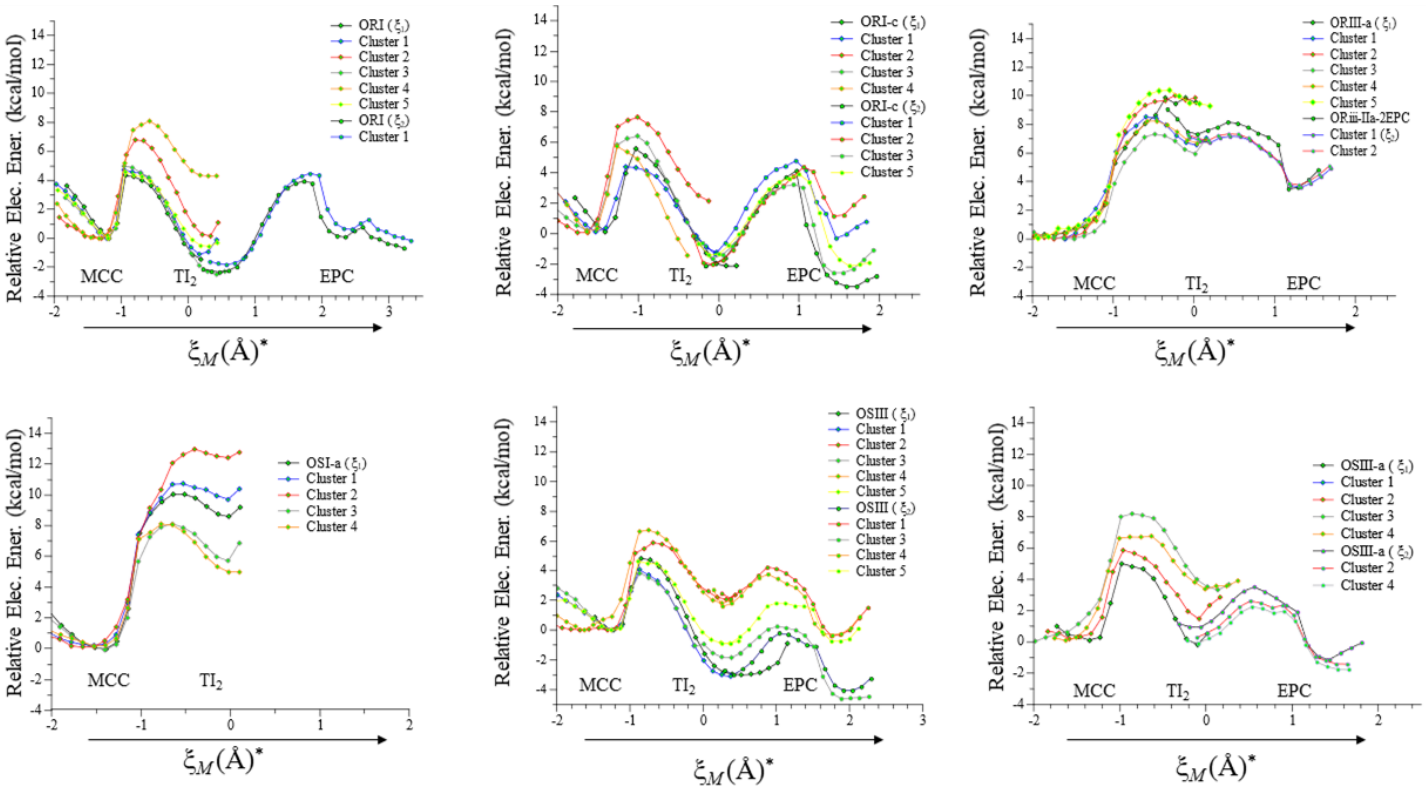

Appendix P. Finite-temperature effects for the conversion of (*S*)-propranolol to *O*-acetylpropranolol in binding modes I and II

Figure 46

Finite-temperature effects for the conversion of (S)-propranolol to O-acetylpropranolol in binding modes I and II. For comparison, the QM(B3LYP/TZVP)/CHARMM results calculations are showed at the top on the right. PMF is the magenta line. PES values are the lines red, black, and blue. Doted lines connect the electronic energy values previously reported.